Development of Persistent Quantum Memories

Manjin Zhong

A thesis submitted for the degree of
Doctor of Philosophy (Physics)
The Australian National University

June, 2017

Declaration

This thesis is an account of research undertaken between November 2009 and June 2017 at the Laser Physics Centre, Research School of Physics and Engineering, The Australian National University, Canberra, Australia.

Except where acknowledged in the customary manner, the material presented in this thesis is, to the best of my knowledge, original and has not been submitted in whole or part for a degree in any university.

Manjin Zhong
June, 2017

Acknowledgements

First and foremost, I would like to thank my primary supervisor, Matt Sellars, for his academic guidance and support throughout my PhD project. His enthusiasm, optimism and patience has inspired me to regain confidence in the most difficult period, either with my project or life. Though it has been a challenging experience, I was able to went through with much fun and reward due to his rich knowledge, creativity as well as his sense of humour. Being his student was one of the luckiest things in my life. I would also like to thank my other supervisor, Neil Manson, for fostering such a great work environment, and for being a dependable source of advice and support.

I would like to thank Morgan Hedges, John Bartholomew and Rose Ahlefeldt for their experimental guidance and support especially at the earlier stage of my time in the lab. In particular, I would like to acknowledge John Bartholomew and Rose Ahlefeldt for their consistent support on my data analysis and writing.

I would like to thank the technical staff of the Laser Physics Centre, Craig Macleod and John Bottega. For Craig, I would like to thank him for building my sample rod mount, which was essential for my project but was tricky to build due to its small dimension and high angular precision requirement. And John, I would like to thank him for supplying me with liquid helium constantly especially for his work on liquid helium during those off-work hours. Being a small lady, I am particularly grateful for John's considerate help to move the huge liquid helium dewar through the step for every single fill.

I would like to thank the staff in RSPE School Computer Unit, for their help with my problems on computers and the internet issues. I would also like to thank the staff of the ANU Security, for picking my up in the school and taking me home in the Ursula Hall for the many times whenever I worked late in the lab into the midnight.

I would like to thank all the wonderfull people I've worked with in the Solid State Spectroscopy Group: Rose, Sarah, Sven, Morgan, John, Sara, Kate, Milös and Michael. In particular, Sarah and Morgan for introducing me about the many culture and customers about Australia when I first arrived, Rose for her courtesy of sharing with me her apartment as well as her assistance on my baking and swimming skills, Sven for designing my sample rod, Sara for sharing the many wonderful after-hour times and Milös for teaching me to drive a manual car. Thanks also to Rose, Kate and Milös for proof reading my thesis. I would like to thank all of you for being patient with my not that fluent speaking English and for forgiving me whenever I used wrong words.

Finally, I would like to thank all my friends and family, for your continued support and encouragement throughout my studies. I would like particularly thank you, Yinan, my sweet boy, let me realise that after the storm, there would come the beautiful rainbow.

Abstract

This thesis investigates the coherence properties of the hyperfine transitions of the $^{151}Eu^{3+}$ ions in Eu^{3+}:Y_2SiO_5 and evaluates the potential of developing quantum memories using these transitions.

Quantum memories for light with long storage times are required for quantum communication applications. For these memories to be useful they need to have storage times long compared to the transmission times across the communication network. For a global optical communication network this requires storage time longer than 100 ms. Rare-earth doped crystals have been identified as a suitable storage material. The storage time of these systems is limited by the coherence time of the hyperfine transitions of the optically active rare-earth ions. In previous work it had been demonstrated that coherence times as long as 1.4 seconds could be achieved for hyperfine transitions in Pr^{3+}:Y_2SiO_5 by applying a particular magnetic field such that the first order Zeeman shift of the transition nulled. This technique is known as zero first-order Zeeman (ZEFOZ). Due to the relatively large second order Zeeman efficient of the transitions in Pr^{3+}:Y_2SiO_5, an extension of the coherence time, significantly beyond the 1.4 second mark using ZEFOZ, is not expected. However, it has been predicted that coherence times more than two orders of magnitude longer could be achieved in Eu^{3+}:Y_2SiO_5 due to the smaller second order Zeeman shifts associated with the relevant hyperfine transitions.

The dominant decoherence mechanism for the hyperfine transitions in diluted Eu^{3+}:Y_2SiO_5 is the magnetic field perturbations caused by the random spin reconfiguration of the Y^{3+} ions in the host. By applying the ZEFOZ technique, previously used in Pr^{3+}:Y_2SiO_5, the sensitivity of the transition's frequency to environmental magnetic field perturbations was significantly reduced. Further, this strong ZEFOZ magnetic field was also shown to induce a frozen core around the Eu^{3+} ion, which resulted in a significant suppression of the reconfiguration of the nearby Y^{3+} spins. The combined effect of the reduced sensitivity and frozen core effect allowed a decoherence rate of 8×10^{-5} s^{-1} over 100 milliseconds to be demonstrated. The observed decoherence rate is at least an order of magnitude lower than that of any other system suitable for an optical quantum memory. Furthermore, by employing dynamic decoherence control, a coherence time of 370 ± 60 minutes was achieved. This 6 hour coherence time observed here opens up the possibility of distributing quantum entanglement via the physical transport of memories as an alternative to optical communications.

It was found that even at the critical point alignment the observed coherence times showed that the Y^{3+} spin flips remain the dominant decoherence mechanism. To aid in the development of future strategies to further extend the coherence time beyond 6 hours, a study of the Y^{3+} spin dynamics in the frozen core was conducted. Four of the Y^{3+} sites were resolved and a complete mapping of all frozen-core Y^{3+} sites was limited by the inhomogeneity of the applied magnetic field. The Rabi frequency, the coherence time and lifetime as well as the interaction strength with the Eu^{3+} ion of one of these Y^{3+} ions were measured. The observed lifetime of the Y^{3+} ion is 27 s, which is four orders of magnitude longer than the low field value. With the technique developed, a detailed understanding

of the frozen-core dynamics is possible, which would allow an extension of the hyperfine coherence time of the Eu^{3+} ion towards the lifetime limit.

In summary, this thesis provides a detailed characterisation of the decoherence mechanisms of the hyperfine transitions in Eu^{3+}:Y_2SiO_5. The potential of using rare-earth doped crystals for the long-term storage of quantum information with applications to long-range quantum communications is identified. The demonstrated long coherence time of the quantum transitions for information storage allows a new way of entanglement distribution: entanglement is transported by physically transporting the memory crystal rather than the light. This approach opens a new regime for both quantum communication and fundamental tests of quantum mechanics.

Contents

Chapter 1

Background and Motivation

The establishment of quantum entanglement over a space-like distance is a critical operation for fundamental tests of quantum mechanics and for quantum communication applications. Seminal papers in the field envisaged entanglement distribution as the process of locally entangling two material systems, such as spin-1/2 particles, and then separating them [1–4]. Although conceptually appealing, this proved impractical because of the losses due to the rapid decoherence rates of otherwise suitable quantum systems. Thus, researchers nowadays have turned to using photons to distribute entanglement because it is easier to generate and transmit photon pairs than spin-1/2 particles. However, losses associated with scattering, diffraction and absorption of the light still limit the effective range of this direct distribution to a few hundred kilometres [5, 6].

A proposal to overcome this range limitation and build a worldwide quantum network is the quantum repeater protocol [7, 8], which involves the distribution of entangled pairs of optical modes between many quantum memories stationed along the transmission channel. To be effective, the memories must store the quantum information encoded on the optical modes for times that are long compared to the direct optical transmission time of the channel.

There is significant interest in developing suitable memories based on mapping optical quantum states onto the hyperfine states of rare-earth optical centres in crystals [9–15]. Rare-earth doped crystals possess properties that make them well suited for ensemble-based quantum memories for light. They have optical transitions with homogeneous line widths close to the lifetime limit [16], high optical depths [11], long-lived hyperfine states accessible via optical excitation [17] and no spatial diffusion [12]. The latter is an important distinction from atomic-based ensembles.

There have been major advances in developing rare-earth ion based quantum memories including the demonstrations of the spin-wave storage of the quantum entanglement [18], multimode storage of coherence quantum states [19], memories operating with large efficiencies [11, 20], and storage for single photons and quantum entanglement [13, 14]. Among the many rare-earth-ion-based energy levels studied for quantum memory applications, nuclear spin states of europium-ion dopants in yttrium orthosilicate (Eu^{3+}:Y_2SiO_5) are particularly attractive due to their extremely long observed lifetime of 23 days [17] and their optical accessibility. The focus of this thesis is the characterisation of the decoherence mechanisms affecting the ground $^7F_0$ state hyperfine transitions of low concentration $^{151}Eu^{3+}$ ions in Eu^{3+}:Y_2SiO_5 in order to extend the coherence times.

The approach used to extend the coherence time is known as the zero first-order Zeeman (ZEFOZ) technique, which works by applying a particular magnetic field at which the transition of interest undergoes a critical point. At the critical point, the sensitivity

of the transition is not sensitivity to field fluctuation to first order leading to an extension of the coherence times. The ZEFOZ technique was first implemented in Pr^{3+}:Y_2SiO_5 and resulted in an extension of the hyperfine coherence time of Pr^{3+} from 500 µs to 1.4 s [21]. A further increased coherence time of greater than 40 s was demonstrated due to the combination of the ZEFOZ technique and dynamic decoherence control (DDC) [10, 12]. DDC is a strategy of fighting decoherence by applying a sequence of controlling pulses to alter the dynamic of the system and refocus the system-environment evolution (Section 3.1.4). Given this coherence time is approaching the limit imposed by the lifetime of the spin stats as well as the transition's second order magnetic field sensitivity, a significant increase in coherence time is unlikely in Pr^{3+}:Y_2SiO_5 [10, 12]. It was predicted by Longdell et al. that hour-long coherence time should be achievable in Eu^{3+}:Y_2SiO_5 using the ZEFOZ technique and DDC [22]. This is because the hyperfine transitions in Eu^{3+}:Y_2SiO_5 have much smaller second order magnetic field sensitivity.

The expected hour-long coherence time would satisfy the storage time requirement of the quantum repeater protocol for building a worldwide quantum network. In addition, it would also allow revisiting some very early approaches to entanglement distribution through local entanglement and transport of quantum memories [3, 23].

1.1 EPR paradox and entanglement

Entanglement is one of the most counterintuitive physical phenomena of the quantum world. It occurs when multiple particles are linked together in such a way that the measurement on the quantum state of one particle determines the quantum states of the other particles. A entangled multi-particles system is described by an overall wavefunction that cannot be factored to be the product of the individual functions for each particle. Thus, a measurement of any observables such as position, momentum, spin, or polarisation on either one particle or the whole system would simultaneously collapse this wavefunction such that each particle is in an eigenstate of the measurement operator.

The concept of entanglement originates from a paper published by Albert Einstein, Boris Podolsky and Nathan Rosen (EPR) in 1935 [1]. The EPR paper concluded that the accepted formulation of quantum mechanics (Niels Bohr's Copenhagen interpretation) is incomplete, with missing "hidden variables" [2]. This is known as the EPR paradox, and triggered heated debate in the physics community at the time [2–4, 24].

The EPR paradox can be described using Figure 1.1(a). We have a source that emits electron-positron pairs and we have two separated observers Alice and Bob. The electron is sent to Alice and the positron is sent to Bob. Each pair from the source occupies a spin singlet state so the electron and the positron are entangled. Alice and Bob each chooses a coordination axis to measure the spin state of their received particles. For example, Alice might choose the z axis and find the electron is in the spin up ($+z$) state. Then, if Bob also chooses the z axis, he would find a spin down ($-z$) state for his positron. Conversely, if Alice gets $-z$, Bob will measure $+z$. The same result will hold true whenever Alice and Bob choose the same measurement axis: they will always record opposite results. According to the Copenhagen interpretation of quantum mechanics, there is no way to know the state of the electron-positron pairs before a measurement, but if you measure one of them, you will know the state of the other simultaneously because they have a shared wavefunction.

The correlation between their measurements can be described more generally when Alice and Bob do not use the same coordination frame. As shown in Figure 1.1(b), Alice

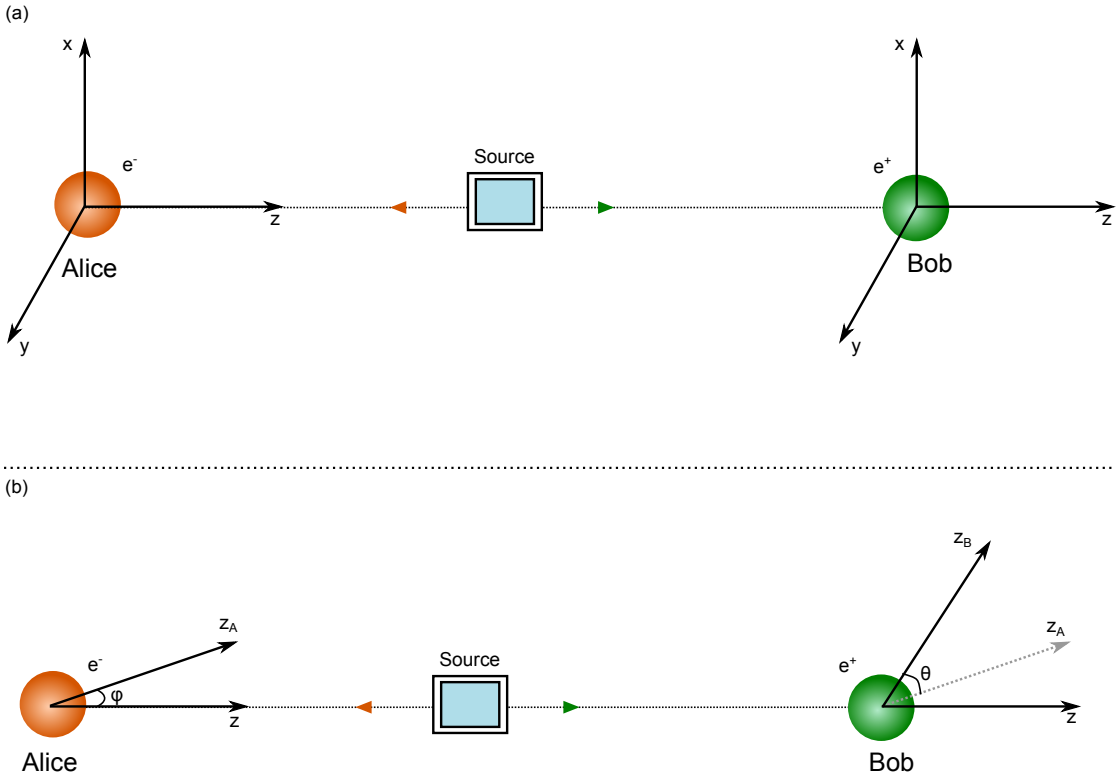

Figure 1.1: A setup that illustrates the EPR paradox. A spin singlet source emits entangled pairs of electron and positron going in opposite directions to observers Alice and Bob. (a), Alice and Bob perform their measurements using the same coordination frame. (b), Alice and Bob use different frames.

measures her electron along an axis z_A, which is defined by an angle φ from the z axis. Bob measures his positron along an axis z_B, which is defined by an angle θ from z_A. Alice and Bob have four possible combination for their results, that is $(+z_A, +z_B)$, $(+z_A, -z_B)$, $(-z_A, +z_B)$ and $(-z_A, -z_B)$. The correlation is that no matter what value of φ is chosen by Alice, among the many measurements for a fixed φ and θ, the percentage of their results being $(+z_A, -z_B)$ or $(-z_A, +z_B)$ is always $cos^2\theta$.

There are two explanations for the correlation. One is that the two particles instantaneously communicate with each other and they somehow 'feel' which axis is chosen to be measured on their counterpart (entanglement argument). The other explanation is that there is information, like DNA, embed within each particle at the moment it was created that governs every outcome of a measurement performed on the system ('hidden variable' argument). In the EPR paper, Einstein and his coworkers support the 'hidden variable' theory because they thought that the first explanation violates the theory of relativity, which claims that information cannot be transmitted faster than light.

The term 'entangled' did not appear until 1936, when Erwin Schrödinger published his cat paradox paper [24] in which he described the quantum state of two interacting systems in the following way:

> *When two systems, of which we know the states by their respective representatives, enter into temporary physical interaction due to known forces between them, and when after a time of mutual influence the systems separate again, then they can no longer be described in the same way as before, viz. by endowing each of them with a representative of its own. I would not call that one but rather the characteristic trait of quantum mechanics, the one that enforces its entire departure from classical lines of thought. By the interaction, the two representatives have become entangled.*

Though he used the word 'entangled', Schrödinger was a supporter of the 'hidden variable' theory like Einstein.

The EPR paradox was not resolved until 1964, when John Bell formulated the 'hidden variable' theory mathematically and showed that it violates the statistical predictions of quantum mechanics [4]. Since Bell's original paper, many experiments have been performed [25, 26][27, 28] and their results overwhelmingly supported the Copenhagen interpretation of quantum mechanics. However, until recently, all these experiments rely on additional assumptions and resulted in so-called "loopholes". One significant loophole, known as the locality loophole, is that the correlated events were not separated with a space-like distance when the measurement was carried out, thus the experimental outcomes could have been influenced by subliminal communication [29, 30]. This loophole was eliminated by Hensen and co-workers in 2015 when they reported a loophole-free Bell test [31]. Without any additional assumptions, they were able to observe robust entanglement correlation between spins that had a space-like separation.

An interesting aspect involving the present work is to test Bell's theorem more thoroughly. The Eu^{3+} hyperfine transitions in Eu^{3+}:Y_2SiO_5 have a lifetime of 23 days, implying a limitation of the possible coherence time of 46 days. An exploration of the coherence time towards this limit might allow us to revisit the idea of locally entangling two material systems and separating them. For example, we set up the entanglement between two crystals, and observe their correlation after putting one of them on a satellite orbiting the Earth, and leaving the other one on the ground.

1.2 Quantum communication

Besides the intriguing applications in the study of fundamental physics theories, quantum entanglement has become the foundation of modern quantum information science. One of the ultimate technological goals of modern quantum information science is building a quantum computer in which entangled quantum states are used to perform computations in parallel. This should allow computation for particular tasks to be performed dramatically faster than conventional computers [32]. As a result, certain problems, such as factorisation of large integers, that are intractable with conventional computers become solvable. In the past decade, there has been tremendous progress in the experimental development of a quantum computer, such as the realisation of fourteen quantum bits or 'qubits' [33]. However, a large-scale quantum computer is still an extremely ambitious goal, appearing to us now as classical computers must have seemed a century ago.

An intermediate realisation is quantum communication in which entangled particles are used to transmit signals that cannot be eavesdropped upon without leaving a trace. Before introducing more details on quantum communication, I first discuss the security risks inherent in the current communication system. In order to avoid eavesdropping, a message containing secret or confidential information is encoded before transferring it between two parties. The technique involving the encoding of the information is known as cryptography. Information cryptography is widely employed by governments, military organisations, and by almost every ordinary individual of the modern society. For example, financial organisations use cryptography in their computer security systems to prevent fraud in electronic transactions. One of the most commonly used encryption systems is public key encryption whose security is based on the mathematical difficulty of solving certain problems using current computers. The security of such an encryption scheme relies on two assumptions, that the eavesdropper does not have a sufficiently efficient algorithm for solving the problem and that they have a limited computing power. Not only is there no mathematical proof that such an algorithm does not exist, there is evidence that a functional quantum computer will put public key encryption under challenge [34, 35].

This inevitably leads us to look for alternative ways to encrypt information with a higher degree of security. In quantum communication, information is encoded in quantum states, or qubits, as opposed to bits that are used in classical communication. Photons are usually used as the media for these quantum states. By exploiting certain properties of these quantum states, quantum key distribution (QKD) provides a reliable method for transmitting secret keys across public channels without the risk of undetected eavesdropping by third parties.

1.2.1 Quantum key distribution

As discussed before, the information is usually encoded in the quantum states of photons in quantum communication. QKD enables two parties to produce a shared random secret key by measuring the quantum properties of the photons. The shared key is then used to encrypt and decrypt information.

The security of QKD relies on a basic rule of quantum mechanics known as indeterminacy: an eavesdropper (usually referred to as Eve) cannot avoid disturbing a quantum system by performing a measurement on it. Eve must in some way measure the quantum state if she wants to steal a copy of the key, so will inevitably be detected by the two communication users (Alice and Bob).

QKD is only used to generate and distribute a private key and not for transmission of any message data. The message containing confidential information can be encoded with the key based on an encryption algorithm prior to transmission over a public communication channel.

There are different schemes that have been demonstrated for performing QKD depending on the quantum properties they exploit. Here I present two examples. The first scheme is based on quantum measurements on single particles. It was proposed by Bennett and Brassard in 1984 [36, 37] and thus, is known as the BB84 protocol. Alice at one site sends Bob at another site the qubits for constructing the encryption code via a shared quantum channel. This channel is generally either an optical fibre or simply free space in the case of using single photons as qubits. In addition, the encrypted information is transmitted through a public classical channel, such as broadcast radio or the internet.

Though theoretically appealing, the experimental execution of BB84 protocol was not possible due to the lack of any single-photon source within a decade after this protocol was proposed [38, 39][40, 41].

Alternatively, Ekert proposed another protocol in 1991, the Ekert91 protocol [42]. The basic principles of this protocol are equivalent to the BB84 protocol, but it does not require single photons. It is based on the quantum properties of entangled particles which are used as resources for quantum key distribution. The protocol is illustrated in Figure 1.2. Entangled photon pairs emitted from a light source travel in opposite directions to two observers, Alice and Bob. A series of measurements are performed by Alice and Bob on their received photons, choosing the polarisation measurement basis randomly and independently. Alice and Bob then exchange the bases for their measurements over the classical communication channel. A shared key between them can be constructed due to the entanglement properties of the shared particles. Such a protocol does not protect against attacks from Eve but it provides a fail-safe way for knowing when the message has been intercepted in accordance with Bell's inequality [4].

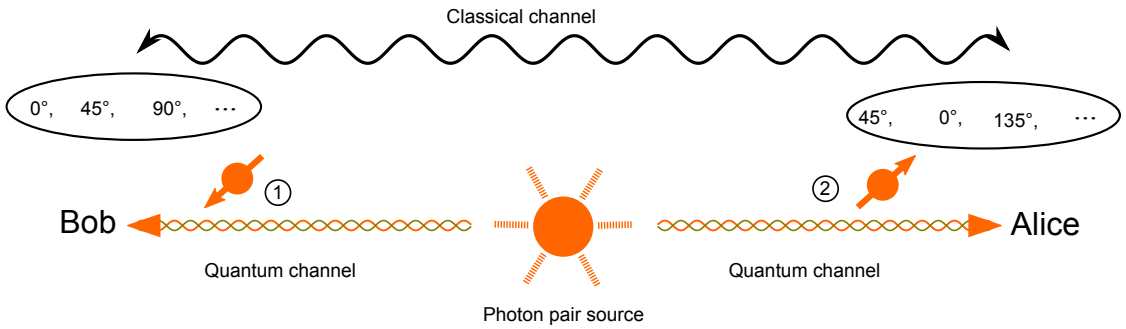

Figure 1.2: An illustration of the 'Ekert91' QKD protocol based on reference [43]. Alice and Bob share the photon pairs emitted from a EPR pair source via a quantum channel. They perform measurements based on arbitrarily chosen polarisation bases and communicate their bases over a classical (public) channel.

The entanglement-based Ekert91 protocol stands out by the feasibility of extending its distribution via entanglement swapping [44]. Thus it offers a possibility for secure long-distance quantum communication and for worldwide quantum network.

1.3 Towards long-distance quantum communication

QKD provides an unconditionally secure method for communicating information. However, the distribution of QKD over long distances is limited by several obstacles. The first one is the photon loss during transmission with optical fibres. Consider a typical type of optical fibre with an attenuation rate of $a = 0.2$ dB/km. It allows a probability of $p = 10^{aL/10}$ to distribute entanglement successfully over a distance of L (reference [45]). This probability is 0.1 at $L = 50$ km and rapidly drops to 10^{-20} at $L = 1000$ km. The other obstacle is the decoherence during transmission of quantum states, which reduces the purity of the distributed entanglement exponentially with the transmission length. For these reasons, the range of quantum communication when using direct entanglement is limited to a few hundreds of kilometres at most.

1.3.1 A quantum repeater

A feasible method to extend the range of quantum communication is to use a quantum repeater, initially proposed in 1998 by Briegel and co-workers [7]. A quantum repeater is not a single piece of equipment but a protocol for distributing entanglement, with which remote communication partners can be connected by shorter entangled sections via entanglement swapping [44] as shown in Figure 1.3. The length of each section is decided by the attenuation rate of the transmission channel. Experimental realisations of quantum repeaters were demonstrated soon after the theoretical proposal [46]. However, these earlier demonstrations had a limited range and the realisation of larger scale, real-world quantum communication was challenged by the lack of a quantum memory.

Quantum memories are crucial for a quantum repeater as the initial distribution of entanglement is a probabilistic process. Quantum memories allow for storage of the established entanglement in a given segment until the adjacent segment has also set up the entanglement. Hence the entanglement-establishing process of each segment can be operated independently. If there was no memory, the processes would have to succeed simultaneously [7]. For a segment length of 50 km, the photon loss allows a probability of $p = 10^{aL/10} = 0.1$ for successful entanglement distribution. The probability for ten segments to set up entanglement simultaneously is only 10^{-10}, the same as for direct transmission.

A milestone in the implementation of quantum repeaters and long-distance quantum communication, which fundamentally changed the above situation, is the so-called DLCZ protocol [8]. Proposed in 2001 by Duan, Lukin, Cirac and Zoller, the DLCZ protocol integrates atomic quantum memories into the linear optical system. It uses photons as 'flying qubits' and atomic states for local storage. The conversion between these two different states can be performed with high efficiency. Stationary qubits stored in the atomic quantum memories that are separated at a distance are connected by photons distributing entanglement. To be effective, these memories must store the qubits for times that are long compared to the direct optical transmission time of the channel, which is 1 ms for a 300 km link and 100 ms for 30,000 km.

1.3.2 Satellite-based free-space quantum communication

The DLCZ quantum repeater suggests a promising future for long distance quantum communication. However, when it comes to global-scale quantum communication, another

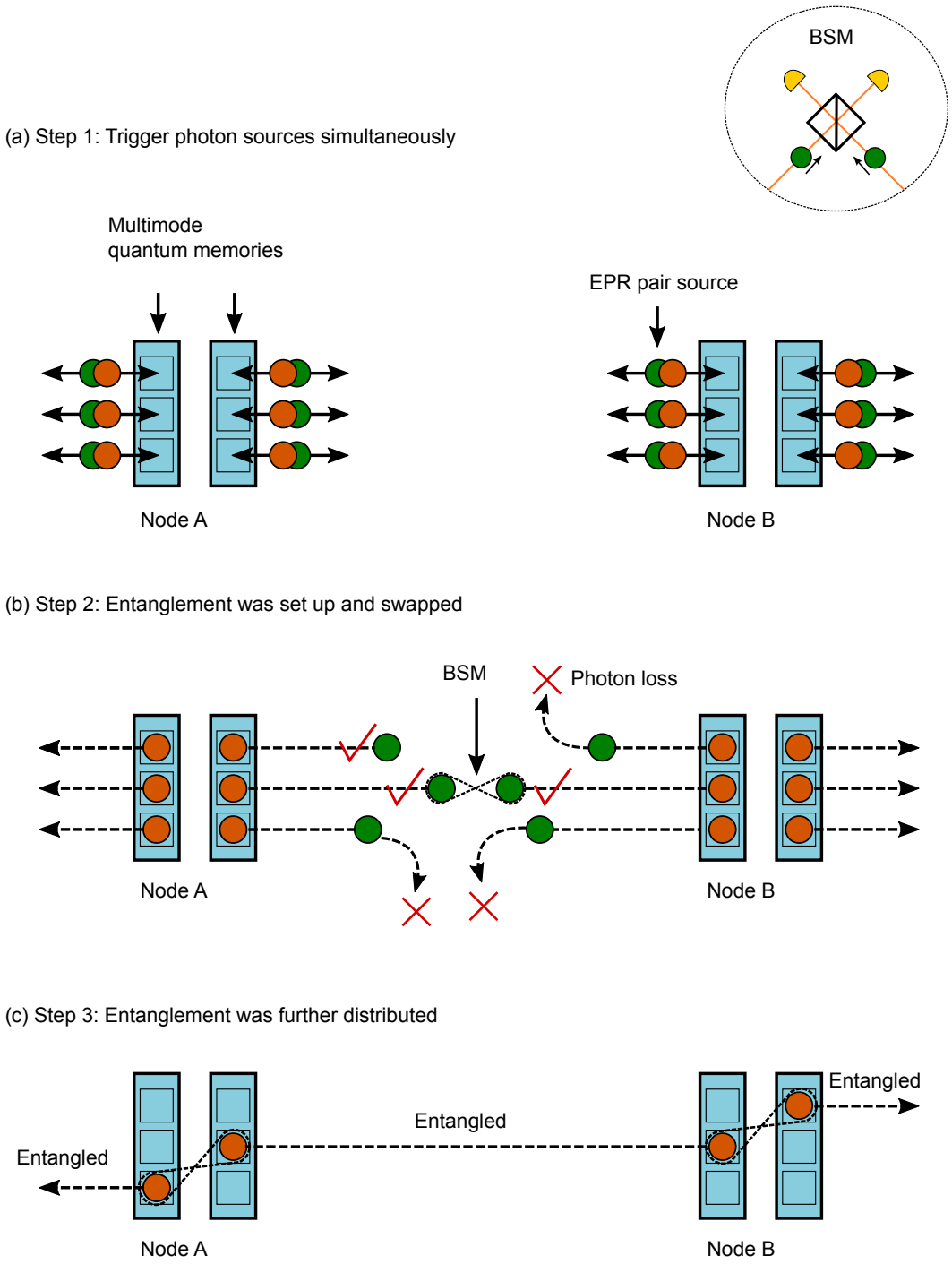

Figure 1.3: A schematic illustration of entanglement setup process between two adjacent nodes in a simplified version of quantum repeater. There are 2N (here N=3) sources of EPR photon pairs and two quantum memories allowing storage of N modes each. (a) All sources are triggered at once, with one photon of each pair sent towards the neighbouring node and the other stored in the quantum memory. (b) Entanglement is swapped via performing a Bell state measurement (BSM) on the two photons that remain. (c) Once adjacent quantum memories have both stored one excitation, entanglement is swapped to further nodes by subjecting them to a Bell state measurement. This process is repeated until entanglement is set up across the length of the desired link. The figure is reproduced with permission from [47]

promising scheme is satellite-based free-space quantum communication for which an orbiting satellite is deployed to act as a "node" [48]. The implementation of free-space quantum communication relies on the fact that there is a transmission window around 700 nm in the atmosphere where the light transmission rate is higher than 80% [49, 50]. One way to implement the scheme is shown in Figure 1.4.

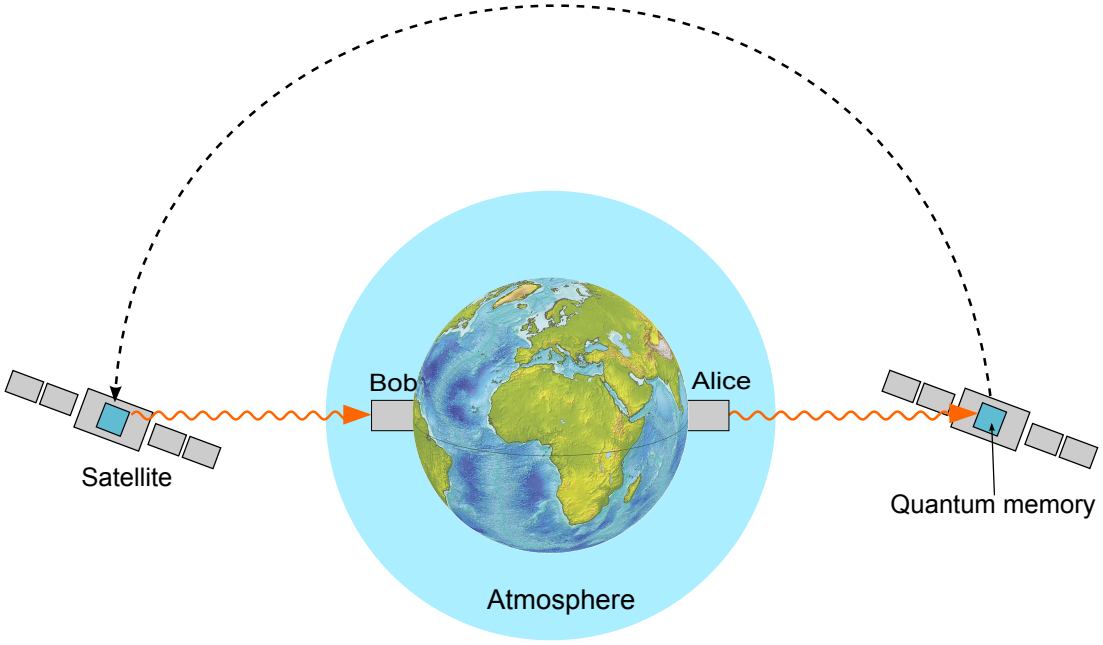

Figure 1.4: Schematic representation of a scheme of satellite based free-space quantum communication. The photonic quantum states are first sent through the atmosphere by Alice from one ground station to the satellite, where there is a quantum memory to store the quantum states, then the satellite moves. The quantum states were converted to photonic states and sent back to Bob, who is on the other site on the Earth.

The effective thickness of the atmosphere is on the order of 5-10 km (i.e., the whole outer-space atmosphere is equivalent to 5-10 km ground atmosphere) [49]. Researchers have experimentally proven the capability of preserving quantum entanglement well with a distance beyond this effective thickness [51, 52]. If the quantum state remains after penetrating the atmosphere, outer space, where the photon loss is negligible, provides the ideal environment for quantum communications. Combined with satellite technology, the free-space optical transmission allows the probability of establishing quantum communication between any two points on the globe.

The satellite-based quantum communication stepped forward by a giant step to reality in August 2016, when China launched the world's first quantum satellite. This satellite, known as QUESS (quantum experiments at space scale) satellite, contains a cryostat that produces entangled photon pairs [53].

Besides the quantum repeater and satellite links, other schemes for long distance quantum communication are possible. In particular, it would be possible to physically transport a quantum memory via the commercial transport system if many hours or even weeks of storage time is available. In this thesis, I show that this method is feasible by experimentally demonstrating a several hours long coherence time in the rare-earth solid state system Eu^{3+}:Y_2SiO_5.

1.4 Quantum memory

A quantum memory, in broad terms, is a device to store a quantum state. In the past decade, most research work on developing a quantum memory has aimed to fill the requirements of quantum communication and linear-optical quantum computation applications. Thus in this work I take the narrow definition of quantum memory, that is an 'optical' quantum memory, which is an absorber that can store and retrieve the quantum information on demand by interacting with light at optical frequencies. We can consider an ideal quantum memory as a 'sealed box' allowing for storing and recalling of the same input quantum state with 100% efficiency at any time. In reality, the sealing of the box is never perfect and there is always leakage to the rest of the universe, destructively disturbing the fragile quantum state in which the information is encoded. This process is known as decoherence of the system. Though there is no system in nature that is completely free of decoherence, certain systems have relatively energy levels that are less senstive to the environmental perturbations, allowing for a long coherence time. In particular, this is true for the internal electronic levels of atomic ensembles and the 4f-levels of rare-earth dopants in solid state hosts.

1.4.1 Atomic systems

The internal electronic levels of neutral atoms and ions provide a set of well-characterised quantum states whose interactions with the surrounding environment are well understood [54, 55]. The transitions between these levels can be manipulated via microwave or optical fields. As the ions or the atoms are weakly coupled to the environment, their electronic or hyperfine transitions, which serves as qubits for storage of quantum information, can exhibit good coherence properties.

The main challenge of working on an atomic system involves controlling the system and isolating the internal levels from the motional states. Researchers have developed a variety of techniques to tackle this challenge, laser cooling and trapping of atoms for instance. The laser cooling and trapping approach works by confining charged ions in an electromagnetic trap and using Coulomb repulsion between the ions to balance the strong external trapping potential. As the trapped ions or atoms are well separated from each other, it can be difficult to achieve strong and controllable interactions between them. However, an ensemble of individually trapped ions in a single trap is coupled by the motional states, which provides a way to set up strong interactions between them [56].

Laser cooled atomic ensembles are currently one of the most well-studied systems for light-matter interaction at the quantum level and a lot of impressive work has been demonstrated [47] following the influential DLCZ quantum repeater proposal [8]. Recent work showed a storage time of classical light for 16 s by making use of a microwave dynamic decoupling protocol [57] (dynamic decoupling protocols are discussed in Chapter 6). This work was performed in ultra-cold Rb atoms confined in a one-dimensional optical lattice, for which the ultimately achievable storage time is limited by the lifetime of the optical trap, which was measured to be 20 s.

Besides cold atomic systems, there is also significant progress towards quantum storage in room-temperature atomic systems by using dilute hot atomic vapours as described in the review paper by Bussières et al. [47]. One of the primary concerns with this system is that the atoms always have a non-zero velocity and move around in the optical field, eventually leaving the interaction region. This drifting causes the atoms to experience an

inhomogeneous driving field (phase and amplitude) and it imposes a limit on the longest storage time on the system.

1.4.2 Rare earth dopants in solids

Compared to atomic systems, quantum memories based on solid state systems provide advantages from the point of view of fundamental properties and as well as engineering feasibility. Atomic motion, which causes many challenges in working with atomic systems and ultimately limits their storage time, can be completely avoided in a solid state system. These systems can also use much larger numbers of optical centres for data storage. In addition, the properties of the solid can be tuned by adjusting the chemistry, and modern fabrication technology can be used to machine solids into a desired shape. It is also easier to integrate solid-state systems with other systems such as cavities and resonators or classical circuitry [58, 59].

The solid state system has its own disadvantages. Unlike trapped atoms or atomic gases, each atom in the solid has a different environment from each other. This causes inhomogeneous broadening on the optical transitions, which makes it more difficult to coherently manipulate the atoms. More importantly, the coherence times of optical and spin transitions are shortened in these systems due to the strong coupling to the dynamic environment. However, there is a very particular solid system, rare earth dopants in solids, which possess all the above advantages of being 'solid' but in which it is also possible to have very long coherence time for both optical and hyperfine transitions. In this system, the optically active $4f^N$ levels are used to store and manipulate the quantum information. The $4f^N$ electrons are tightly-bonded and shielded by the outer $5s^2$ and $5p^6$ orbitals (see Chapter 2). This means that the $4f^N$ levels are atom-like, even in a crystalline solid at doping densities as great as $10^{18}/\mathrm{cm}^3$ [45].

There has been remarkable progress in the development of rare-earth-based quantum memories as outlined in the review papers of Tittel in 2010 [45] Bussières in 2013 [47]. The primary achievements include storage with a retrieval efficiency of 69% [11], storage for more than 40 s [12] and the development of a rare-earth-based quantum repeater protocol [60, 61].

In this work, I focus on a particular rare-earth system, Eu^{3+}:Y_2SiO_5, a promising candidate for quantum memory applications. In our case, the quantum information is mapped on its nuclear spin states, the transition between which is expected to have an extremely long coherence time due to the measured lifetime of 23 days [17].

1.5 Thesis outline

The goal of this thesis was to study the decoherence mechanisms of the hyperfine transitions in Eu^{3+}:Y_2SiO_5 and to extend the coherence time, aiming to achieve a sufficiently long coherence time that the crystal could be used for a persistent quantum memory. A persistent quantum memory is a key component in either quantum computation or distribution of entanglement over long distance. The thesis is arranged as follows:

Chapter 2 first gives a brief introduction on the spectroscopic properties of the rare earth ions with a focus on transitions between the $4f^N$ levels. Then a more detailed description of the hyperfine energy levels structure in Eu^{3+}:Y_2SiO_5 is given. This is followed by a discussion on the spectral broadening mechanism for rare-earth ensembles, with a focus on the broadening mechanisms of the hyperfine transitions in Eu^{3+}:Y_2SiO_5.

Finally, the last section is an analysis of the mechanisms resulting in decoherence of the hyperfine transitions in Eu^{3+}:Y_2SiO_5 and the approaches that can be used to extend the coherence times.

Chapter 3 begins with an introduction of the Bloch sphere representation of a two-level system, with which the two pulse spin echo technique for measuring the coherence time was illustrated. After that, an analysis of two echo decay shapes is presented, which is followed by an introduction to DDC, a strategy for fighting decoherence. The final section talks about two methods for measuring hyperfine coherence time via the optical transition. These two methods are spectral holeburning and Raman heterodyne detection.

Chapter 4 first describes the experimental setup with a focus of the critical field alignment. Then the measurements of the coherence time using the ZEFOZ method are presented. This is followed by a demonstration of the coherence time measurements by combing the ZEFOZ and DDC. Finally, I provide a detailed analysis of the experimental results and a discussion of the possible limit of the experiments.

Chapter 5 is a detailed study on the frozen core created around an Eu^{3+} site in an applied magnetic field, aiming to work out the remaining mechanisms that still limit the coherence time of Eu^{3+} hyperfine transitions. Measurements of the Rabi frequency, coherence time, lifetime and Zeeman-transition spectrum of the frozen-core Y spins are reported.

Chapter 6 concludes the thesis and discusses the possible applications of the achieved results, the limitation of the present experiment and the potential for longer coherence time in this system.

Chapter 2

The optical spectroscopy and the hyperfine transitions of Eu^{3+}:Y_2SiO_5

The rare-earth (RE) elements have been the focus of experimental investigation for many decades. This has led to the development of many applications, including fluorescent lamps, laser materials and optical amplifiers for telecommunications.

The observation of narrow optical lines [62, 63] was a key property that motivated the study and technological development of the rare-earth ions. The optical lines are from transitions between the electronic states within a $4f^N$ configuration of divalent (RE^{2+}) or trivalent RE ions (RE^{3+}) doped into transparent host materials, such as $Y_3Al_5O_{12}$, Y_2SiO_5 (YSO) and Y_2O_3. The $4f^N$ configuration for RE ions is unique in solids because the $4f$ electrons are shielded from the crystalline environment by the outer $5s$ and $5p$ electrons and couple only weakly to ligand electrons and lattice vibrations. Thus RE ion doped solids have spectral properties more akin to trapped ions than other optical centres in solid state hosts. The $4f^N$ transitions exhibit excellent coherence properties, and unlike trapped ions, large optical depths are readily achieved.

Because of these characteristics, there has been interest in using rare-earth doped solids as a physical system for quantum memory applications. The storage time of a quantum memory is limited by the coherence time of the transition on which information is stored. In RE doped solids, the longest coherence time observed for optical transitions is 4.8 ms in Er^{3+}:Y_2SiO_5 [64]. This optical coherence time is long compared to many other systems that are considered for developing quantum memories, but much longer coherence time can be achieved for hyperfine transitions. Previous experiments involving Pr^{3+} doped into Y_2SiO_5 have demonstrated hyperfine coherence times exceeding 40 seconds [10, 12]. This thesis investigates the hyperfine decoherence mechanisms of Eu^{3+}:Y_2SiO_5, in an attempt to achieve still longer coherence times. While the above coherence time (40 seconds) of Pr^{3+}:Y_2SiO_5 is already very close to being lifetime limited, the hyperfine lifetime of Eu^{3+}:Y_2SiO_5 is up to 23 days [17]. This gives a significantly longer upper limit, and makes Eu^{3+}:Y_2SiO_5 a promising candidate of the development of long-term quantum memories.

At the beginning of this chapter, a brief review of the spectroscopic properties of rare-earth ions is presented. This is followed by a more detailed description of the hyperfine structure and spin Hamiltonian parameters of Eu^{3+} in Y_2SiO_5. Then I present a discussion on the spectral broadening mechanisms for rare-earth ensembles with a focus on the broadening mechanisms of the hyperfine transitions in Eu^{3+}:Y_2SiO_5. Finally, in

the last section, a detailed analysis on the feasible methods to suppress the mechanisms that broaden the homogeneous linewidth of the hyperfine transitions in Eu^{3+}:Y_2SiO_5 is presented. Then the expected coherence time is presented according to this analysis.

2.1 Introduction to rare earths

The rare earths, or lanthanides, are a group of elements with very similar chemical and physical properties. They comprise the 15 elements in the periodic table from lanthanum (57) to lutetium (71). These elements all exhibit strong electropositivity and the most stable oxidation state is generally RE^{3+}, resulting in the electronic configuration $4f^N$ as shown in Table 2.1. scandium and Y^{3+} are often included in the class of rare earths because they share their trivalent oxidation state and have a similar ionic size.

Atomic number	Element	Electronic configu-	Ground state	Ionic radius (pm)
21	Sc	$3d^0$	$^1S_0$	87.0
39	Y	$4d^0$	$^1S_0$	101.9
57	La	$4f^0 5s^2 5p^6$	$^1S_0$	116.0
58	Ce	$4f^1 5s^2 5p^6$	$^2F_{5/2}$	114.3
59	Pr	$4f^2 5s^2 5p^6$	$^3H_4$	112.6
60	Nd	$4f^3 5s^2 5p^6$	$^4I_{9/2}$	110.9
61	Pm	$4f^4 5s^2 5p^6$	$^5I_4$	109.3
62	Sm	$4f^5 5s^2 5p^6$	$^6H_{5/2}$	107.9
63	Eu	$4f^6 5s^2 5p^6$	$^7F_0$	106.6
64	Gd	$4f^7 5s^2 5p^6$	$^8S_{7/2}$	105.3
65	Tb	$4f^8 5s^2 5p^6$	$^7F_6$	104.0
66	Dy	$4f^9 5s^2 5p^6$	$^6H_{15/2}$	102.7
67	Ho	$4f^{10} 5s^2 5p^6$	$^5I_8$	101.5
68	Er	$4f^{11} 5s^2 5p^6$	$^4I_{15/2}$	100.4
69	Tm	$4f^{12} 5s^2 5p^6$	$^3H_6$	99.4
70	Yb	$4f^{13} 5s^2 5p^6$	$^2F_{7/2}$	98.5
71	Lu	$4f^{14} 5s^2 5p^6$	$^1S_0$	97.7

Table 2.1: The electronic configuration and ground states of the trivalent rare earth ions RE^{3+}. The ionic radii are from [65].

The rare earth ions distinguish themselves by their partially occupied $4f$ orbitals. The $4f^N$ shell sits inside the $5s$ and $5p$ sub-shells, both of which are completely filled. Hence the electrons in the $4f^N$ shell have atomic-like localised states, being shielded from interacting with the crystal field. Figure 2.1 shows, with Gd^+ as an example, the radial distribution of electrons in the outer four shells. It is obvious that the $4f$ shell is deeply imbedded inside the $5s$ and $5p$ shells.

While the $4f$ electrons are well shielded from the crystal field, they are not well shielded from the nucleus. The effective charge of the nucleus grows as the atomic number

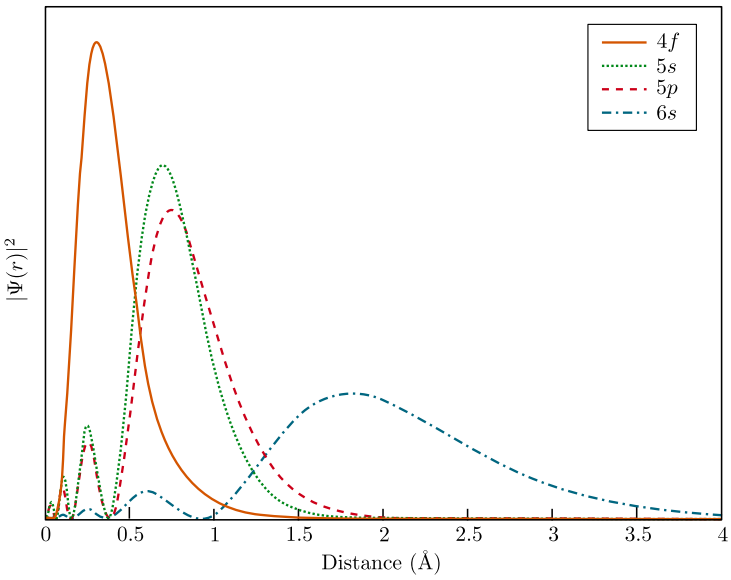

Figure 2.1: The calculated radial probability distribution for the 4f, 5s, 5p and 6s orbitals of Gd^+. This figure is reproduced based on [66].

increases, which enhances the attraction to the outer electrons. This results in a gradual decrease in the radius across the lanthanide ions, known as the lanthanide contraction. Thus, as shown in Table 2.1, while lanthanum has a larger radius than Y^{3+}, the radius of erbium is similar to Y^{3+}.

2.1.1 Energy levels of $4f$ electrons

An exact solution of the Schrödinger equation is not possible for a multi-electron system. However, due to the well-shielded crystalline environment, the Hamiltonian of the $4f$ electrons of rare earths in solids is very similar to that of the free ion. Thus, we can use a free-ion approximation in which the electron-nucleus, electron-electron and the spin-orbit interactions are described by a free-ion Hamiltonian while the remaining effect of the crystal field is treated as a perturbation to this Hamiltonian. The energy level scales corresponding to different interaction mechanisms of rare earths in solids is listed in Table 2.2 and the method for solving the Schrödinger equation to get these splittings, using the free-ion approximation, is briefly described in the following paragraphs.

The free-ion energy levels are formed through three steps. First, a Hamiltonian is formed in the central field approximation, composed of two components. One is the Coulomb attraction between the electrons and the nucleus. The other is the central part of the Coulomb repulsion between the electrons. In the framework of this approximation, all the $n = 4$ energy levels are degenerate. The degeneracy in n is then lifted by the non-central part of the Coulomb repulsion. At this stage, the energy levels can be specified by the definite orbital angular momentum $L = \sum_{i=1}^{N} l_i$ and the spin angular moment $S = \sum_{i=1}^{N} s_i$, where l_i and s_i are the orbital angular and spin angular momentum for the i-th electron. Degeneracy of these energy levels is further lifted by the spin-orbit coupling, which mixes states whose L and S are different, but whose total angular momenta J are identical. As this mixing is significant, the orbital (L) and spin (S) angular momentum

are no longer good quantum numbers. The energy levels of the free ion are labelled according to the total angular momentum $J = L + S$. This brings about the familiar Russell-Saunders symbol $^{2s+1}L_J$ where each J level is $2J + 1$ degenerate. The L and S values are approximations by using the numbers with the largest contribution. While the S and L values are specified numerically, the L values are specified using letters as $L = S,P,D,F,G,H$, corresponding to $L = 0,1,2,3,4,5$.

Interaction mechanism	Energy splitting (cm^{-1})	Energy splitting (Hz)
Configuration splitting ($4f^N \rightarrow 4f^{N-1}5d$)	10^5	10^{15}
Splitting within a $4f^N$ configuration:		
Non-central Coulomb	10^4	10^{14}
Spin-orbit interaction	10^3	10^{13}
Crystal field interaction	10^2	10^{12}
Hyperfine splitting (nuclear spin)	$10^{-3} - 10^{-1}$	10^7-10^9
Superhyperfine splitting(ion-host nuclear spin)	$10^{-4} - 10^{-2}$	10^6-10^8

Table 2.2: Approximate scale of the Hamiltonian contributions for rare-earth ions in solid hosts. This table is reproduced from [67].

The $(2J + 1)$ degeneracy of the energy levels is lifted or partially lifted by the crystal field for a rare earth ion in a solid. The degree to which the degeneracy in J is lifted depends on the symmetry of the ion site and the number of electrons the ion has. For ions with an even number of electrons (non-Kramers ions), the degeneracy is completely lifted in sites of less than axial symmetry, such as the Y^{3+} sites in Y_2SiO_5. The rare-earth ions in this case have no electronic magnetic moment to first order and hence are much less sensitive to magnetic fields. For ions with an odd number of electrons (Kramers ions), the crystal field levels remain doubly degenerate even in the case of a low-symmetry site, which is known as Kramers' degeneracy. The doublet states are split by an external magnetic field.

Figure 2.2 is the famous Dieke diagram of energy levels of the trivalent rare-earth ion in a solid. First created by Dieke in 1963 [68], it was extended by Carnall et al. in 1989 [69]. The Hamiltonian for these energy levels consists of the free-ion and crystal field. The splittings due to crystal field interaction are not resolved in this diagram, and the scale of splitting is indicated by the thickness of the lines. Though the levels shown in the diagram are for RE^{3+}:LaF_3, the splittings are similar for different host materials.

Transitions between the levels in Figure 2.2 are electric or magnetic dipole transition. For free rare-earth ions, the 4f-4f transitions are parity forbidden because the electric dipole operator only links states with different parity. However, once the rare-earth ions are placed in non-centrosymmetric sites in a solid, the states of configurations with opposite parity, such as $4f^{N-1}5d$ or $4f^{N-1}5p$, are mixed into the $4f^N$ configuration [67]. Thus the 4f-4f transitions become weakly allowed.

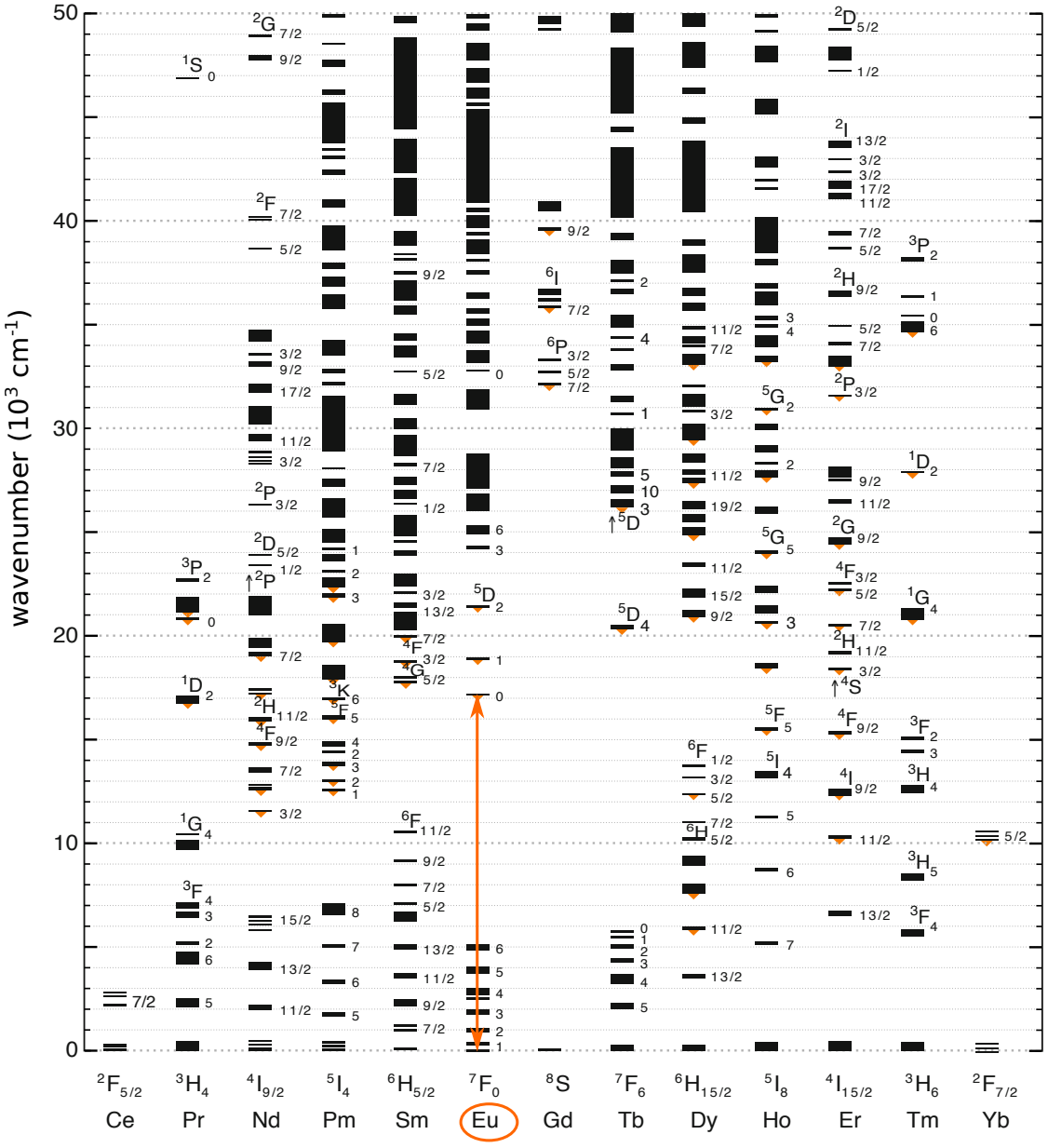

Figure 2.2: The classic Dieke chart of energy levels in RE^{3+}:LaF_3 based on calculated free-ion and crystal-field splittings [70]. The $^7F_0 \rightarrow {}^5D_0$ transition of Eu^{3+} studied in this thesis is indicted by the orange arrow.

2.2 Spectral properties of Eu^{3+}:Y_2SiO_5

The experiments described in this thesis were conducted in Eu^{3+}:Y_2SiO_5. This section describes properties specific to the host crystal Y_2SiO_5 and for the Eu^{3+} ion in this material.

The host crystal Y_2SiO_5 is monoclinic and belongs to the C_{2h}^6 space group with four formula units per unit cell. The detailed crystal structure and cell parameters are listed in Table 2.2. Being monoclinic, the crystal is optically biaxial and the optical extinction axes are commonly used to orient the crystal in an experiment. As shown in Figure 2.3, one extinction axis coincides with the crystallographic b axis, which has C_2 symmetry, while the other two, labelled D_1 and D_2, lie in the a-c plane, with D_1 23.8° from the c axis, 78.7° from the a axis and perpendicular to the D_2 axis [71].

Cell parameters:	$a = 10.419$ Å, $b = 6.726$ Å, $c = 12.495$ Å, $\beta = 102°39'$		
Schoenflies:	C_{2h}^6 (no. 15 in inter. labels of cryst.)		
Element	x/a	y/b	z/c
Y(1)	0.30657	0.37701	0.14154
Y(2)	0.42839	-0.25506	-0.03701

Table 2.3: The crystal structure and cell parameters of Y_2SiO_5 [71]. The constants a, b, c and β are the cell parameters, with β the angle between a and c. The Y^{3+} positions listed are to be used in Section 2.5.

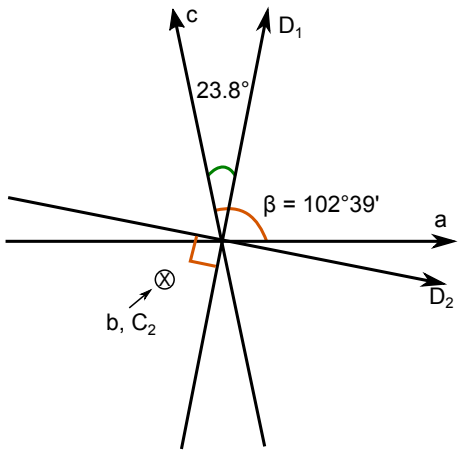

Figure 2.3: The orientation of the D_1, D_2 and C_2 axes relative to the crystallographic axes (a, b, and c) in Y_2SiO_5 with C_2 along b axis and the other two axes in the $a - c$ plane [71].

Eu^{3+} ions can substitute the Y^{3+} ions in Y_2SiO_5 in one of two crystallographically inequivalent sites of C_1 symmetry. These two sites, referred to as Site 1 and Site 2, have different frequencies for the same transition. The transition of interest in this work is the $^7F_0 \rightarrow {}^5D_0$ transition, which occurs at 579.879 nm for Site 1 and 580.049 for Site 2 [67]. Each crystallographically identical site consists of a pair of magnetically inequivalent sites, related by a rotation about the crystal's C_2 axis. The work reported in this thesis focus on one of the magnetic site of Site 1.

The $^7F_0 \rightarrow {}^5D_0$ transition of Eu^{3+} is unique among all the $4f \rightarrow 4f$ transitions of the rare earths in that both the ground and excited states are $J = 0$ singlet levels. These levels have very weak magnetic and crystal field interactions with the lattice. In many symmetries, the $J = 0$ to $J = 0$ transition is completely forbidden according to the Judd-Ofelt theory [72, 73]. Such a transition can become weakly allowed for sites belonging to the polar point groups [74], which comprise C_1, C_s, C_n and C_{nv} (for $n = 2, 3, 4, 6$). In these symmetries, the $0 \rightarrow 0$ transition becomes allowed because the $J = 2$ levels are mixed into the $J = 0$ ground state. However, the oscillator strength is generally weaker than other rare-earth systems, and is dependent on the host material. For the $^7F_0 \rightarrow {}^5D_0$ transition in Eu^{3+}:Y_2SiO_5, the oscillator strength is 10^{-8} [17].

2.3 Hyperfine energy levels of Eu^{3+}:Y_2SiO_5

2.3.1 Spin Hamiltonian

The hyperfine structure of Eu^{3+}:Y_2SiO_5 is determined by a number of interactions and is often described by introducing the Hamiltonian [75]

$$H = [H_{FI} + H_{CF}] + [H_{HF} + H_Q + H_Z + H_z]. \tag{2.1}$$

In this equation, the six terms are the free-ion Hamiltonian H_{FI}, the crystal field Hamiltonian H_{CF}, the hyperfine interaction H_{HF}, the nuclear electric quadruple interaction H_Q, the electronic Zeeman interaction H_Z and the nuclear Zeeman interaction H_z. The first group $[H_{FI}+H_{CF}]$ are of a much larger order than the second group $[H_{HF}+H_Q+H_Z+H_z]$, and determine the electronic energy levels. The four terms of the second group in Equation 2.1 are of similar magnitude and it is the perturbation from these terms that determines the hyperfine structure to the electronic levels.

In most non-Kramers' ions in a non-centrosymmetric site, the crystal field quenches the electronic angular momentum, so that there is no first order but there is a second order contribution from the hyperfine interaction H_{HF} and the electronic Zeeman interaction H_Z due to interactions with nearby crystal field levels. But this is not the case for the $^7F_0$ and $^5D_0$ levels of Eu^{3+}, since these levels are true electronically singlets so there are no other J multiplets to interact with. However, Eu^{3+} does have admixtures with other J states contributing to the Hamiltonian of the $J = 0$ states, which gives rise to a similar Hamiltonian to that seen in other non-Kramers' systems. The behaviour of a single electronic level can then be described by a reduced spin Hamiltonian [75, 76]

$$H = (\boldsymbol{B} \cdot (g_J^2 \mu_B^2 \boldsymbol{\Lambda}) \cdot \boldsymbol{B})\hat{\boldsymbol{E}} + \boldsymbol{B} \cdot (\gamma_N \boldsymbol{E} + 2A_J g_J \mu_B \boldsymbol{\Lambda}) \cdot \hat{\boldsymbol{I}} + \hat{\boldsymbol{I}} \cdot (\boldsymbol{P_Q} + 2\boldsymbol{T_Q}) \cdot \hat{\boldsymbol{I}}, \tag{2.2}$$

where the tensor $\boldsymbol{\Lambda}$ and the tensor $\boldsymbol{P_Q}$ are determined by the admixtures between the $J = 0$ and the nearby $J \neq 0$ states. In particular, for the $^7F_0$ state, the mixing is with the $^7F_1$ and $^7F_2$ state. Also

- g_J is the Lande g-value, $g_J = \frac{3}{2} - \frac{L(L+1)-S(S+1)}{2J(J+1)}$
- μ_B is the Bohr magneton,
- $\boldsymbol{B}$ is the vector of the magnetic field,
- γ_N is the nuclear gyromagnetic ratio,

- $\hat{\boldsymbol{I}}$ is the vector nuclear spin operator,
- $\boldsymbol{E}$ is the 3×3 identity matrix,
- $\hat{\boldsymbol{E}}$ is the identity operator,
- A_J is the magnetic hyperfine interaction parameter for a given J state,
- $\boldsymbol{T_Q}$ is the tensor describing the nuclear quadrupole interaction, also known as the true quadrupole tensor.

The first term of Equation 2.2 is the quadratic electronic Zeeman shift which is due to the second order hyperfine interaction. The term $2A_J g_J \mu_B \boldsymbol{B} \cdot \boldsymbol{\Lambda} \cdot \boldsymbol{I}$ has the same form as the nuclear Zeeman interaction $\gamma_N \boldsymbol{B} \cdot \boldsymbol{I}$, both of which are linear with magnetic field and can be combined to be described by an enhanced nuclear Zeeman tensor. The $\boldsymbol{P_Q}$ tensor and the true quadrupole tensor $\boldsymbol{T_Q}$ have the same format and can be combined into a total quadrupole tensor. This leads to a simplified form of Equation 2.2:

$$H = (\boldsymbol{B} \cdot \boldsymbol{Z} \cdot \boldsymbol{B})\hat{\boldsymbol{E}} + \boldsymbol{B} \cdot \boldsymbol{M} \cdot \hat{\boldsymbol{I}} + \hat{\boldsymbol{I}} \cdot \boldsymbol{Q} \cdot \hat{\boldsymbol{I}}. \tag{2.3}$$

The quadratic electronic Zeeman term is described by $\boldsymbol{Z}$, the quadratic Zeeman tensor. The second term is the enhanced nuclear Zeeman Hamiltonian where $\boldsymbol{M}$ is the effective Zeeman tensor. The tensors $\boldsymbol{Z}$ and $\boldsymbol{M}$ are anisotropic and share the same principal axes given by the tensor $\boldsymbol{\Lambda}$. The tensor $\boldsymbol{Q} = \boldsymbol{P_Q} + \boldsymbol{T_Q}$ is the effective quadrupole tensor, including the true quadruple and the admixture interactions. Because the system investigated has less than axial symmetry, the tensor $\boldsymbol{Q}$ does not have the same principal axes as $\boldsymbol{P_Q}$, $\boldsymbol{T_Q}$ or $\boldsymbol{M}$. For the ground state $^7\mathrm{F}_0$ and excited state $^5\mathrm{D}_0$, because the tensor $\boldsymbol{\Lambda}$ and the tensor $\boldsymbol{P_Q}$ in Equation 2.2 are different, the tensor $\boldsymbol{Q}$ or $\boldsymbol{M}$ have different values and principal axes.

2.3.2 Hyperfine structure

As mentioned earlier, the electronic $^7\mathrm{F}_0 \rightarrow {}^5\mathrm{D}_0$ transition of Eu^{3+} involved in this thesis is a special case among $4f - 4f$ transitions of rare earth ions in solids as both the ground and excited states are electronically non degenerate $J = 0$ levels. This results in a very weak coupling between the transition and the magnetic and crystal field of the host lattice. The remaining weak interaction is due to slight mixtures of the nearby $J = 1, 2$ states. As the $^7F_0 \rightarrow {}^7F_1$ separation ($\approx$ 10 THz) is much smaller than $^5D_0 \rightarrow {}^5D_1$ separation ($\approx$ 30 THz), the admixture is larger in the $^7F_0$ state than the $^5D_0$ state. Though the admixture of the nearby $J = 1, 2$ states is larger in $^7\mathrm{F}_0$ than that in $^5\mathrm{D}_0$, the magnitude of the hyperfine quadrupole splittings in the ground $^7\mathrm{F}_0$ state is significantly smaller than those in the excited $^5\mathrm{D}_0$ state. This is because the different contributions to the effective quadruple tensor $\boldsymbol{Q}$ of $^7\mathrm{F}_0$ have opposite signs and they cancel each other [67].

Natural Eu^{3+} has two isotopes, ^{151}Eu and ^{153}Eu, with roughly equal abundance. Both isotopes have a nuclear spin of 5/2. At zero field, the $J = 0$ singlets are split by the nuclear quadrupole interactions into three doubly degenerate hyperfine levels. The zero field hyperfine splitting frequencies of the $^7\mathrm{F}_0$ and $^5\mathrm{D}_0$ states in Eu^{3+}:Y_2SiO_5 are listed in Table 2.4. The transitions involved in this work are the splittings of $^{151}Eu^{3+}$ ions occupying Site 1 Y^{3+} positions as shown shown in Figure 2.4.

In an external magnetic field, the degeneracy of the nuclear spin states is lifted and the three pairs of hyperfine levels are split into six levels as shown in Figure 2.4. The quadratic

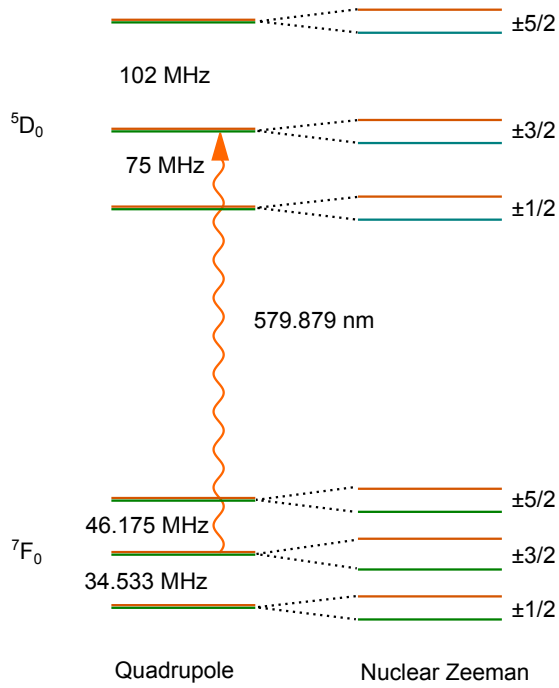

Figure 2.4: Hyperfine energy levels for Site 1 Eu^{3+} ions in $^{151}Eu^{3+}$:Y_2SiO_5. This thesis focusses on the hyperfine transitions of the $^7F_0$ state, but it involves the optical transition, as marked, during measurements. The hyperfine splitting are from [67]. Though the hyperfine levels are labelled with the spin states ($\pm 5/2$, $\pm 3/2$ and $\pm 1/2$), this labelling is not accurate due to the mixture between different spin states.

	^{151}Eu, Site 1 (MHz)	^{153}Eu, Site 1 (MHz)	^{151}Eu, Site 2 (MHz)	^{153}Eu, Site 2 (MHz)
$^7F_0$	34.533[a]	90.0	29.527[a]	76.4
	46.175[a]	119.2	57.254[a]	148.1
$^5D_0$	75	191	63	160
	102	260	108	274

Table 2.4: Hyperfine splittings for Eu^{3+}:Y_2SiO_5. The transition frequencies labelled as [a] are from Könz [17] and other values are from Yano et. al. [77, 78]. This table is reproduced from [67].

Zeeman term in Equation 2.3 does not contribute to the hyperfine splittings as it causes the same shift for different nuclear spin states. This term is ignored when discussing the hyperfine splittings. So the spin Hamiltonian of Equation 2.3 can be simplified as

$$H = \boldsymbol{B} \cdot \boldsymbol{M} \cdot \hat{\boldsymbol{I}} + \hat{\boldsymbol{I}} \cdot \boldsymbol{Q} \cdot \hat{\boldsymbol{I}}. \tag{2.4}$$

For the non-axial sites of Y_2SiO_5, tensors $\boldsymbol{M}$ and $\boldsymbol{Q}$ have different orientation and can be written

$$\boldsymbol{M} = R(\alpha_M, \beta_M, \gamma_M) \begin{bmatrix} \gamma_1 & 0 & 0 \\ 0 & \gamma_2 & 0 \\ 0 & 0 & \gamma_3 \end{bmatrix} R^T(\alpha_M, \beta_M, \gamma_M), \tag{2.5}$$

$$\boldsymbol{Q} = R(\alpha_Q, \beta_Q, \gamma_Q) \begin{bmatrix} -E & 0 & 0 \\ 0 & E & 0 \\ 0 & 0 & D \end{bmatrix} R^T(\alpha_Q, \beta_Q, \gamma_Q), \tag{2.6}$$

where $R(\alpha, \beta, \gamma)$ is the rotation matrix defining the orientation between an external coordination system and the principal axes of the tensors, and is described by three Euler angles

$$R(\alpha, \beta, \gamma) = \begin{bmatrix} \cos\alpha & -\sin\alpha & 0 \\ \sin\alpha & \cos\alpha & 0 \\ 0 & 0 & 1 \end{bmatrix} \times \begin{bmatrix} \cos\beta & 0 & \sin\beta \\ 0 & 1 & 0 \\ -\sin\beta & 0 & \cos\beta \end{bmatrix} \times \begin{bmatrix} \cos\gamma & -\sin\gamma & 0 \\ \sin\gamma & \cos\gamma & 0 \\ 0 & 0 & 1 \end{bmatrix}. \tag{2.7}$$

As shown in the above equations, the ground state $^7F_0$ and the excited state $^5D_0$ each have six parameters determining the tensor $\boldsymbol{M}$ and five parameters determining the tensor $\boldsymbol{Q}$. These tensors are different for the two magnetically inequivalent subsites contributing to a single crystallographic site. The tensors for one subset can be obtained by rotating the tensors of the other subset around the C_2 axis. For example, for the tensor $\boldsymbol{M}$:

$$\boldsymbol{M_1} = R_{C_2} \cdot \boldsymbol{M_2} \cdot R'_{C_2}, \tag{2.8}$$

where R_{C_2} is the rotation matrix about C_2-axis while $\boldsymbol{M_1}$ and $\boldsymbol{M_2}$ are the $\boldsymbol{M}$ tensors for the two magnetic subsets respectively. Since the tensors are different, the hyperfine splittings are different for the two subgroups in the presence of a magnetic field, thus, there is a pair of lines corresponding to the same transition as shown in Figure 4.9(b). The parameters defining the $\boldsymbol{Q}$ and $\boldsymbol{M}$ tensor and the C_2 axis of the ground state hyperfine levels for crystallographically Site 1 on $^{151}Eu^{3+}$:Y_2SiO_5 were worked out by Longdell et

al. [22] and are listed in Table 2.5.

Quantity	Value	Fit uncertainty	Units
α_M	144.9	0.1	degrees
β_M	34.9	0.1	degrees
γ_M	98.1	0.6	degrees
γ_1	4.43	0.02	MHz/T
γ_2	5.682	0.007	MHz/T
γ_3	11.183	0.010	MHz/T
$C_2\theta$	10.11	0.03	degrees
$C_2\phi$	165.2	0.2	degrees
α_Q	-39.3	0.2	degrees
β_Q	76.49	0.06	degrees
γ_Q	149.9	0.1	degrees
E	2.73500	0.00007	MHz
D	12.3797	0.0001	MHz

Table 2.5: Spin hamiltonian parameters for $^{151}Eu^{3+}$:Y_2SiO_5 hyperfine ground $^7F_0$ state. These parameters are defined in the coordinate frame of the magnetic field used during the experimental determination [22]. $C_2\theta$ and $C_2\phi$ are the elevation and azimuth angle of the C_2 orientation.

2.4 Broadening of spectral lines

An ensemble system of rare earth ions can never be made completely isolated so there is always interaction between the ion of interest and the surrounding environment, which results in the broadening of the transition. This broadening can be classified on the basis of the time scale it occurs over into inhomogeneous broadening, homogenous broadening and spectral diffusion. Inhomogneous broadening is due to interactions with the environment that are static with time, while homogeneous broadening is a dynamic process happening on a time scale that is much faster than the measurement. Spectral diffusion is a process mid-way between the two, which occurs on a time scale comparable to that of the measurement. This section talks about the broadening mechanisms for rare earth solid state systems and the focus is on the broadening of the hyperfine transitions in Eu^{3+}:Y_2SiO_5.

2.4.1 Inhomogeneous broadening

In a doped solid, there are static variations in the strain, electric or magnetic field experienced by a dopant ion from site to site, which results in an inhomogeneous distribution of the dopant's transition frequencies. As shown in Figure 2.5(a), different ion subgroups have different transition frequencies. The frequencies from the whole ensemble forms an inhomogneneous broadening profile as shown in Figure 2.5(b). The variation of the crystalline environment causing this static frequency broadening is generally due to crystal defects such as vacancies, interstitials, impurities, growth defects, ions in different valence states or trapped electrons or holes.

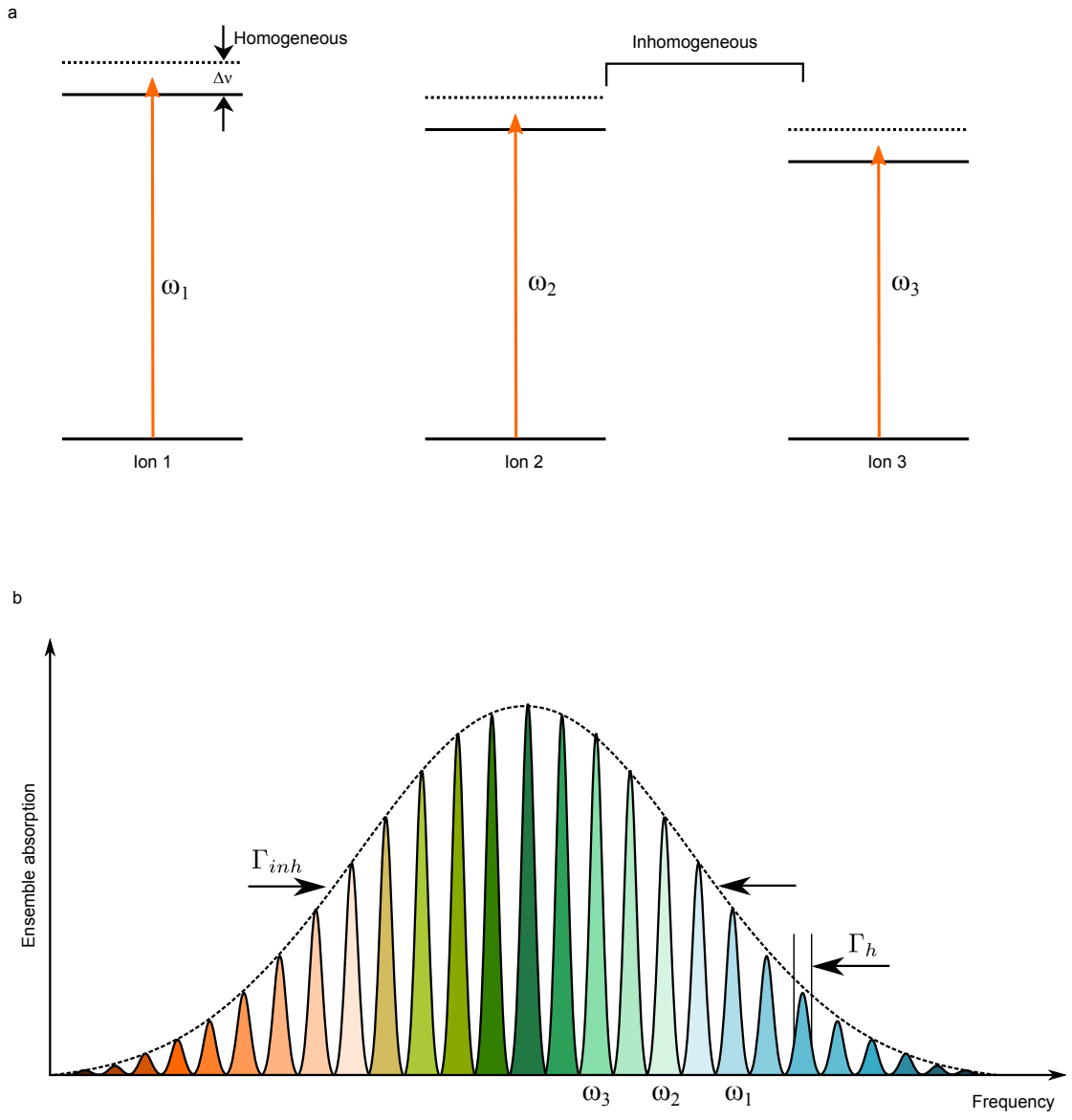

Figure 2.5: (a), Three ion subgroups are used to illustrate the homogeneous and inhomogeneous broadening. The inhomogeneous broadening is that the transition frequency for each ion subgroup is different. It is ω_1, ω_2 and ω_3 for Ion 1, Ion 2 and Ion 3 respectively. The homogeneous broadening is that the frequency for each ion subgroup is altered dynamically within the identical region of $\Delta\nu$. (b), The inhomogeneous absorption profile of an ensemble of ions is the sum of the homogeneous profile of the different individual ions. The transition frequencies of the three ions are indicated in the inhomogeneous profile. This diagram is not to scale, the actual ratio between inhomogeneous linewidth Γ_{inh} and homogeneous linewidth Γ_{h} is much larger.

The rare earths in solids have an inhomogeneous linewidth ranging from 10 MHz to more than 100 GHz for optical transitions. This linewidth is dominated by the static strain in the lattice for the system under consideration [67], and, for non-singlet levels, by static magnetic fields as well [79]. In zero magnetic field, only the second-order contributions to the quadruple tensor from the electronic states cause inhomogeneous broadening on hyperfine transitions. The inhomogeneous linewidth of hyperfine transitions is typically at the kHz to 100kHz scale, which is much narrower than that of optical transitions. In the presence of an external magnetic field, the field inhomogeneity can contribute to both the optical and the hyperfine inhomogeneous linewidth.

Both the optical and the hyperfine inhomogeneous linewidths are dependent on the host material, growth conditions and dopant concentrations. For instance, the dopants are usually mismatched in size with the ions they replace, causing distortion in the lattice, which results in strain in the crystal environment. The lattice distortion grows as the concentration is increased. In order to minimise the strain, a common choice is to replace a host ion of similar size and at low concentration. Thus, it is common to use Y^{3+} hosts, such as Y_2SiO_5 and Y_2O_3, for rare earth ions, given that the Y^{3+} ions, which are to be substituted, have a similar ionic radius with the rare earth ions as shown in Table 2.1.

2.4.2 Lifetime

While the inhomogeneous broadening is static, the homogeneous and spectral diffusion are dynamic processes. To understand these dynamic processes, I will first give a brief discussion of the lifetime T_1 of the excited state of the transition. The lifetime T_1 can be written [79]:

$$\frac{1}{T_1} = \Gamma_r + \sum_i \Gamma_{nr,i}\,. \tag{2.9}$$

T_1 includes both radiative and non-radiative processes. For optical transitions within the $4f^n$ configuration, the radiative decay rate is generally very low, in the kHz or sub kHz regime, due to the weak oscillator strength. This is because these transitions are parity, and often angular momentum forbidden in the free ion, but become weakly allowed when occupying dopant sites in a solid of low symmetry. Non-radiative decay involves the coupling between the electrons and phonons. The phonon processes involved include the direct one-phonon process and higher order processes where two or multiple phonons are involved [80, 81]. The direct phonon decay rate is dependent on the energy gap [82] and the energies of the phonon modes [83]. For the lowest states in J multiplets, the $^5D_0$ level of Eu^{3+} for instance, there is a large energy gap ($\sim$ 10,000 cm^{-1}) beneath it to the next lowest energy level ($^7F_6$). Hence, the contribution to the lifetime of the direct phonon process can be neglected [17]. Higher order processes dominate dephasing at room temperature, but exhibit temperature dependence as T^2 at temperatures higher than the Debye limit and as T^7 at temperatures much lower than the Debye limit [17, 67]. These processes are generally negligible at temperatures below 4 K.

For hyperfine transitions, the radiative decay rate is extremely low and can be ignored. The direct one-phonon process is also very slow because phonons of low-frequency modes, though strongly populated, have a small coupling constant with quadruple coupling due to their long wavelengths. The main spin-lattice relaxation mechanisms, then, are the Orbach process [80] and inelastic Raman scattering of phonons [81]. The system under consideration in this thesis is the ground state hyperfine levels in Eu^{3+}:Y_2SiO_5, the spin-lattice relaxation mechanism of which has been well studied by Könz et al. [17]. By

measuring the hyperfine lifetime at different temperatures from 2 K to 17 K as shown in Figure 2.6, they showed a temperature dependence given by

$$T_1 = \left[\frac{A}{e^{\delta E/kT} - 1} + BT^7\right]^{-1}. \tag{2.10}$$

The first term in the right describes the Orbach process which involves absorbing a phonon from $^7\mathrm{F}_0$ to $^7F_1$ and then re-emitting to a different hyperfine level. The intensity of the Orbach process is dependent on the number of phonons with energy equal to the $^7\mathrm{F}_0 \rightarrow {}^7F_1$ energy gap $\delta E = 201$ cm^{-1} [17]. The second term on the right is the Raman process which describes the inelastic scattering of phonons, scaling with temperature as T^7. The Orbach coefficient is $A = 3.7\times10^8$ Hz and the Raman coefficient is $B = 1.1\times10^{-10}$ Hz/K^7. It was demonstrated that the Orbach process dominates at temperatures higher than ~12 K while the Raman process takes over below 12 K. At 2 K, the measured lifetime is up to 23 days for Site 1, which is much longer than the optical lifetime of ~2 ms [84]. Könz et al. performed the lifetime measurements of Figure 2.6 in samples with several different concentrations and they indicated that the hyperfine lifetime is not dependent on the concentration.

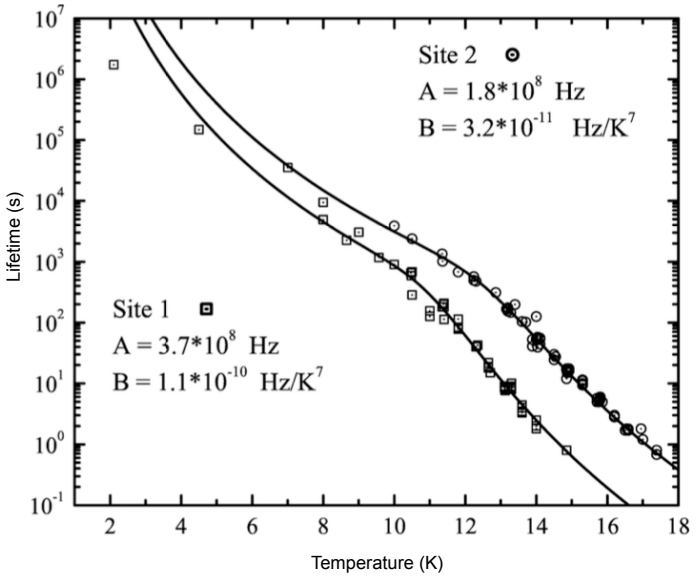

Figure 2.6: Hyperfine lifetime as a function of temperature corresponding to Site 1 and Site 2 in Eu^{3+}:Y_2SiO_5. The solid lines are the theoretical fit according to Equation 2.10. This figure is reproduced with permission from [17]

2.4.3 Homogeneous broadening

While inhomogeneous broadening is the static distribution in the transition frequency of an ensemble, homogeneous broadening is caused by dynamic processes experienced by all the ions in the same way as shown in Figure 2.5. The homogeneous linewidth Γ_h is related

to the coherence time T_2 by

$$\Gamma_h = \frac{1}{\pi T_2} = \frac{1}{2\pi T_1} + \Gamma_\phi \,. \tag{2.11}$$

The first term $\frac{1}{2\pi T_1}$, describes the mechanisms that reduce the lifetime of the excited state of the transition. The second term Γ_ϕ is the contribution of pure dephasing processes, due to interactions that change the transition frequency by shifting the upper and lower energy levels without affecting their lifetimes. The pure dephasing processes can results in both homogeneous broadening and spectral diffusion. Homogeneous broadening is distinguished from spectral diffusion in that the characteristic frequency of the perturbation is large compared to the magnitude of the shifts. As a result, it is not possible to follow the evolution of the transition frequency. For spectral diffusion, the frequency of the perturbation is comparable or smaller than the magnitude of the perturbations, making it possible to follow the evolution of the transition frequency. Importantly, the linewidth observed will now depend on the time-scale of the measurement.

The coherence time is ultimately limited by the lifetime of the excited level, that is $T_2 \leqslant 2T_1$. However, when the system is cooled down to cryogenic temperatures and thus phonon processes are suppressed, there are usually still various Γ_ϕ mechanics preventing the coherence time from reaching the lifetime limit. Generally, Γ_ϕ processes involve dynamic changes in the transition frequency of the rare earth ion due to the fluctuating electric or magnetic field in the surrounding environment. The electric field shifts the frequency via the Stark shift and the magnetic field shifts the frequency via the Zeeman effect.

At cryogenic temperatures, interactions causing dephasing generally include dopant-dopant interactions and dopant-host interactions. Dopant-dopant interactions depend largely on the density of excited ions in the system [67]. The density of excited ions can be reduced by shifting the driving frequency from the centre of the absorption line, decreasing the intensity of the driving field or employing samples with low concentration. In the limit of low excitation density, for the system investigated in this thesis, the remaining dominant Γ_ϕ dephasing source is the dopant-host interactions which is mostly magnetic. This involves the random flips of host spins constantly perturbing the surrounding magnetic field of the dopant ions thereby shifting their transition frequencies. In Eu^{3+}:Y_2SiO_5, there is no first order electronic magnetic moment and the magnetic field sensitivity of the $^7F_0 \rightarrow {}^5D_0$ originates from the magnetic field sensitivity of the hyperfine levels through the quadratic Zeeman and linear Zeeman effect (Equation 2.3). For the hyperfine transitions, only the linear Zeeman effect is important.

Y_2SiO_5, like some other Y^{3+} crystals, such as Y_2O_3, is a good host for coherence experiments because it is a "low noise" host with small magnetic field fluctuations at the dopant ion site. The magnetic perturbation on the dopant ion mainly originates from the 100% abundant of ^{89}Y. ^{89}Y has a nuclear spin of $I = 1/2$ and a small nuclear magnetic moment of $-0.14\mu_N$, where μ_N is the nuclear magneton. The other constituent elements with non-zero magnetic moment are ^{29}Si and ^{17}O, with a nuclear magnetic moments of $-0.56\mu_N$ and $-1.89\mu_N$ respectively. However, both these two isotopes have a very low abundance, 4.7% for ^{29}Si and 0.04% for ^{17}O. To make a comparison, hosts containing Al ion, such as $YAlO_3$ and $Y_3Al_5O_{12}$ (YAG) are not "low noise" hosts, because the 100% ^{27}Al has a much larger magnetic moment of $3.64\mu_N$.

2.4.4 Spectral diffusion

In the previous sections, I talked about the inhomogeneous and homogeneous broadening mechanisms. Inhomogeneous broadening is due to the static variation of the crystalline environment while the homogeneous broadening is due to dynamic fluctuations from the crystalline environment that occur on a time scale much faster than that of a possible measurement. The spectral diffusion, to be discussed in this section, is a dephasing process that occurs at a time scale comparable to that of the measurement. Spectral diffusion can be observed in an experiment measuring the homogeneous linewidth using the two-pulse photon echo for optical transitions and two pulse spin echo for hyperfine transitions (Section 3.1.2). An exponential decay of the echo amplitude with the total evolution time indicates a constant dephasing rate which is the characterisation of homogeneous broadening. The spectral diffusion process, however, can lead to non-exponential decay of the echo. It occurs when the dephasing rate grows with time.

A typical example of a spectral diffusion phenomenon in rare earth doped solids is the frozen core effect [85]. The frozen core effect occurs in many different systems, and here I illustrate it with the Pr^{3+} : LaF_3 system [86]. In Pr^{3+} : LaF_3, the F spins flips randomly, causing dephasing of Pr^{3+} ions. The dominant spin flip process involves spin exchange between two or more F nuclei. As shown in Figure 2.7, in the region far away from the Pr^{3+} ion, all the F nuclei have the same spin frequency and easily exchange energy so the spin flip rate is fast. As these spins are far away from the Pr^{3+} ion, their flipping produces frequency shift on the Pr^{3+} transition which is small compared to the flipping rate. Hence, the effect of the dynamics of the F spins in this region on the Pr^{3+} transition can be treated as the source of homogeneous broadening. In the nearby region, the Pr^{3+} ion produces a local field acting on the F nuclei. Due to the asymmetrical placement and the distance of the nuclei with respect to the Pr^{3+} ion, their spin frequencies are detuned differently. The region in which the frequency of the F spins is detuned is called a frozen core. As a result of the varied spin frequencies, the F nuclei in the core, which produce the largest perturbation on the Pr^{3+} ion, flip at a suppressed rate, which is low compared to the resulting frequency shift induced on the Pr^{3+} transition. Thus, the Pr^{3+} ion does not have a uniform dephasing time. At short time scales, the perturbation is small as it is caused by the bulk F spin flips. As time evolves, the frozen-core F spins gradually flip, which continuously expands the distribution of magnetic perturbation field across the Pr^{3+} ensemble. The resulted increasing dephasing rate is the spectral diffusion, which presents as an non-exponential decay of the echo amplitude in a coherence measurement (Section 3.1.2). Other systems which demonstrated spectral diffusion related to a frozen core effect are Cr^{3+} in ruby [87], Er^{3+} in $YLiF_4$ and LaF_3 [88, 89], Tm^{3+} in LaF_3 and $Y_3Al_5O_2$ (YAG)[90] and Pr^{3+} in Y_2SiO_5 [21].

The frozen core is formed because the dopant ion produces a local field, whose magnitude is proportional to the magnetic moment of the dopant ion. For hyperfine transitions in Eu^{3+}:Y_2SiO_5, the frozen core effect is negligible in zero field as the Eu^{3+} has a relatively small nuclear magnetic moment, which is $\sim$ 700 Hz/G according to the parameters of $\boldsymbol{M}$ tensor in Table 2.5. However, an external applied magnetic field induces a magnetic moment through the quadratic Zeeman tensor (Equation 2.3). The induced moment does not directly change the hyperfine transition frequencies, but it induces a frozen core, the extent of which scales with the applied field. This is detailed in the following section.

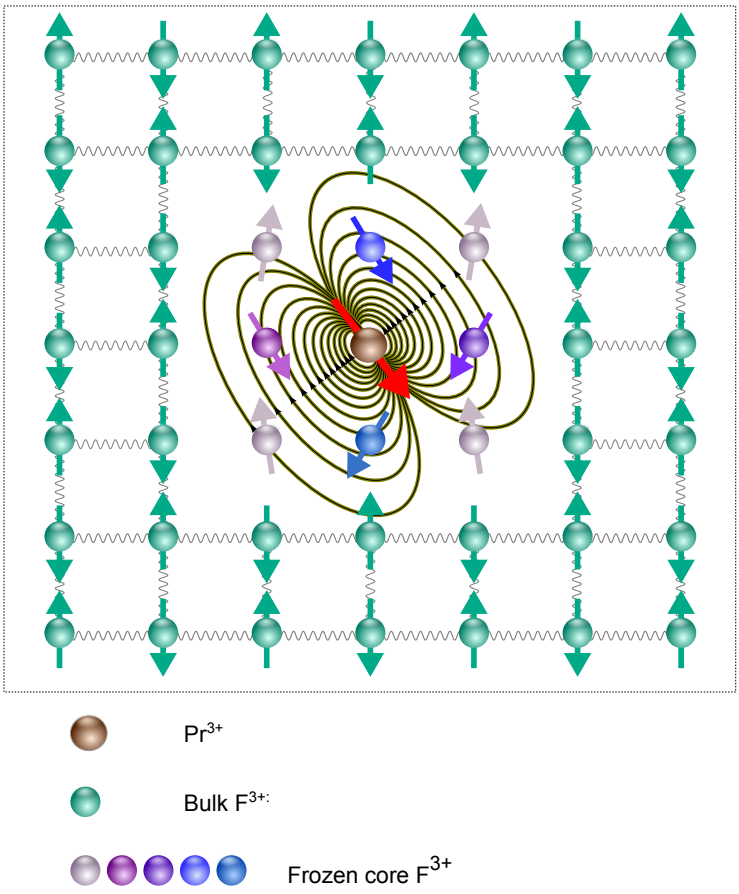

Figure 2.7: Illustration of the frozen core effect for Pr^{3+}:LaF_3. The Pr^{3+} magnetic moment changes the Larmor frequency and quantisation axis of the nearby F nuclei, creating a frozen core of F ions that can not readily exchange spin with the bulk F nuclei.

2.5 Methods for extending hyperfine coherence time of Eu^{3+}:Y_2SiO_5

The focus of this thesis is studying the decoherence mechanism (homogeneous broadening mechanism) of the ground state hyperfine transitions in Eu^{3+}:Y_2SiO_5, with an aim to extend the coherence time. It was demonstrated in the previous sections that, at cryogenic temperatures, the dominant decoherence mechanism for the hyperfine transitions in a sufficiently diluted Eu^{3+}:Y_2SiO_5 sample is random spin flips of the Y^{3+} ions in the host. This section investigates the details of this mechanism and explores methods to extend the coherence times.

2.5.1 ZEFOZ method

The random spin flips of the bulk Y^{3+} ions produce a fluctuating magnetic field on the Eu^{3+} ion, which Zeeman shifts its hyperfine transition frequency and causes decoherence. Assuming that the magnetic field fluctuations occur much faster than the coherence time T_2 of the Eu^{3+} hyperfine transition, T_2 can be estimated according to:

$$\frac{1}{\pi T_2} = \boldsymbol{S_1} \cdot \boldsymbol{\Delta B} + \boldsymbol{\Delta B} \cdot \boldsymbol{S_2} \cdot \boldsymbol{\Delta B}, \tag{2.12}$$

where $\boldsymbol{\Delta B}$, a column vector, is a distribution describing the magnetic field fluctuation while $\boldsymbol{S_1}$ and $\boldsymbol{S_2}$ are the gradient (first order term) and curvature (second order term) respectively of the transition frequency f with respect to magnetic field $\boldsymbol{B} = (B_x, B_y, B_z)'$ [21]. The gradient $\boldsymbol{S_1}$ and curvature $\boldsymbol{S_2}$ are given by

$$\boldsymbol{S_1} = \frac{\partial f}{\partial B_x}\hat{\boldsymbol{i}} + \frac{\partial f}{\partial B_y}\hat{\boldsymbol{j}} + \frac{\partial f}{\partial B_z}\hat{\boldsymbol{k}}, \tag{2.13}$$

and

$$\boldsymbol{S_2} = \begin{bmatrix} \frac{\partial^2 f}{\partial B_x \partial B_x} & \frac{\partial^2 f}{\partial B_x \partial B_y} & \frac{\partial^2 f}{\partial B_x \partial B_z} \\ \frac{\partial^2 f}{\partial B_y \partial B_x} & \frac{\partial^2 f}{\partial B_y \partial B_y} & \frac{\partial^2 f}{\partial B_y \partial B_z} \\ \frac{\partial^2 f}{\partial B_z \partial B_x} & \frac{\partial^2 f}{\partial B_z \partial B_y} & \frac{\partial^2 f}{\partial B_z \partial B_z} \end{bmatrix}. \tag{2.14}$$

The values of $\boldsymbol{S_1}$ and $\boldsymbol{S_2}$ can be worked out using the reduced spin Hamiltonian of Equation 2.4 and the parameters listed in Table 2.5. The unit vectors $\hat{\boldsymbol{i}}$, $\hat{\boldsymbol{j}}$ and $\hat{\boldsymbol{k}}$ are for the coordination system used to define the applied magnetic field $\boldsymbol{B}$. With this Hamiltonian and the parameters, the electronic ground ($^7F_0$) state hyperfine energy levels of $^{151}Eu^{3+}$ ion occupying a Site 1 Y^{3+} position in Y_2SiO_5 [77] were also calculated and are shown in Figure 2.8.

In the presence of an external magnetic field, as shown in Figure 2.8, level anti-crossings occur when the linear Zeeman splitting approaches the magnitude of the quadrupole splitting. In this regime, $\boldsymbol{S_1}$ and $\boldsymbol{S_2}$ are strongly dependent on the applied field magnitude and direction. The sensitivity of the hyperfine transition to $\boldsymbol{\Delta B}$ can be significantly reduced by applying a particular field so that the transition frequency is at a critical point such that the first order field sensitivity vanishes, namely

$$\left(\frac{\partial f}{\partial B_x}\right)^2 + \left(\frac{\partial f}{\partial B_y}\right)^2 + \left(\frac{\partial f}{\partial B_z}\right)^2 = 0. \tag{2.15}$$

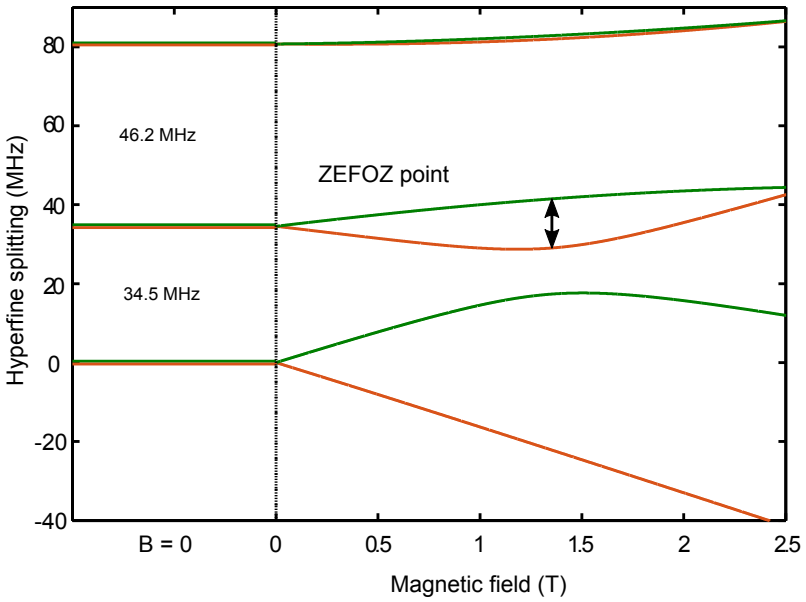

Figure 2.8: Illustration of a ZEFOZ transition. The graph shows the calculated hyperfine ground state energy levels of $^{151}Eu^{3+}$:Y_2SiO_5 as a magnetic field is increased from zero in a ZEFOZ direction. The calculation is performed using the reduced spin Hamiltonian in Reference [22]. At the field magnitude as marked, the transition experiences a critical point, at which the transition is no longer sensitive to small field perturbations in any directions to first order.

This zero first-order Zeeman (ZEFOZ) method is analogous to a clock transition in atomic spectroscopy [91]. At the ZEFOZ field, T_2 can be extended because the transition frequency is insensitive to first order Zeeman shifts in all three directions. Only the second-order Zeeman coefficient $\boldsymbol{S_2}$, that is the curvature at the critical point, couples the transition to magnetic fluctuations. This method was first implemented in Pr^{3+}:Y_2SiO_5, which resulted in an extension of the hyperfine coherence time of Pr^{3+} from 500 µs to 1.4 s [21, 22]. The latter corresponds to a decoherence rate ($1/T_2$) of 0.7 s^{-1}.

The studies of hyperfine decoherence in Pr^{3+}:Y_2SiO_5 indicate that the achieved storage times are reaching the limit imposed by $\boldsymbol{S_2}$ [10, 12]. Although a significant increase in current coherence times is unlikely in Pr^{3+}:Y_2SiO_5, it was predicted by Longdell et al. that coherence times much longer than 1.4 s should be achievable in Eu^{3+}:Y_2SiO_5 using the ZEFOZ technique [22]. This is because the critical points in Eu^{3+}:Y_2SiO_5 have much smaller second-order Zeeman coefficient as shown in Figure 2.9. This assertion is based on the assumption that the magnetic field fluctuations causing dephasing should have the same origin in both Pr^{3+}:Y_2SiO_5 and Eu^{3+}:Y_2SiO_5 which is reasonable because the fluctuation arises from the host rather than the dopant.

For both Pr^{3+}:Y_2SiO_5 and Eu^{3+}:Y_2SiO_5, there are a number of critical points with different magnetic fields and curvature values as shown in Figure 2.9. The circled point labelled as 'A' is the ZEFOZ transition used in Pr^{3+}:Y_2SiO_5 for which the coherence time was extended from 550 us to 1.4 s. This critical point occurs at a field of 780 G and has a curvature value of 60 Hz/G^2. The point labelled as 'B' is the critical point for Eu^{3+}:Y_2SiO_5 to be investigated in this thesis, which has a field magnitude of around 1.3 T and a curvature of 0.217 Hz/G^2. This curvature value is 276 times smaller than the 'A' transition in Pr^{3+}:Y_2SiO_5, implying possible coherence times of ~400 s according to

Equation 2.12. At higher fields, critical points with even lower curvature are available in Eu^{3+}:Y_2SiO_5, such as the one marked with 'C' in Figure 2.9, occuring at a field magnitude of 4.6 T and with a curvature of 0.154 Hz/G^2. At this point, the coherence time is expected to be even longer.

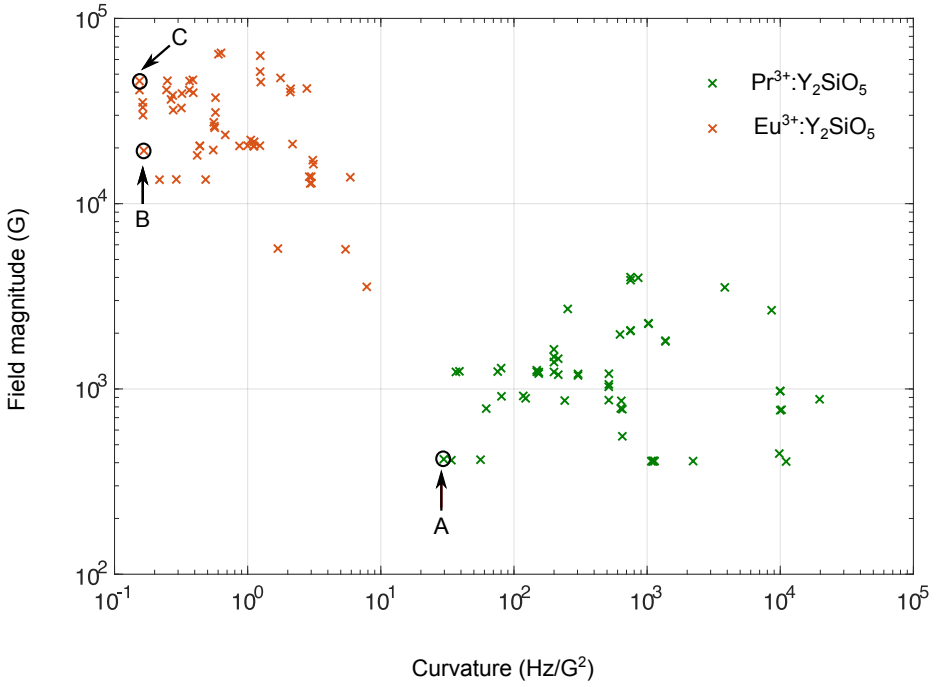

Figure 2.9: Comparison of ZEFOZ values in two different systems, Eu^{3+}:Y_2SiO_5 and Pr^{3+}:Y_2SiO_5, performed by Londell et al. [22]. Each point in the diagram represents a critical point identified in the material. The curvature tensor $\boldsymbol{S_2}$, as shown in Equation 2.14, is a tensor valued quantity but is reduced here to a single number by taking the largest of the absolute values of the eigenvalues. The magnitude of the ZEFOZ field is plotted against the second order Zeeman dependence. The critical point marked with 'A' was the one investigated in [21, 22], with 'B' the one to be studied in this thesis and with 'C' the critical point in Eu^{3+}:Y_2SiO_5 having the smallest curvature.

2.5.2 Calculation of the field perturbation

The distribution describing the magnetic field fluctuation $\boldsymbol{\Delta B}$ can be estimated using the Monte-Carlo simulation procedure described in [92]. The calculation is performed by considering one Eu^{3+} ion occupying a Site 1 Y^{3+} position in Y_2SiO_5 [77] being surrounded by a host which does not contain any other Eu ion. The bulk Y spins are randomly orientated then the field on the Eu ion from the magnetic dipole of each Y spin is summed:

$$\boldsymbol{\Delta B} = \frac{\mu_0}{4\pi} \sum_{i=1}^{n} \left(\frac{3(\boldsymbol{m_Y} \cdot \boldsymbol{r}_i)\boldsymbol{r}_i}{|\boldsymbol{r}_i|^5} - \frac{\boldsymbol{m_Y}}{|\boldsymbol{r}_i|^3} \right), \tag{2.16}$$

where $\boldsymbol{m_Y}$ is the nuclear magnetic dipole moment of Y^{3+} ions, given by

$$\boldsymbol{m_Y} = \gamma h \boldsymbol{I}. \tag{2.17}$$

The constants in these two equationss are listed as follows:

- μ_0 is the vacuum permeability, $\mu_0 = 4\pi \times 10^{-7}$ T·m/A,
- $\boldsymbol{r_i}$ is the displacement of the i-th Y^{3+} ion relative to the Eu ion,
- γ is the gyromagnetic ratio of Y^{3+} ions, $\gamma = 2.09 \times 10^6$ Hz/T,
- h is Planck's constant, $h = 6.626 \times 10^{-34}$ J·s,
- $\boldsymbol{I}$ is the nuclear spin state vector of Y ions, $|I| = 1/2$.

The Y positions were calculated by Ahlefeldt [93] using the Y_2SiO_5 crystal structure listed in Table 2.2, which was provided by Scientific Materials Corp. (Bozeman, Montana). The nearest 2000 ions were included in the Monte-Carlo calculation and it was found that only the nearest 60 ions make a significant contribution to the field. After 5×10^5 iterations of randomisation of the spin states, a histogram of magnetic field values at the Eu site was produced as shown in Figure 2.10. The full width at half maximum (FWHM) linewidth of the field perturbation $\boldsymbol{\Delta B}$ was calculated to be 8.0 μT.

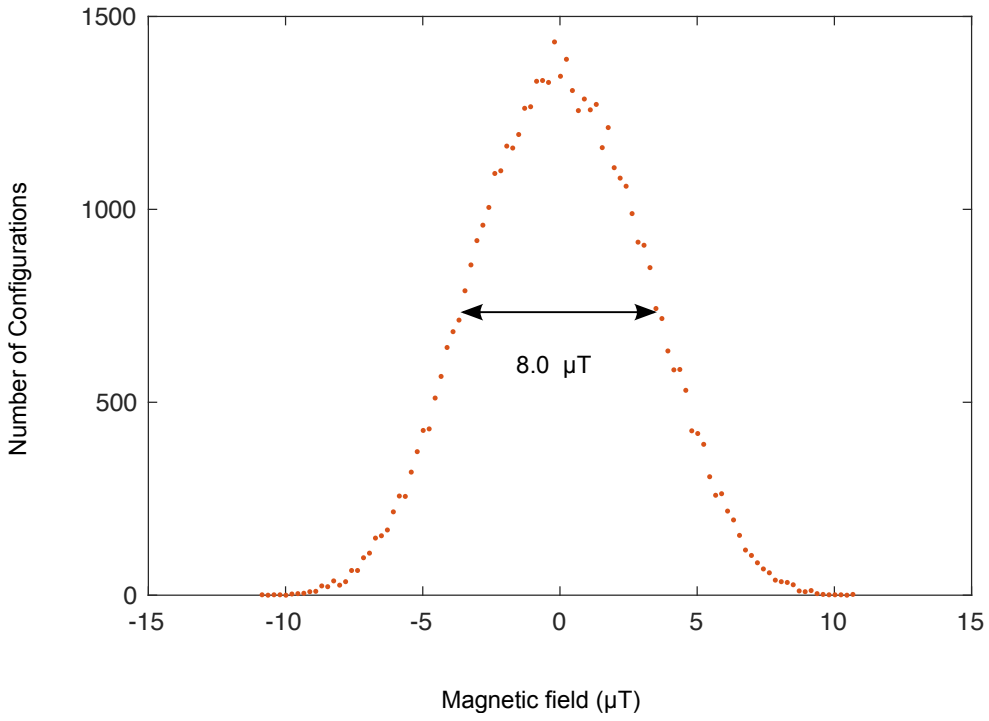

Figure 2.10: Magnetic field distribution along x axis at the Eu site due to randomly orientated Y spins in Y_2SiO_5 host. The distributions along y and z axes are identical, which also present a field distribution (FWHM) of 8.0 μT.

With this field perturbation, according to Equation 2.12, for a perfect field alignment at the critical point ($\boldsymbol{S_1} = 0$) in Pr^{3+}:Y_2SiO_5, marked 'A' in Figure 2.9, the coherence time

is estimated to be 0.8 s, which is slightly under the experimentally measured value of 1.4 s [92]. This is most probably because, besides the ZEFOZ effect, there was a frozen core of Y^{3+} spins produced by the Pr^{3+} magnetic moment, which also contributed to extend the coherence time to 1.4 s in Pr^{3+}:Y_2SiO_5. For Eu^{3+}:Y_2SiO_5, if there is no frozen core, using Equation 2.12, an aligned critical point, marked 'A' in Figure 2.9, is expected to have a coherence time of 229 s. However, the applied ZEFOZ field would induce a frozen core on Eu^{3+}, which means the coherence time might be expected to be longer than 229 s. The frozen core effect in Eu^{3+}:Y_2SiO_5 is to be discussed in the following section.

2.5.3 Frozen core effect

The Eu^{3+} hyperfine ground state has a nuclear magnetic moment comparable to that of a Y^{3+} ion, thus the frozen core effect is expected to be very small at zero field. The Y^{3+} ions around the Eu ions easily exchange spins with each other and flip fast, which limits the Eu hyperfine coherence time to the order of 10 ms [67]. However, in the presence of an external magnetic field, due to the quadratic Zeeman interaction, a magnetic moment is induced on the Eu ion. The induced magnetic moment of Eu can be written:

$$\boldsymbol{m_{Eu}} = \boldsymbol{Z} \cdot \boldsymbol{B}, \tag{2.18}$$

where $\boldsymbol{Z}$ is the quadratic Zeeman tensor as shown in Equation 2.3 and $\boldsymbol{B}$ the applied magnetic field. The induced moment is linearly dependent on the magnetic field, with a gradient given by the quadratic Zeeman tensor. I have measured the quadratic Zeeman coefficient along the three principal axes of polarisation for the crystal to be $Z(D_1, D_2, C_2)$ = (-0.56, -0.53, -1.58) Hz/G^2 (Appendix A). Then the quadratic Zeeman tensor can be worked out using the parameters in table 2.5 because the quadratic Zeeman tensor and the Zeeman tensor have the same principal axes ($\boldsymbol{R_Z} = \boldsymbol{R_M}$, Section 2.3.2).

As the magnetic field is increased, the induced magnetic moment on Eu^{3+} detunes the nearby Y^{3+} ions from the bulk and produces a frozen core. It then becomes difficult for the Y^{3+} ions around the Eu ion to exchange spins with each other and therefore they flip at a suppressed rate. This results in a decreased value of the field fluctuation $\boldsymbol{\Delta B}$ acting on the Eu ion over short time intervals, thereby extending the coherence time of its hyperfine transitions.

The size of the frozen core can be estimated by determining the distance by which the Eu-Y interaction exceeds the Y-Y interaction. Similar to the calculation for $\boldsymbol{\Delta B}$ described in Section 2.5.2, the detuning frequencies and the frozen core size can be calculated using the Hamiltonian [1]:

$$H_{DD} = \frac{\mu_0}{4\pi|\boldsymbol{r}|^3}(\boldsymbol{m_{Eu}} \cdot \boldsymbol{m_Y} - \frac{3(\boldsymbol{m_{Eu}} \cdot \boldsymbol{r})(\boldsymbol{m_Y} \cdot \boldsymbol{r})}{|\boldsymbol{r}|^2}), \tag{2.19}$$

where the magnetic moment for Y^{3+} is defined in Equation 2.17. For Eu^{3+}, at the moment, I neglect the non-induced component (the nuclear magnetic moment), which is dependent on the hyperfine states, and only consider the induced moment by the magnetic field on the electronic states. This is because, when the applied field is higher than 0.1 T, the induced moment is much larger than the nuclear magnetic moment. With the field ramping up in the direction of the critical point field marked 'B' in Figure 2.9, the result of

[1] For the frozen core size calculation, as we are only interested in the scale of the dipole-dipole interaction strength, the angle-dependent term of the following Hamiltonian is not included.

the calculation is shown in Figure 2.11. The detuning on each of the Y^{3+} ion in the frozen core is different depending on the Eu-Y displacement, and it is shown in Figure 2.11(a) that the second-nearest Y^{3+} ion has its frequency detuned the most. For each ion, the field detuning increases linearly with the magnetic field. In Figure 2.11(b), it is shown that the number of the ions included in the frozen core also increase linearly with the magnitude of the field. At a field of 1 T, more than 200 Y^{3+} ions are included in the frozen core, and the frequency of one of the nearest Y^{3+} ion is detuned more than 1000 Hz, which is much larger than the linewidth of the bulk Y^{3+} ions' spin transition. Given by field distribution $|\boldsymbol{\Delta B}| = 8.0\,\mu$T, the bulk-$Y^{3+}$ linewidth can be calculated using $\Delta\nu = \gamma|\boldsymbol{\Delta B}| = 16$ Hz. It is reasonable to conclude that, at a high magnetic field, the flipping of the nearest Y^{3+} spins is largely suppressed, thus, the field perturbation on Eu^{3+} at short time intervals is significantly decreased.

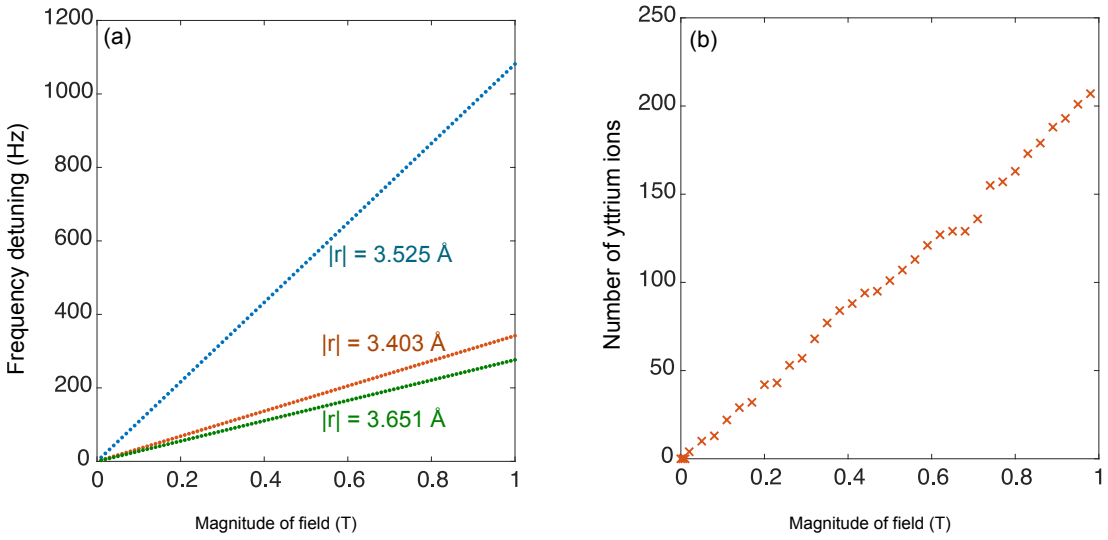

Figure 2.11: This figure shows the increase of the detuning frequencies of the nearest three Y^{3+} ions in (a) and the number of Y^{3+} ions included in the Y^{3+} frozen core in (b) as the magnetic field magnitude is ramped up in the direction of the critical point field marked 'B' in Figure 2.9.

2.5.4 The effects of driving Eu^{3+} transitions on the Y^{3+} bath

In the previous section, the discussion focused on the impact of the Y^{3+} transitions on a Eu^{3+} transition. In fact, driving an Eu^{3+} transition can also influence the dynamics of the Y^{3+} spins. This means that driving a Eu^{3+} transition will disturb the environment which will have a back action on Eu^{3+}, inducing excess dephasing. The reason is that changing the state of the Eu^{3+} ion will change the magnetic environment seen by the Y^{3+} spins. This slightly changes the quantisation axis of the Y^{3+} spins, causing a small probability of Y^{3+} spin flips. A small change in the quantisation axis can also induce Y-Y spin flip-flop process, which conserve energy, resulting in near degenerate initial and final magnetic field configurations as investigated by Pryde in Pr^{3+}:LaF_3 [94].

The impact of driving an Eu^{3+} transition on the Y^{3+} bath originates from the change of the magnetic moment of Eu^{3+}, which changes the magnetic environment at Y^{3+} sites. The magnetic fields acting on a Y^{3+} due to the magnetic moment of the ground and

excited state Eu^{3+} can be written as:

$$\boldsymbol{B}_g = \frac{\mu_0}{4\pi}\left(\frac{3(\boldsymbol{m_g}\cdot\boldsymbol{r})\boldsymbol{r}}{|\boldsymbol{r}|^5} - \frac{\boldsymbol{m_g}}{|\boldsymbol{r}|^3}\right), \tag{2.20}$$

$$\boldsymbol{B}_e = \frac{\mu_0}{4\pi}\left(\frac{3(\boldsymbol{m_e}\cdot\boldsymbol{r})\boldsymbol{r}}{|\boldsymbol{r}|^5} - \frac{\boldsymbol{m_e}}{|\boldsymbol{r}|^3}\right), \tag{2.21}$$

where $\mu_0 = 4\pi \times 10^{-7}$ T·m/A is the magnetic constant, $\boldsymbol{r}$ is the displacement of the Y^{3+} ion relative to the Eu ion. $\boldsymbol{m_g}$ and $\boldsymbol{m_e}$ are the magnetic moments of the Eu^{3+} at ground state $|g\rangle$ and excited state $|e\rangle$ respectively. The change of the magnetic field on the Y^{3+} by driving the Eu^{3+} transition is then written:

$$\boldsymbol{\Delta B}_{Eu} = \frac{\mu_0}{4\pi}\left(\frac{3(\boldsymbol{\Delta m}\cdot\boldsymbol{r})\boldsymbol{r}}{|\boldsymbol{r}|^5} - \frac{\boldsymbol{\Delta m}}{|\boldsymbol{r}|^3}\right), \tag{2.22}$$

where $\boldsymbol{\Delta m} = \boldsymbol{m_e} - \boldsymbol{m_g}$ is the difference in the magnetic moment of Eu^{3+} between the ground and excited hyperfine states. To work out $\boldsymbol{\Delta m}$, we start with the Hamiltonian for the hyperfine energy levels of Equation 2.3:

$$H = (\boldsymbol{B}\cdot\boldsymbol{Z}\cdot\boldsymbol{B})\hat{\boldsymbol{E}} + \boldsymbol{B}\cdot\boldsymbol{M}\cdot\hat{\boldsymbol{I}} + \hat{\boldsymbol{I}}\cdot\boldsymbol{Q}\cdot\hat{\boldsymbol{I}}.$$

If the applied field is $\boldsymbol{B} = B_x\hat{\boldsymbol{i}} + B_y\hat{\boldsymbol{j}} + Bz\hat{\boldsymbol{k}}$, then the magnetic moment $\boldsymbol{m_g}$ and $\boldsymbol{m_e}$ can be written:

$$\boldsymbol{m_g} = \left\langle g\middle|\frac{\partial H}{\partial B_x}\middle|g\right\rangle\hat{\boldsymbol{i}} + \left\langle g\middle|\frac{\partial H}{\partial B_y}\middle|g\right\rangle\hat{\boldsymbol{j}} + \left\langle g\middle|\frac{\partial H}{\partial B_z}\middle|g\right\rangle\hat{\boldsymbol{k}}, \tag{2.23}$$

$$\boldsymbol{m_e} = \left\langle e\middle|\frac{\partial H}{\partial B_x}\middle|e\right\rangle\hat{\boldsymbol{i}} + \left\langle e\middle|\frac{\partial H}{\partial B_y}\middle|e\right\rangle\hat{\boldsymbol{j}} + \left\langle e\middle|\frac{\partial H}{\partial B_z}\middle|e\right\rangle\hat{\boldsymbol{k}}. \tag{2.24}$$

The values for $\boldsymbol{m_g}$ and $\boldsymbol{m_e}$ can be calculated using the $\boldsymbol{M}$-tensor and $\boldsymbol{Q}$-tensor parameters in Table 2.5 as well as the $\boldsymbol{Z}$-tensor parameters presented in Section 2.5.3. With a field increased in the direction of the critical field marked 'B' in Figure 2.9, the absolute values of $\boldsymbol{m_g}$, $\boldsymbol{m_e}$ and $\boldsymbol{\Delta m}$ are shown in Figure 2.12.

The first term of Equation 2.3, which determines the induced moment, is independent of the spin state $\boldsymbol{I}$. Thus the induced moment has the same value for both hyperfine ground and excited levels. However, the non-induced term of the moment, the nuclear magnetic moment term, given by the second and third terms of Equation 2.3, causes the mixing between the hyperfine levels. As a result, the total moments for the two levels depend on the applied field in different ways as shown in Figure 2.12(a).

It was discussed in Section 2.5.1 that there are critical points of the transition where $\left(\frac{\partial f}{\partial B_x}\right)^2 + \left(\frac{\partial f}{\partial B_y}\right)^2 + \left(\frac{\partial f}{\partial B_z}\right)^2 = 0$ (Equation 2.15), which is equivalent to $\boldsymbol{m_e} = \boldsymbol{m_g}$, namely $\boldsymbol{\Delta m} = 0$ (Footnote [2]). It means, according to Equation 2.22, driving a Eu^{3+} transition at

[2] The field perturbation $\boldsymbol{\delta B}$ from the Y^{3+} bath shifts the hyperfine ground and excited energy levels of Eu^{3+} by:

$$\delta E_g = h\boldsymbol{m_g}\cdot\boldsymbol{\delta B}, \tag{2.25}$$

$$\delta E_e = h\boldsymbol{m_e}\cdot\boldsymbol{\delta B}, \tag{2.26}$$

where h is the Planck constant. This leads to a frequency shift of the hyperfine transition :

$$\delta f = \frac{1}{h}(E_e - E_g) = \boldsymbol{\Delta m}\cdot\boldsymbol{\delta B}. \tag{2.27}$$

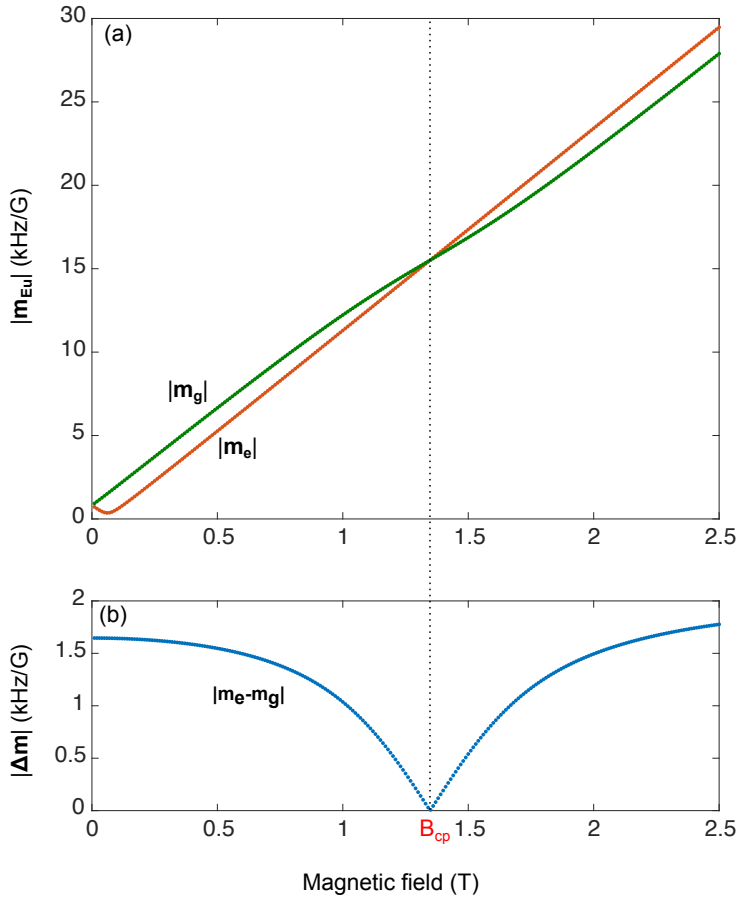

Figure 2.12: (a) The absolute value of the ground and excited hyperfine state magnetic moment of Eu, plotted against the magnetic field, which is increased along a critical field direction. (b) The absolute value of the difference in the magnetic moment between the ground and excited hyperfine states of Eu^{3+}, which is plotted against the same field values as (a).

a critical point does not change the magnetic field, thus does not disturb the Y^{3+} system.

When the field is detuned from the critical moment, as shown in Figure 2.12, the moment for Eu^{3+} is different for the hyperfine ground and excited states. Hence, driving an Eu^{3+} transition results in a change in the magnetic moment of Eu^{3+}, which disturbs the Y^{3+} system. This disturbance in the environmental Y^{3+} system will have a back action on Eu^{3+}, again through $\boldsymbol{\Delta m}$, inducing excess dephasing. This is particular important for techniques that involves driving a Eu^{3+} transition with many pulses, such as with dynamic decoherence control (DDC, detailed in Section 3.1.4), which is designed to reduce dephasing. The interactions discussed above means that DDC, when applied at a magnetic field where $\boldsymbol{\Delta m}$ is non-zero, will introduce an extra source of depahsing, thereby reducing its effectiveness.

From the above discussion, driving a Eu^{3+} transition at a critical point has two benefits. First, it largely suppress the sensitivity of the Eu^{3+} transition to the magnetic field perturbation arising from the random spin flips in the Y^{3+} bath, which extend the coherence time. Further, at the critical point where $\boldsymbol{\Delta m} = 0$, driving a Eu^{3+} transition does not disturb the Y^{3+} system. The latter allows the possibility to use a large number of DDC pulses to the Eu^{3+} system to fight decoherence, without concerns about accumulation of errors induced by this dynamic reconfiguration of the environment. The combination of the ZEFOZ technique and DDC was used in Pr^{3+}:Y_2SiO_5 and extended the hyperfine coherence time from 1.4 s to 30 s [10]. Recently, the combination of ZEFOZ and DDC was applied to the storage of images using electromagnetically induced transparency, allowing storage times greater than 40 s [12]. The 40 s is 28 times longer than 1.4 s. Assuming that the DDC has the same effectiveness in Eu^{3+}:Y_2SiO_5 as that in Pr^{3+}:Y_2SiO_5, the coherence time in Eu^{3+}:Y_2SiO_5 is expected to be a few hours (229 s$\times$28 = 6412 s).

2.6 Summary

Rare-earth doped solids are promising candidates for quantum memory applications due to their good coherence properties. The reason for these good coherence properties is because their transitions within the $4f^N$ configuration have weak coupling to the magnetic and crystal field of the hosts. Among the many rare-earth systems, the hyperfine transitions in Eu^{3+}:Y_2SiO_5 are particular attractive, given the extremely long lifetime of up to 23 days [17].

At cryogenic temperatures, the dominant decoherence mechanism for Eu^{3+} hyperfine transitions in Y_2SiO_5 is the magnetic field fluctuation due to the random Y^{3+} spin flips. An extension of the coherence time can be achieved using the ZEFOZ method. This works by applying a special magnetic field, at which the hyperfine ground and excited levels experience the same magnetic moment, such that the transition's sensitivity to the field perturbation is largely decreased. Such a field is called a critical point.

Applying such an external magnetic field also results in an extra extension of the coherence time due to the creation of a frozen core of Y^{3+} ions. This occurs because the applied field induces a magnetic moment on Eu^{3+}, which detunes the spin frequency of the nearby Y^{3+} ions. The frozen core effect largely suppresses the spin flips of these ions, thereby reducing the field perturbation acting on the Eu^{3+} ion, and thus extend the coherence time.

Hours-long hyperfine coherence time are expected in Eu^{3+}:Y_2SiO_5 through the com-

bination of the ZEFOZ effect and the frozen core. The possible coherence time is different for each of the many critical points in Eu^{3+}:Y_2SiO_5 with different curvatures and magnetic field. It is better to choose those with smaller curvature and larger field magnitude, because smaller curvature means lower field sensitivity at the ZEFOZ transition while a larger field magnitude means a larger volume of the frozen core, namely a smaller field perturbation.

There is additional benefit of using the ZEFOZ transitions when techniques involving driving the Eu^{3+} transition with large number of pulses, such as the dynamic decoherence control, are applied to the system to fight decoherence. This is because driving an Eu^{3+} transition at critical point will not change the Eu^{3+} magnetic moment, thus it does not disturb the Y^{3+} bath. This allows the application of many pulses on Eu without inducing extra dephasing due to reconfiguration of the environment.

Chapter 3

Techniques for coherence measurements

An ensemble system of rare earth ions can never be made completely isolated from the environment and the interaction between the system and the surrounding environment results in broadening of a transition. This broadening can be classified as inhomogeneous broadening, homogeneous broadening and spectral diffusion based on the time scale it occurs on. If the transition is not lifetime limited, the broadening is mainly due to a frequency shift of the transition caused by system-environment interactions. Inhomogeneous broadening corresponds to a static frequency shift while homogeneous broadening and spectral diffusion correspond to a dynamic frequency shift. In Section 2.4, the mechanisms contributing to these different broadening types were analysed in detail. In this chapter, I review the techniques to observe the effect of these broadening mechanisms have on the ensemble coherence.

These broadening effects can be measured by observing the behaviour of the system driven by resonant radiation. The system investigated in this thesis is the hyperfine transitions in Eu^{3+}:Y_2SiO_5, which occur at radio frequencies (RF). If a resonant pulse is applied to the system, coherence emission dephasing at a rate given by the inhomogeneous broadening is obtained. This inhomogeneous contribution can be removed by using the two pulse spin echo technique, which allows a measurement of the homogeneous broadening. Dynamic dephasing sources, either homogeneous broadening or the spectral diffusion, causes the size of the echo to decay as a function of the total evolution time. If the dephasing is due to homogeneous broadening, then the dynamic perturbation from the environment is fast and involves a small frequency shift. This results in an exponential echo decay which can be characterised using a constant coherence time T_2. Spectral diffusion, however, involves slow and large frequency shifts. It corresponds to a non-exponential decay of the two pulse spin echo signal and accordingly can not described by a uniform T_2.

While the two pulse spin echo removes the decoherence due to static dephasing, it does not remove the decoherence due to dynamic dephasing. A strategy of fighting decoherence is known as dynamic decoherence control (DDC). It works by applying a large number of resonant pulses to refocus the dephased ensemble repeatedly and extend the coherence time.

This chapter begins with an introduction of the Bloch sphere representation of a two-level system, with which I then illustrate the two pulse spin echo technique. After that, I present an analysis of the two echo decay shapes as given above, which is followed by an introduction to DDC. I then talk about two methods for measuring hyperfine coherence time via the optical transition. These two methods are spectral holeburning and Raman

heterodyne detected coherence transients.

3.1 Decoherence of two-level spin ensemble systems

The focus of this thesis is on the hyperfine decoherence mechanisms in Eu^{3+}:Y_2SiO_5, which involves the interactions of a two-level ensemble system with radiation. A typical example of such interactions occurs between a nuclear spin-half system with a RF field in the field of nuclear magnetic resonance (NMR) spectroscopy. The interactions between a spin-half system with a driving RF field are usually illustrated using a coordination frame rotating about the z axis at the rate of the resonant frequency. Such a rotation frame is represented with a Bloch sphere, which can be used to describe any closed two level systems including a subspace of the spin 5/2 system discussed in this thesis. The Bloch sphere provides an excellent tool to visualise the evolution of the magnetic moment vectors of a two-level ensemble system interacting with a resonant driving field.

In this section, I first introduce the Bloch sphere representation of quantum states. Using the Bloch sphere, I then illustrate the concepts of free induction decay (FID) and two pulse spin echo. After that, I present an analysis of the spin echo decay. Finally, I introduce the concept of dynamic decoherence control (DDC).

3.1.1 The Boch sphere representation of quantum states

The Bloch sphere provides a graphical representation of the wavefunction of a two level system as a vector in a unit sphere. An arbitrary vector $\mathbf{r}$ in a unit sphere, as shown in Figure 3.1, has the form:

$$\mathbf{r} = \cos\phi\sin\theta\hat{\mathbf{x}} + \sin\phi\sin\theta\hat{\mathbf{y}} + \cos\theta\hat{\mathbf{z}}. \tag{3.1}$$

A general state of two-level system is described by $|\psi\rangle = c_1|1\rangle + c_2|2\rangle$ with $|c_1|^2 + |c_2|^2 = 1$. This equation is mapped to the unit sphere by rewriting it as:

$$|\psi\rangle = \sin\frac{\theta}{2}|1\rangle + e^{i\phi}\cos\frac{\theta}{2}|2\rangle, \tag{3.2}$$

where the angles θ and ϕ in this equation are identical to those in Equation 3.1. In the Bloch sphere, the ground state $|1\rangle$ and the excited state $|2\rangle$ correspond to the south pole and the north pole respectively. Other points on the surface of the sphere represent superpositions of states $|1\rangle$ and $|2\rangle$. In particular, the states in the xy plane are 50:50 superposition states, with:

$$\begin{aligned}\hat{\mathbf{x}} &= \frac{1}{\sqrt{2}}(\,|1\rangle + |2\rangle\,)\\ \hat{\mathbf{y}} &= \frac{1}{\sqrt{2}}(\,|1\rangle + i|2\rangle\,)\end{aligned} \tag{3.3}$$

3.1.2 Two pulse spin echo

A two-level ensemble system in the ground $|1\rangle$ state has the ensemble vector along the $-z$ axis on the Bloch sphere. Typically the transition frequency of an ensemble system

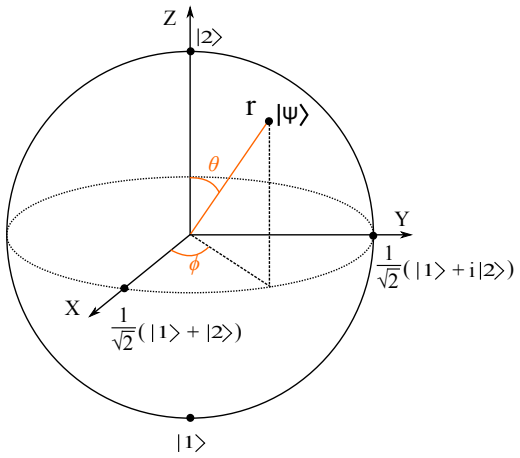

Figure 3.1: Bloch sphere representation of the state of a two level system.

is inhomogeneous broadened and the ensemble can be broken into different subgroups of ions with each subgroup having a different resonant frequency. Then the ensemble Bloch vector can be described as:

$$\boldsymbol{M_0} = \sum_j \boldsymbol{M_{0,j}}, \tag{3.4}$$

where $\boldsymbol{M_{0,j}}$ is the Bloch vector for the j-th subgroup of ions.

In a two-pulse echo sequence, as shown in Figure 3.2, a resonant $\pi/2$ pulse along the x axis is applied to the system, which rotates the ensemble Bloch vector from $-z$ axis to the $+y$ axis. The rotation axis is decided by the phase of the pulse. The Bloch vectors of the individual spins then precess around the z-axis in the xy-plane. In an inhomogeneously broadened ensemble, the spin subgroups precess at different rates. In the rotating frame of the Bloch sphere, each spin vector rotates at a rate equal to its detuning from the frequency of the driving field, resulting in a total Bloch vector (total moment) at a time t after the end of the pulse [85]:

$$\boldsymbol{M_{x+iy}}(t) = \sum_j \boldsymbol{M_{0,j}} \exp(i\Delta\omega_j t), \tag{3.5}$$

where the detuning $\Delta\omega_j$ is described by

$$\Delta\omega_j = \omega_j - \omega_0. \tag{3.6}$$

In this equation, ω_o is the frequency of the driving field while ω_j is the transition frequency for the j-th subgroup of ions. It is clear that $\boldsymbol{M_{x+iy}}$ is the Fourier transform of the spin moment distribution $\boldsymbol{M_{0,j}}$, which defines the inhomogneous line shape. In the lab frame, $\boldsymbol{M_{x+iy}}$ precesses at the resonant frequency near ω_0 and generates a RF signal which is known as the Free Induction Decay (FID). If the spectral line shape of the inhomogeneously broadened transitions is Lorentzian, then Equation 3.5 corresponds to an exponential FID decay, with the decay rate proportional to the inverse of the inhomogeneous width of the

transition, given by the following relation:

$$\Gamma_{inh} = \frac{2\pi}{T_2^*}, \tag{3.7}$$

where Γ_{inh} is the inhomogeneous linewidth of the transition and T_2^* is the time taken for $\boldsymbol{M_{x+iy}}$ to reach $1/e$ of the value when the driving pulse is ended.

The above FID model is based on the assumption that the lifetime T_1 and the coherence time T_2 is much longer than T_2^*. In addition, though both the inhomogeneous broadening and the dynamic effect dephase the FID signal, the inhomogeneous broadening is large and dominates. Hence, the decay given by the constant T_2^* is unrelated to true decoherence processes which act to dephase an individual spin of the ensemble.

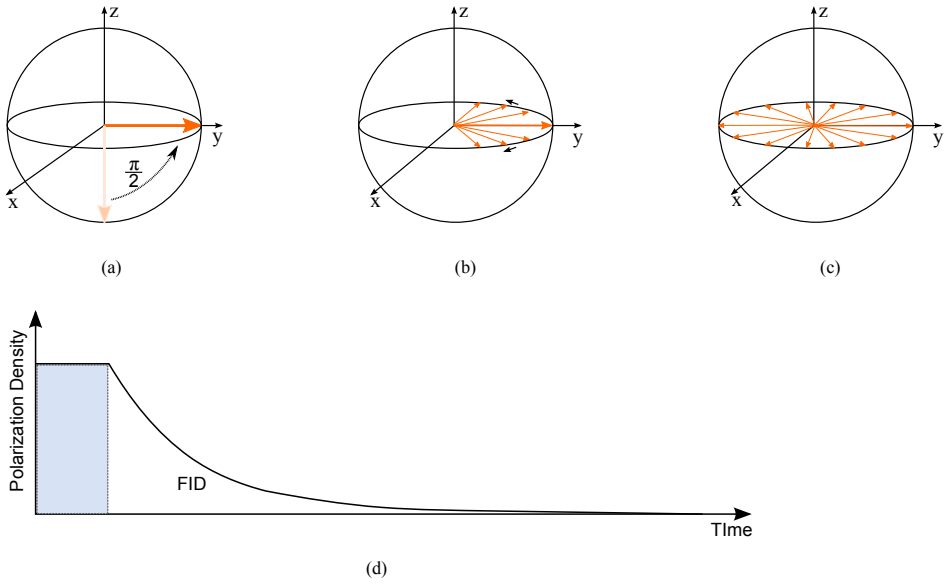

Figure 3.2: Bloch sphere representation of an ensemble placed in a 50-50 superposition state undergoing a Free Induction Decay (FID). (a) The ensemble is driven into a 50-50 superposition state by a $\frac{\pi}{2}$-pulse. (b) The Bloch vectors of individual subgroups start to precess around the Bloch sphere with a rate and direction decided by their detunings. This causes the ensemble Bloch vector (projection on the y axis) to decay exponentially, radiating the FID signal. (c)The radiation ceases when the ensemble polarisation dephases completely. (d) The FID signal.

Spin echoes on hyperfine transitions were first demonstrated by E. L. Hahn in 1950[95], and provide an effective way to completely remove the effect of inhomogeneous broadening on a transition and measure the true coherence properties. The spin echo technique allows to reverse the free induction signal long after it has disappeared completely. The optical analogue of spin echoes, photon echoes on optical transitions, were first observed in 1964 (shortly after the invention of the laser) by Kurnit, Abella, and Hartmann [96].

The spin echo pulse sequence is outlined in Figure 3.3. Initially, we apply a $\pi/2$ pulse to an ensemble which results in an FID signal. A period $\tau/2$ after the initial pulse, a π-pulse is applied, rotating the Bloch vector of each ion around the $+x$ axis by 180°. The π-pulse effectively reverses the evolution of the spin vectors. After a further delay $\frac{\tau}{2}$, the spin vectors return to a macroscopic coherence and radiate a signal, the echo of the original FID. The delays before and after the π pulse are referred to as the dephasing and rephasing periods respectively.

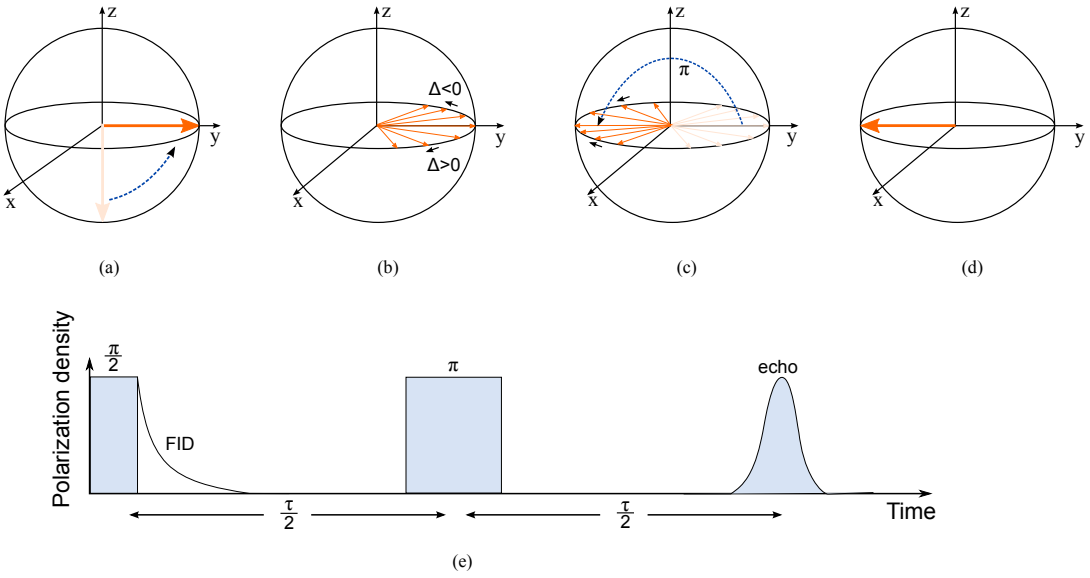

Figure 3.3: The Bloch sphere representation of the two pulse spin echo technique. (a) The ensemble is driven into a 50-50 superposition state by a $\frac{\pi}{2}$-pulse. (b) The Bloch vectors of individual subgroups start to precess around the Bloch sphere with a rate and direction decided by their detunings. (c) The $y$components of the Bloch vectors are inverted by a π-pulse and the vectors begin to refocus. The ensemble starts to radiate an echo signal. (d) The individual Bloch vectors are all aligned and the echo signal reaches its maximum value. (e) The pulse sequence and the echo signal.

Similar to Equation 3.5, the Bloch vector $\boldsymbol{M_{x+iy}}$ for each subgroup of ions at the echo point is dependent on the phase accumulation over the total evolution time τ, which is decided by the frequency detuning $\Delta\omega_j$ [85, 85]

$$\boldsymbol{M_{x+iy}}(\tau) = \sum_j \boldsymbol{M_{0,j}} \exp\left[i \int_0^\tau s(t)(\Delta\omega_{s,j} + \Delta\omega_j(t))dt\right] \tag{3.8}$$

where $\Delta\omega_{s,j}$ is the static perturbation originating from the inhomogneous broadening mechanisms while $\Delta\omega_j(t)$ is the dynamic perturbation involving homogneous broadening and spectral diffusion. The function $s(t)$ is the step describing the phase reversal caused by the π pulse, which is defined by

$$\begin{aligned} s(t) &= +1 \qquad \text{if} \quad t < \tau/2 \qquad \text{(dephasing period)} \\ &= -1 \qquad \text{if} \quad t > \tau/2 \qquad \text{(rephasing period)} \end{aligned} \tag{3.9}$$

The phase accumulation due to the static detuning during the dephasing and rephasing intervals cancels, thus the echo amplitude is governed by the dynamic contribution. Then Equation 3.10 can be reduced to

$$\boldsymbol{M_{x+iy}}(\tau) = \sum_j \boldsymbol{M_{0,j}} \exp\left[i \int_0^\tau s(t)\Delta\omega_j(t)dt\right] \tag{3.10}$$

The dynamic contribution results in a difference in phase accumulation between the de-

phasing and rephasing periods. The amount of the phase accumulate for different subgroups are not identical, thus the Bloch vectors are not aligned at the echo point. This decreases the size of the total Bloch vector and accordingly decreases the echo amplitude. With a longer delay, the differences in the phase accumulation among subgroups increase, resulting in a smaller size of the total Bloch vector. Changing the delay τ sequentially allows the phase shift due to the environment to accumulate over different periods, providing a way to work out the decay rate $1/T_2$.

In the above discussion, the state evolving over a pulse period is describe by only considering the action of the pulse on the initial state and the evolution during the pulse is neglected. In order to make this approximation valid, the Rabi frequency Ω of the driving field for spin echoes, must be significantly larger than the linewidth of the transition:

$$\Gamma_{inh} \ll \Omega. \tag{3.11}$$

In this equation, γ is the gyromagnetic ratio and $\Omega = \gamma B_1$ for spin echoes, where B_1 is the amplitude of the RF driving field. Under this assumption, the action of the driving field for all ions is the same and a pulse of such a driving field is called a hard pulse.

3.1.3 Spin echo decays

The two pulse spin echo decay in Equation 3.10 is based on the assumption that the lifetime of the excited state is much longer than the coherence time. In this case, the T_1 process which tends to degrade an individual Bloch vector is considered to occur long after the ensemble loses coherence. This assumption holds true for the hyperfine transitions in Eu^{3+}:Y_2SiO_5, the system investigated in this thesis. The coherence time at cryogenic temperature of a diluted sample is at the order of 10 ms, which is much shorter than the lifetime of 23 days [17].

For hyperfine transitions in Eu^{3+}:Y_2SiO_5, the dephasing of Eu^{3+} Bloch vectors are due to the fluctuating magnetic field caused by the random spin flips of host Y^{3+} spins. In order to work out the decay function of the echo amplitude in Equation 3.10, this can be treated by considering the problem to be about the echo decay of the spins of interest , or A spins, in the presence of a random magnetic field due to an array of spin-1/2 B spins. In this model, the concentration of the A spins is assumed to be sufficiently low that A-A interactions can be ignored. Such a problem of the echo decay of the A system in a bath of B spins was studied by Mims et al. [85, 85, 97]. The rest of this section provides a brief review of these studies.

I start the discussion from Equation 3.10. For a spin echo, the rephasing for different subgroups will be the same. The echo amplitude decay shape is then given by the phase factor of the A spins due to the phase accumulation over the total evolution time τ [85, 85]. The effect of the B spin bath can be understood by considering how it affects a single subgroup. For the j-th subgroup, the phase accumulation is written

$$\varphi_j(\tau) = \int_0^{\tau} s(t)\Delta\omega_j(t)dt. \tag{3.12}$$

The phase accumulation is due to the dynamic frequency shift caused by the magnetic dipolar interaction of the A spin with the array of B spins. The dynamic frequency shift

$\Delta\omega_j(t)$ can, therefore, be written

$$\Delta\omega_j(t) = \gamma_A \sum_k [\boldsymbol{m_k}(t) - \boldsymbol{m_k}(0)](1 - 3\cos^2\theta_k)/|\boldsymbol{r_k}|^3, \tag{3.13}$$

where γ_A is the gyromagnetic ratio of the A spin[1], $\boldsymbol{r_k}$ is the distance between the A spin and the k-th B spin and θ_k is the angle between $\boldsymbol{r_k}$ and the z axis of the Bloch vector. The sum is taken oven all B spins in the lattice. $\boldsymbol{m_k}(t)$ is the time-varying z component of the k-th B-spin magnetic moment, i.e.,

$$\boldsymbol{m_k}(t) = \gamma_B \boldsymbol{S_z^k}(t), \tag{3.14}$$

where γ_B is the gyromagnetic ratio and $\boldsymbol{S_z^k}$ is the nuclear spin of B spins. As B ions are a spin-1/2 system,

$$|\boldsymbol{S_z^k}| = 1/2. \tag{3.15}$$

The effect of the dynamics of the B spin bath on an A spin is due to the various B spin lattice configurations and the time-varing magnetic moment $\boldsymbol{m_k(t)}$ for each B spin. From Equation 3.10 and Equation 3.12, the echo amplitude of the ensemble A spin for a given total evolution time τ is then written [85]

$$E(\tau) = \left\langle\left\langle \exp i \int_0^\tau s(t)\gamma_A \left\{ \sum_k \left[\boldsymbol{m_k(t)} - \boldsymbol{m_k(0)}\right] \right.\right.\right. \tag{3.16}$$

$$\left.\left.\left. \times(1 - 3\cos^2\theta_k)/\boldsymbol{r_k^3} \right\} dt \right\rangle_{Av(1)} \right\rangle_{Av(2)},$$

where $Av(1)$ is the average of different subgroups of A spins while $Av(2)$ is the average over the possible configurations of B spins surrounding an A spin.

An exact solution of Equation 3.16 is not possible and statistical models describing the reconfiguration of the B spin bath are needed to find suitable averages. In all statistical models, the decay rate of the A spin is directly related to two parameters, one is the B spin bath reconfiguration rate R, which is equivalent to the inverse of the population lifetime, $R = 1/\tau_1$ of the bath. The other is the magnitude of the frequency shift caused by the reconfiguration of the B spin bath as defined in Equation 3.13.

Herzog et al demonstrated it is reasonable to assume that the average over all bath configurations results in a Gaussian lineshape independent of time [97]. They also assumed that all B spins are the same and therefore can be averaged over using the same probability distribution. When the spin B bath configuration rate is fast compared to the total evolution time τ of spin A, namely $R\tau \gg 1$, a large number of randomly selected B spins reverse their orientation over the time τ. These randomly selected elements of the Gaussian distribution also forms a Gaussian distribution. Then, an average of Equation 3.16 results in a single exponential decay of the two pulse spin echo amplitude

$$E(\tau) \propto \exp\left(-\frac{\Delta\omega_A^2\tau}{2R}\right), \quad R\tau \gg 1, \tag{3.17}$$

[1] I explain the concept by considering that A spins are isotropic to simplify the explanation, though typically, the rare earth spins in our system are not isotropic.

where $\Delta\omega_A$ is the averaged frequency shift of an A spin due to the reconfiguration of B spin bath and R, as defined in the last paragraph, is the B spin configuration rate. Equation 3.17 can be reformulated as

$$E(\tau) \propto E_0 \exp(-\tau/T_2), \tag{3.18}$$

where

$$T_2 = 2R/\Delta\omega_A^2 \tag{3.19}$$

If the configuration rate of B spins is slow compared to the evolution time τ, such that $R\tau \ll 1$, then over the period of τ only a small number of B spins flip. Though, over a long time scale, the average over all bath configurations is assumed to be a Gaussian lineshape, it is not possible to argue that a small number of randomly selected elements of a Gaussian distribution also form a Gaussian distribution [98]. A different method was used to average Equation 3.16 by Klauder and Anderson [99] in this limit, where the B-spin flips were considered to result in a "diffusion" of the distribution of the local field perturbation. In a time period $\Delta t \ll 1/R$, there is a small number of randomly selected B spins flips, which is equivalent to the insertion of $n_B R\Delta t$ additional spins, each with magnitude of γ_B, at random sites in the lattice. Here n_B is the total number of the B spins in the bath. An average over the A spins that independently experience such a B configuration results in a Lorentzian distribution of the A transition frequencies [98]. That is, an A spin subgroup with an initial transition frequency ω_a will broaden into a distribution [100]

$$K(\omega - \omega_a, \Delta t) = \frac{(2R\Delta\omega_{1/2}\Delta t)/\pi}{(\omega - \omega_a)^2 + (2R\Delta\omega_{1/2}\Delta t)^2} \tag{3.20}$$

where $\Delta t = t - t_0$ and $\Delta\omega_{1/2}$ is the full width at half maximum of the A spin frequency deviation defined by the distribution of all possible bath configurations and Δt. The concept of $\Delta\omega_{1/2}$ is equivalent to $\Delta\omega_A$ in Equation 3.17, but were labelled differently in the corresponding papers. Klauder and Anderson [99] show that this results in the echo decay function:

$$E(\tau) \propto \exp\left[-(\tau/T_M)^2\right], \quad R\tau \ll 1 \tag{3.21}$$

where

$$T_M = 1.41(R\Delta\omega_{1/2})^{-1/2}. \tag{3.22}$$

In this equation, T_M, the phase memory time, is used rather than the coherence time T_2, because the decay rate is time dependent. T_M is defined as the evolution time which brings about a $1/e$ attenuation of the echo amplitude.

In between these two extremes, when $R\tau \approx 1$, there is no simple statistical approximation [85] and consequently no decay functions have been derived.

The two distinctly different spin echo decays, Equation 3.18 and Equation 3.21, are derived depending on the relative time scale of the echo and B spin bath reconfigurations. In the coherence measurement, as we are only concerned with the delay for the echo amplitude drops to $1/e$ of the maximum value, the evolution time τ is generally chosen to be comparable to the inverse of the perturbation magnitude caused by the bath reconfiguration. Thus, the limiting conditions for the two different echo envelopes can be reformulated in terms of the static local field broadening $\Delta\omega_{1/2}$. The condition $R\tau \gg 1$ is equivalent to $R \gg \Delta\omega_{1/2}$ and the condition $R\tau \ll 1$ is equivalent to $R \ll \Delta\omega_{1/2}$. The two echo decay

formulas can then be summarized as : the echo decay has an exponential format when the B spin bath reconfigures at a rate fast compared to the frequency perturbation it causes on the A spins and the echo decay has a non-exponential format when the reconfiguration rate is slow compared to the frequency perturbation.

3.1.4 Dynamic decoherence control

The two pulse spin echo technique described above completely removes the decoherence due to static broadening in an ensemble, but it does not remove the decoherence due to dynamic broadening. Dynamic decoherence control (DDC) is a strategy for fighting decoherence due to dynamic broadening. It works by applying a sequence of control fields periodically, usually fast and strong pulses in cycles, to alter the dynamics of the system and refocus the dephased ensemble Bloch vectors. In contrast to quantum error correlation (QEC), for example, DDC does not require additional measurement or memory resources. Hence it can be integrated with other error-avoiding or error-correcting techniques in a straightforward manner to help achieve fault-tolerant control.

The DDC technique works effectively only if the reconfiguration time τ_1 $(= 1/R)$ of the dephasing bath is longer than the time scale τ_c at which pulses can be applied to the system. Then the frequency detunings due to the dephasing environment remain effectively static during each pulse period and are therefore rephased. If the decoherence contribution is rapidly fluctuating, with a correlation time much shorter than the time required for the application of refocusing pulses, then this type of noise cannot be refocused by a DDC pulse sequence.

The discussion above shows that, in order to fight decoherence, DDC repetition rate needs to be faster than the reconfiguration rate R of the dephasing bath. However, there are practical challenges if the DDC pulse rate is too fast. First, in order to make the pulses hard pulses such that the evolution during the pulses is neglected, the DDC pulse rate is required to be lower than the Rabi frequency while the Rabi frequency is often limited by the possible RF power supply. Secondly, a high pulse rate means that the pulse number is huge. Since the precision of any experimentally accessible operation is finite, the number of pulses that can be applied without degrade the signal is limited by the pulse errors. For these two reasons, to realise the DDC effective, it is necessary to keep the pulse rate low, which is only possible when the reconfiguration rate of the dephasing bath is low .

For the system discussed in this thesis, hyperfine transitions in Eu^{3+}:Y_2SiO_5, the decoherence is dominated by the magnetic field perturbation due to the random spin flips of the host Y^{3+} ions. Though the Y^{3+} spins flip at a very fast rate at zero field, this flipping rate can be largely reduced in the presence of an external field principally because the field induces a frozen core as discussed in Section 2.5.3. The frozen-core effect divides the host Y^{3+} ions into two groups, that are bulk Y^{3+} ions, far away from Eu^{3+} ions, producing small amplitude but rapid magnetic field perturbations, and frozen core Y^{3+} ions, near the Eu^{3+} ions, generating large but slow magnetic field perturbations. If, in addition, the applied field is chosen such that the transition of interest is a ZEFOZ transition, the rapid and small magnetic field perturbations originating from the bulk Y^{3+} ions have a negligible effect on the hyperfine transition frequency due to the small field sensitivity. The remaining decoherence contribution is the large field perturbations from the frozen core Y^{3+} ions. Since the frozen core reconfigures at a suppressed rate, a DDC sequence with relatively low repetition rates should be quite effective in removing the decoherence. To summarize, ZEFOZ removes the small and fast decoherence effect of the bulk Y^{3+} and

DDC removes the large and slow decoherence effect of the frozen-core Y^{3+}. As we can consider ZEFOZ technique as a high frequency decoherence filter and DD technique a low frequency decoherence filter, their combination is likely to be very effective.

Applying DDC pulses at a ZEFOZ transition have another benefit. If the field is detuned away from a ZEFOZ field, driving a Eu^{3+} transiton using a DDC pulse will slightly change the magnetic moment of Eu^{3+}. As discussed in Section 2.5.4, a change in the europium magnetic moment would accordingly cause a reconfiguration of the Y^{3+} bath, which will have a back action on Eu^{3+}. When a large number of DDC pulses are applied, the accumulated error due to this issue can decrease the DD effectiveness. Whereas, if the DDC pulses are applied at a ZEFOZ transition of Eu^{3+}, as discussed in Section 2.5.4, driving the Eu^{3+} transition does not change its magnetic moment, thus will not disturb the Y^{3+} system. This means that, the combination of ZEFOZ, the frozen core, and DDC can result in significant extension of the coherence times in this system.

Two different DDC pulse sequences were used in the experiments presented in this thesis. The first sequence implemented was the CPMG(Carr-Purcell-Meiboom-Gill) [101] spin echo sequence, which is commonly used in NMR experiments. It provide a simple and effective way to test the DDC effectiveness. As shown in Figure 3.4, the pulse sequence has the following format:

$$(\pi/2)_x - \tau_c/2 - \pi_y - \tau_c - \pi_y - \tau_c - \pi_y - ...\pi_y - \tau_c/2 - echo.$$

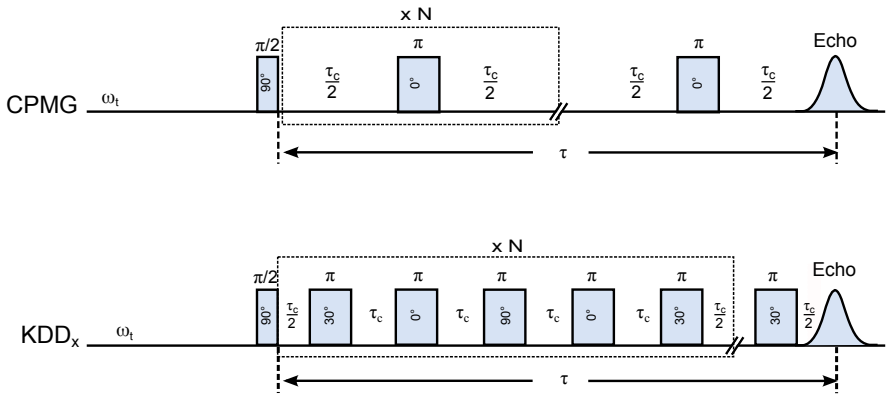

Figure 3.4: CPMG and KDD_x pulse sequences. Here ω_t is the frequency of the driving field, N is the repetition number of the indicated pulse sequence, τ_c is the pulse interval and τ is the total evolution time.

Although the CPMG sequence is commonly used to extend coherence, the method is only effective in preserving quantum states that possess a particular phase. Hence, it is not suitable for use in a practical quantum memory, which is required to store arbitrary quantum states. To test the suitability of the Eu^{3+}:Y_2SiO_5 system for arbitrary quantum state storage, another DDC sequence, known as KDD_x, was also used. The KDD_x sequence is effective in preserving arbitrary states and is robust against errors due to pulse area and off-resonant excitation [102]. It has the general format:

$$(\pi/2)_{\pi/2+\phi} - \tau_c/2 - \pi_{\pi/6+\phi} - \tau_c - \pi_\phi - \tau_c - \pi_{\pi/2+\phi} - \tau_c - \pi_\phi - \pi_{\pi/6+\phi}... - \pi_{\pi/6+\phi} - \tau_c/2 - echo,$$

which is equivalent to a π pulse rotation around the axis defined by ϕ followed by a $-\pi/3$ rotation around the z axis in the Bloch sphere. In our case, the rotation axis is set to $\phi = 0$ axis and the pulse sequence is shown in Figure 3.4.

3.2 Optical preparation and readout

While this thesis is concerned with the spin coherence time on hyperfine levels, optical frequencies are used for experimental preparation and echo readout. Prior to each RF pulse sequence in any coherence time measurement, spectral holeburning was used to to prepare a population difference between the two hyperfine levels of interest. To read the echo, Raman heterodyne detection was used to detect the echo signal optically. This section provides a brief introduction of these two techniques.

3.2.1 Spectral holeburning

Spectral holeburning is an optical pumping progress that uses a narrow-band laser to selectively excite a small subset of ions in the ensemble. In order to introduce the spectral holeburning process, the following conditions are imposed based on the sample and the laser used in the experiments presented in this thesis:

- The zero-field hyperfine structure of the ion is composed of three doubly degenerate hyperfine states for both ground and excited electronic states.
- The hyperfine transition frequencies, $\omega_{1,2,3,4}$ as shown in Figure 3.5 are 10-100 MHz, which is in the range of RF frequencies.
- The optical inhomogeneous linewidth is $\Gamma_{\text{inh}} \simeq 1$ GHz, and it is much broader than the homogeneous linewidth which is $\Gamma_{\text{h}} \simeq 100$ Hz.
- The linewidth of laser is narrow with a linewidth $\Gamma_{\text{laser}} \simeq 1\,\text{kHz}$, which is much narrower than the optical inhomogeneous linewidth. This allows the possibility to burn a narrow feature.
- The lifetime of the spin states is many orders of magnitude longer than that of the electronic excited state so there is no spin decay during the pulse sequences.

As shown in Figure 3.5(a), the three hyperfine ground states are equally occupied by the ions initially. A narrow-band laser at fixed frequency ω_b is used to excite a small subgroup of ions to the electronic excited state. The ions in the excited state can then decay to any of the hyperfine ground states by spontaneous emission. Some ions end up in the same hyperfine ground state from which they originated while others decay to different states. The former are excited again as the laser is on continuously, while the latter are no longer resonant with the laser. After many optical cycles, all the ions initially resonant to the laser field have been pumped to a different spin state and no longer interact with the laser at this frequency (Figure 3.5(c)). By sweeping the laser over the inhomogeneous line, a decrease of absorption at ω_{b} is seen due to the reduced ground state population of ions that are resonant at that frequency. This appears as a hole in the inhomogeneous absorption spectrum (Figure 3.5(d)).

In Eu^{3+}:Y_2SiO_5, there are several factors that can affect the depth of the hole, including the optical pumping rate, the relative optical oscillation strengths of the different

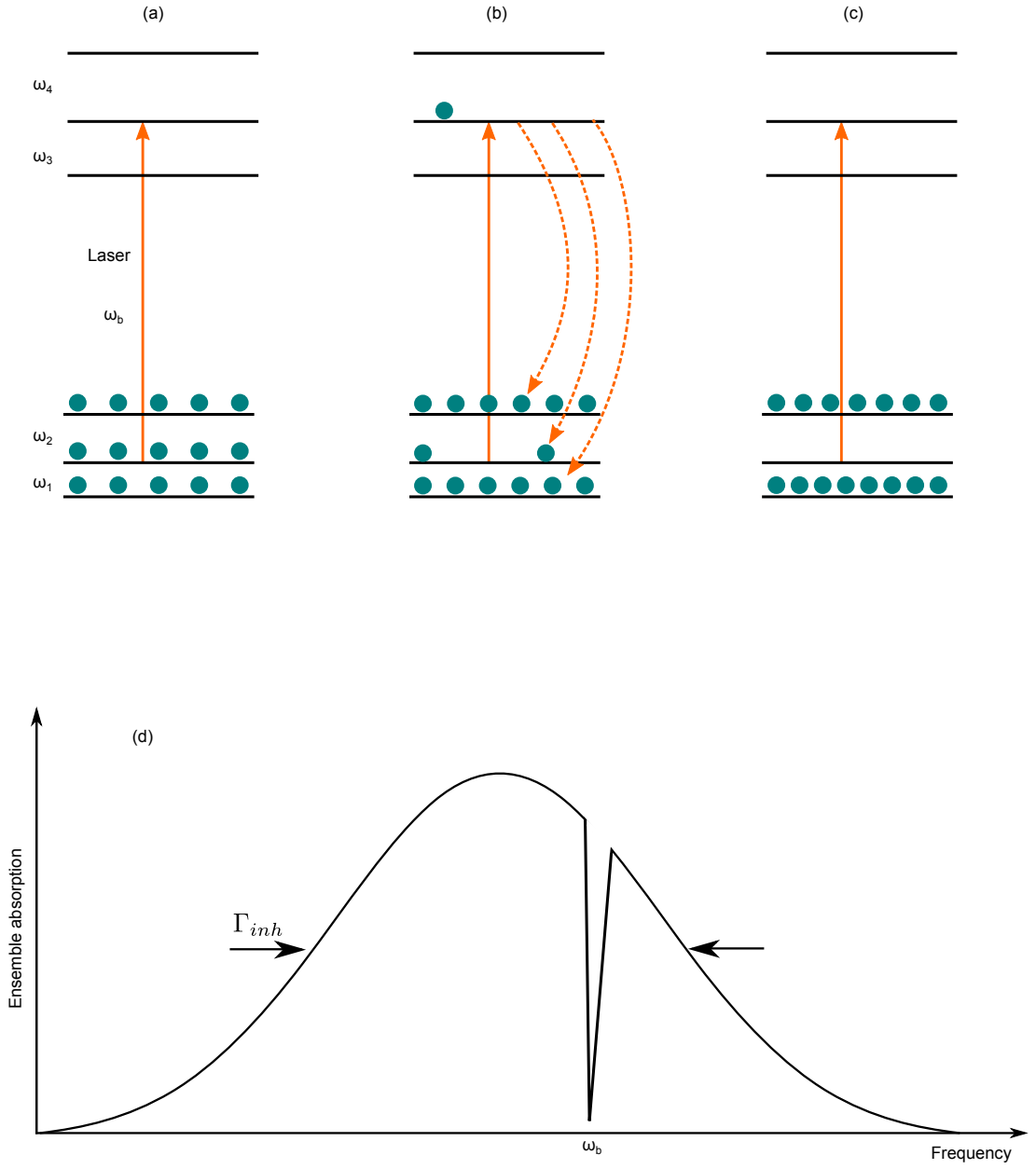

Figure 3.5: Illustration of spectral hole-burning. (a) All three hyperfine ground state are equally populated and a laser with frequency ω_b is used to pump the ions in the middle state to the optically excited state. (b) The excited ions can decay to any of the hyperfine ground states, but only those that decay to the middle state can be pumped by the laser again. (c) After many iterations of excitation and decay, there are no ions that are still resonant with the laser. All the ions end up in the non-resonant ground states. (d) A 'hole' is burned in the inhomogeneous profile. Only one subgroup of ions is considered here to simplify the illustration. In the actual holeburning experiment, the optical field drives multiple subgroups. Also, there are sideholes and antiholes in actual experiment, which is not shown in this figure because it is not relevant to my experiments.

transitions and the hyperfine lifetime. The return of the ions in Figure 3.5(c) to the initial ground state is through spin-lattice relaxation and the rate is different for each system. Rare-earth solids typically have long hyperfine lifetimes, in the present case is a few weeks [17], so a spectral hole can persist for a long period.

3.2.2 Raman heterodyne detection

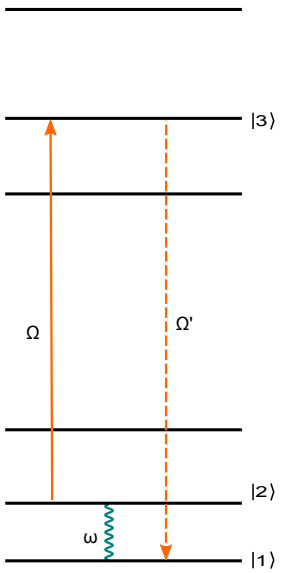

Figure 3.6: An illustration of Raman heterodyne detection. An optical field with frequency Ω sets up coherence between $|2\rangle$ and $|3\rangle$ and an RF field with frequency ω sets up coherence between $|1\rangle$ and $|2\rangle$, which results in coherence between all three levels $|1\rangle$, $|2\rangle$ and $|3\rangle$.

Raman heterodyne detection is an RF-laser double-resonance technique, introduced by Mlynek et al. in 1983 [103]. It is a method for optically detecting NMR. It employs heterodyne detection to measure the coherent Raman emission stimulated by a resonant RF field and a laser field in a three-level quantum system. The technique is illustrated in a system with three ground and excited hyperfine states in Figure 3.6. An optical field with frequency Ω resonantly drives the electronic transition $2 \rightarrow 3$ and simultaneously a RF field with frequency ω drives the transition $1 \rightarrow 2$ between the nuclear spin states. This stimulates an optical field with the frequency $\Omega' = \Omega + \omega$ by establishing coherence between states $|1\rangle$, $|2\rangle$ and $|3\rangle$. With a photodetector to detect the transmitted optical field, the two frequency components Ω and Ω' will result in a heterodyne beat signal $\omega = |\Omega' - \Omega|$.

The size of the beat signal is proportional to the ion population difference between the two hyperfine ground state $|1\rangle$ and $|2\rangle$. If necessary, this population difference can be prepared using spectral holeburning as discussed in the previous section. The magnitude of the signal is also dependent on the oscillator strengths of all three transitions involved as well as the intensity of both the RF field and optical field.

Raman heterodyne spectroscopy is similar to the method of optical detection of magnetic resonance (ODMR). The ODMR technique works by using a laser field to burn a spectral hole in a optical transition and then using a RF field to sweep slowly through a hyperfine transition. This hyperfine transition is driven when the RF field becomes

resonant, resulting in the return of the ions to the original ground state with which the laser is resonant. The hole is unburned, so the laser absorption is increased. The main difference is that Raman heterodyne detects coherent emission, and so is faster and has higher resolution than ODMR, which detects incoherent emission.

Chapter 4

Hyperfine coherence time extension in Eu^{3+}:Y_2SiO_5

Mechanisms for hyperfine decoherence in Eu^{3+}:Y_2SiO_5 were discussed in Chapter 2. The dominating source for dephasing of the coherence of the hyperfine transition is the fluctuating magnetic field at the Eu^{3+} site caused by the random spin flipping of the Y^{3+} ions in the host. An effective way to minimize this dephasing is to employ the ZEFOZ method (Section 2.5). The ZEFOZ method works by applying a magnetic field with a specific field magnitude and orientation such that a hyperfine transition is not sensitive to the field perturbation to first order.

The goal of the experiments reported in this chapter was to use the ZEFOZ method to extend the coherence time of the hyperfine transitions in Eu^{3+}:Y_2SiO_5. The ZEFOZ transitions in Eu^{3+}:Y_2SiO_5 occur at field magnitudes of a few tesla. Applying such a high magnetic field has the added benefit of inducing a frozen core which should largely suppress the flipping of the yttrium spins. This is expected to result in a decreased field fluctuation at the Eu^{3+} sites and accordingly further increases the coherence time (Section 2.5). In addition, the reduced yttrium flipping rate allows the possibility of applying DDC pulses to fight decoherence and extend the coherence time. As stated in the previous chapter, a significant extension of hyperfine coherence time in Eu^{3+}:Y_2SiO_5 is expected with the combined effect of ZEFOZ, frozen core and DDC pulses.

In this chapter, I first introduce the ZEFOZ transition to be investigated and the experimental set-up for the measurements. Then I introduce the method used to precisely align the magnetic field for achieving a ZEFOZ transition. After that, I present the experimental coherence results. Finally, a discussion of the results is presented.

4.1 ZEFOZ transition

The ZEFOZ magnetic fields for Eu^{3+}:Y_2SiO_5 were calculated using the reduced spin Hamiltonian determined by Longdell. et al [22] and are shown in Figure 2.9. The investigation here focuses on a critical point of the $3/2 \leftrightarrow -3/2$ transition that is predicted to occur at an applied field of 1.35 ± 0.07 T (Figure 4.1). This point was chosen because it has low curvature and occurs at a low magnetic field, which is experimentally simpler to work with. The field orientation of this point relative to the D_1, D_2 and C_2 axes is shown in Figure 4.2. At this field, the transition frequency is 12.45 MHz and the maximum curvature $|S_2| = 21.7\text{MHz/T}^2$. Using the calculated value of the field fluctuation $|\boldsymbol{\delta B}| = 8.0\ \mu$T (Section 2.5.2), and according to Equation 2.12, the expected coherence time is 229 s for a perfectly aligned magnetic field, which corresponds to a decoherence

rate $(1/T_2)$ of 4.4×10^{-3} s^{-1}.

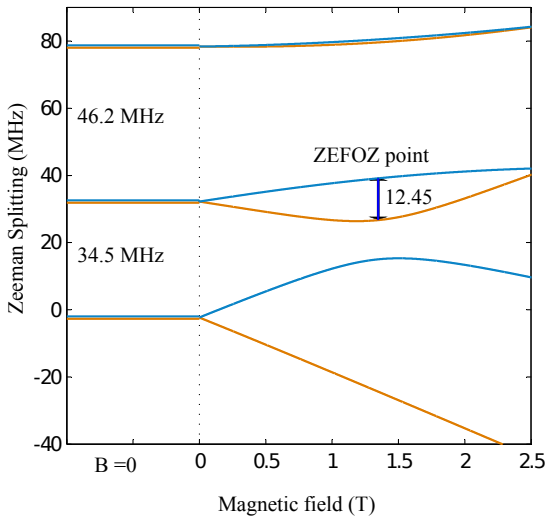

Figure 4.1: This graphs shows the ZEFOZ transition investigated. It is a critical point of the $3/2 \leftrightarrow -3/2$ transition of the $^7F_0$ state. The energy levels, calculated using the reduced spin Hamiltonian in [22], were plotted as a function of the magnetic field magnitude increased from zero in the ZEFOZ field direction.

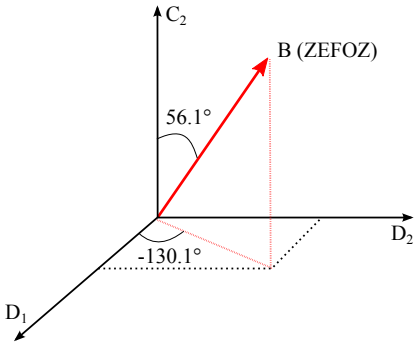

Figure 4.2: The calculated field orientation of the critical point investigated in the coordinate frame of $[D_1, D_2, C_2]$.

4.2 Experimental setup

Coherence measurements of the system were performed using two pulse spin echoes. The echo signals were observed optically, using Raman heterodyne detection (Section 3.2.2), via the $^7F_0 \rightarrow {}^5D_0$ 'site1' transition at 579.87985 nm (air) [77]. The optical and RF pulse sequences used in the spin echo experiments are shown in Figure 4.3.

Prior to each spin echo pulse sequence, the system was prepared with an optical burn and re-pump scheme to isolate the transition of interest. First, the laser frequency was swept over 45 MHz on the low-frequency side of the $-3/2(^7F_0) \leftrightarrow +3/2(^5D_0)$ transition

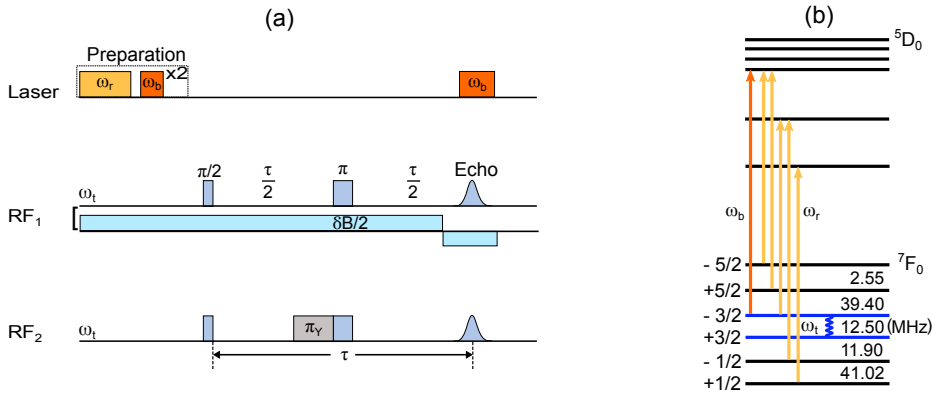

Figure 4.3: (a), Pulse sequences used in the experiments. The optical burn frequency ω_b was used to prepare a population difference between the $+3/2$ and $-3/2$ states prior to the RF pulses, and to optically detect the spin echo signal. The re-pump frequency $\omega_r = [(\omega_b - 45\text{ MHz}) \rightarrow \omega_b]$, scanning over 45 MHz, was used to pump ions back to the $\pm 3/2$ states at the end of the sequence. RF_1 shows the RF pulses for two pulse spin echo detection. The indicated polarity reverse of $\boldsymbol{\delta B}/2$ was for phase sensitive detection (Section 4.3.4), which was used for the final field alignment. Phase sensitive detection works by observing the phase shift of the echo by reversing the polarity of a perturbing magnetic field ($\boldsymbol{\delta B}/2$) prior to the echo detection period. The polarity change of $\boldsymbol{B}/2$ was realized by reverse the current driving the pertubing coil. RF_2 is for measuring the frozen core Y^{3+} dynamics where a perturbing π_Y-pulse, resonant with the spin frequency of the yttrium ions, was applied just prior to the Eu^{3+} π-pulse. (b) The hyperfine transition frequencies as labelled are the theoretical values at the ZEFOZ field investigated.

for 2 s (ω_r). The effect of the sweep was to optically re-pump ions in this subgroup to the $+3/2$ ground state, while ions in other subgroups were shelved to the $\pm 1/2$ ground states. A further pulse resonant with the $-3/2(^7F_0) \leftrightarrow +3/2(^5D_0)$ transition (ω_b) ensured that the $-3/2$ ground state was emptied. Both the re-pump (ω_r) and burn (ω_b) were repeated a second time to achieve the desired population distribution amongst the ground-state hyperfine levels. This preparation scheme was used because it allowed the transition of interest to be initialised independent of the exact magnitude and direction of the applied magnetic field as long as it was close to the ZEFOZ field.

Once the ensemble was prepared in the $+3/2$ ground state, an RF pulse sequence ($RF_{1,2}$) was applied depending on the measurement of interest. In all cases, the resultant spin coherence was read out with Raman heterodyne detection by applying a further optical pulse at ω_b at the time of rephasing.

The schematic diagram of the experimental setup to achieve and measure the long coherence times is shown in Figure 4.4. A 0.01% doped Eu^{3+}:Y_2SiO_5 crystal from Scientific Materials Corp., rectangularly shaped with dimensions of $5 \times 5 \times 3$ mm along the D_1, D_2 and C_2 axes respectively, was used for the experiment. The crystal was maintained at 2.0 K during the measurements in a Oxford SM-2000 bath cryostat that incorporates a superconducting magnet. The superconducting magnet, capable of providing stable magnetic fields of up to 15 Tesla, was used as the source of a DC field for the ZEFOZ transition. The RF signal on the sample was produced by a six turn RF coil with a diameter of 6 mm. The RF coil was driven by a 40 dBm RF amplifier, which resulted in a Rabi frequency $\Omega_{RF} = 7.9$ kHz. The RF pulse was generated by a Spincore Radio Processor, and controlled by RF switches. The RF coil was aligned perpendicular to

the main axis of the superconducting magnet so as to eliminate the interaction with the magnet.

The optical transition was driven by a highly frequency stabilized dye laser (sub-kHz linewidth), which was directed at the sample from below the magnet. The light was then reflected by a mirror, passing through the crystal a second time, and finally detected by a 125 MHz bandwidth Si photo-receiver. The laser power incident on the crystal was 30 mW, gated by a double pass 80 MHz acousto-optic modulator (AOM) to avoid laser radiation on the sample during the RF pulse period. The AOM was driven by a purpose-built Direct Digital Synthesis (DDS) RF source, built by the RSPE (Research School of Physics and Engineering of ANU) Electronics Unit, referred to by the project number as J850. It was controlled by the TTL channels from a Spincore Pulse Blaster through a series of RF switches. The J850 DDS unit is capable of providing scannable RF frequencies which enabled implementation of the re-pump pulse sequence. Synchronization of the RF pulses was realized by using a computer to control the Radio Processor, J850 unit, and the Pulse Blaster.

The diagram in Figure 4.4 shows that the Raman heterodyne signal, detected as a beat, was amplified and split into two signal channels and mixed respectively with two local oscillators. In this case both phases, different by 90°, of the signal were observed. Such a reading strategy was set up for the phase sensitive detection used for the field alignment, where the phase of the echo signal was concerned, as discussed in the next section. While the phase of the echo was of interest during the phase sensitive detection, for coherence measurement, only the echo amplitude was of interest. Thus a single local oscillator channel was used during the coherence measurements.

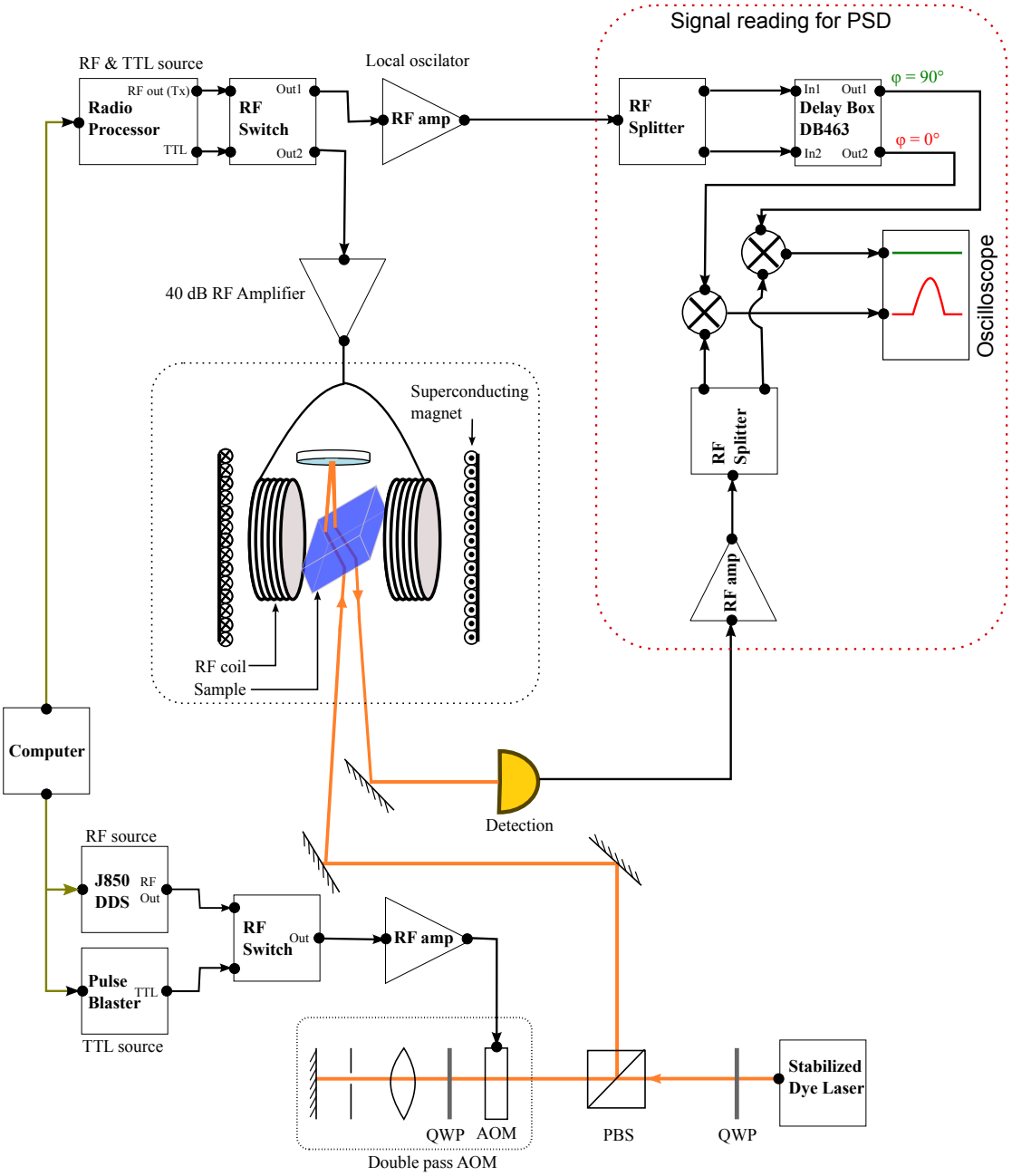

Figure 4.4: Experiment set-up for spin echo measurements. 'HWP' and 'QWP' stand for half wave plate and quarter wave plate respectively while 'PBS' is the polarising beam splitter. The box 'Delay Box DB463' is a device used to adjust the phase of the input RF signal by extending the length of the cable, where '$\varphi = 90°$' means that the phase of an input signal is changed by 90°. The rectangular area indicated with the red dotted line is the signal reading strategy during the final ZEFOZ field alignment using phase sensitive detection (PSD, Section 4.3.4). In the PSD, both phases of the echo signal were observed. During the spin echo measurements, however, only the echo amplitude was recorded.

4.3 ZEFOZ magnetic field alignment

4.3.1 Challenges in field alignment

Before any spin echo measurement could be performed, the field had to be aligned such that the transition investigated was at the critical point, and this was the major challenge of ZEFOZ. The principle of ZEFOZ requires that the error in the applied magnetic field value should be within the magnetic field fluctuations, which is ∼0.08 G for Y_2SiO_5 (Section 2.5.2). This number is only 2.6×10^{-4}% of the ZEFOZ field magnitude of 1.35 T. One way of aligning the field is to look at the hyperfine structure and match it to the theoretical values at the ZEFOZ field. This method, however, can only be used for coarse alignment of the field, and is insufficient to align the magnetic field with the high accuracy required (with error less than 2.6×10^{-4}%). This is because at this small field perturbation, the frequency change is very small compared to the transition's inhomogeneous linewidth, and does not produce a visible change in the hyperfine structure. The hyperfine inhomogneous linewidth of the sample used is 10 kHz. As shown in Figure 4.6 (a), when the Zeeman splitting approaches the ZEFOZ transition, even with a field detuning of 4 G from the ideal critical point, the frequency changes only by a few hertz. This frequency shift is less than 0.1% of the inhomogenous linewidth so it would not create visible change in the hyperfine structure, but would reduce the coherence time by two orders magnitude.

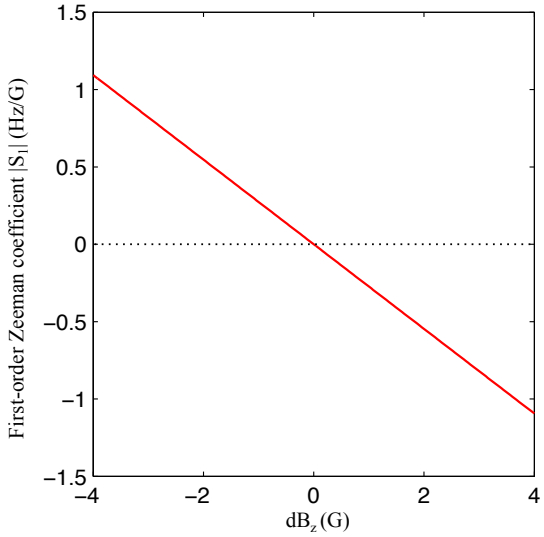

Figure 4.5: Calculated first order Zeeman coefficient $|\boldsymbol{S_1}|$ against magnetic field when the field is adjusted off the ideal ZEFOZ field value along z axis by ±4 G.

One of the other challenges of aligning a critical point field is that the turning points along three dimensions need to be achieved simultaneously. Any field offset in any one of these three directions will lead to a substantial first-order component in the field sensitivity in all directions as demonstrated in Figure 4.6 (b) and (c). Figure 4.6 (b) is a two-dimensional spectrum in the xy-plane while the magnetic field along z is fixed at the critical point. In Figure 4.6 (c), the magnetic field along the z axis is detuned by 0.5 G, it is obvious that the frequency gradient along the x and y axis changes significantly as well. Moreover, as shown in Figure 4.6 (a), the ZEFOZ point investigated is a saddle point with a maximum along the x axis and minimums along the two other dimensions.

It is much easier to work with an absolute maximum or an absolute minimum critical point. For instance, if it was an absolute maximum critcal point, it is efficient to simply maximize the frequency. Hence, being a saddle point, it increases the degree of difficulty in approaching the critical point by observing the hyperfine structure. In addition, the theoretical ZEFOZ value is just a rough reference with its accuracy limited by the fitting error of the Hamiltonian parameters which is up to ∼4%, or 5 G.

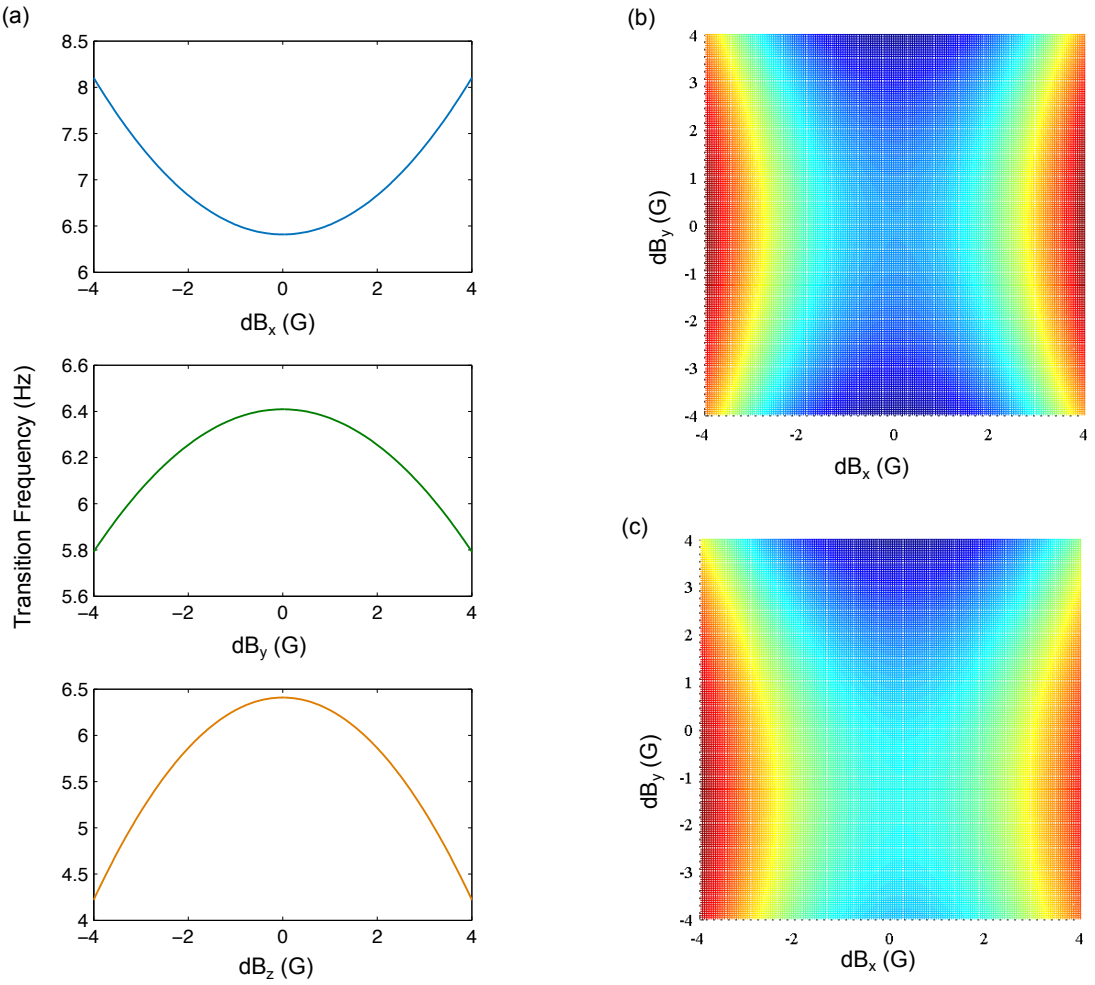

Figure 4.6: Frequencies of the $-3/2 \rightarrow +3/2$ transition around the ZEFOZ point at 1.35 T. (a), Plot of the transition frequency when the magnetic field is shifted from the ZEFOZ field value along one axis by ±4 G, while the field along two other axes are set at the ZEFOZ field value. (b), Two-dimensional spectrum (xy plane) when the field is at the ideal ZEFOZ field. (c), Two-dimensional spectrum (xy plane) when the magnetic field along the z axis is adjusted by 0.5 G.

From the above discussion, even aligning a field with a misalignment of 0.02° is already a technical challenge because the turning points need to be achieved along three orthogonal directions simultaneously. In addition, the field misalignment was required to be much less than 0.02° to get the expected long coherence time in this system. Compared to Fraval's Pr^{3+}:Y_2SiO_5 system [21], this magnetic field alignment was substantially more complicated. In Pr^{3+}:Y_2SiO_5, the fine alignment of the magnetic field was achieved by optimising T_2 directly. This method works because the hyperfine T_2 for the ZEFOZ transition in that system was relatively short, of the order of seconds. For Eu^{3+}:Y_2SiO_5, the

ZEFOZ transition T_2 was expected to be hours (Section2.5.4). The direct T_2 optimisation method was not practical because the system could not be kept stably cold for that long. Furthermore, the ZEFOZ transitions for Pr^{3+}:Y_2SiO_5 happen at reasonably small fields, of the order of a few hundred Gauss, and the magnetic field was provided by a set of superconducting XYZ-coils. With an XYZ-coil, it is easy to adjust the field direction by independently changing the current driving the X, Y or Z coils. However, XYZ-coils cannot reach the $\sim$ 1 T fields required to perform ZEFOZ in Eu^{3+}:Y_2SiO_5. The reason for this is that the huge torque would distort the coils if a very strong magnetic field is applied. As an alternative, an Oxford SM-2000 superconducting magnet, capable of providing stable magnetic fields of up to 15 Tesla along one direction, was used as the source of a DC field.

4.3.2 Introduction to the sample mount

The magnetic field from the superconducting magnet is along a locked Z direction while the ZEFOZ transition happens at a particular field orientation. We designed a special sample mount, capable of rotating the crystal such that the fixed field was aligned along the desired critical point field direction. The sample mount was designed to have the ability to coarsely align the angle easily until a point when a set of two nano-positioning goniometers (from Attocube) could be used. As shown in Figure 4.7, it includes a wedge, a rotation plate and the two goniometers. Because the spin Hamiltonian characterisation determines the C_2 direction much more accurately than the D_1 and D_2 [22], the wedge was designed to align the C_2 axis correctly, while the rotation plate allows the D_1 and D_2 orientation to be coarsely adjusted. Once the field misalignment along all directions came into the range of the Hamiltonian fitting error ($\sim 3°$), the two goniometers were used to perform the fine alignment by using phase sensitive detection. The detail of the coarse and fine alignment will be discussed in the following sections.

4.3.3 Rough alignment of the field

Rough alignment of the field was realized by measuring the hyperfine structure using Raman heterodyne spectroscopy. In Figure 4.8, an example of a measured Raman-heterodyne spectrum is presented, showing how an applied magnetic field results in Zeeman splitting of the $\pm 1/2 \rightarrow \pm 3/2$ transition, which happens at 34.5 MHz at zero field (Section 2.3.2). In order to work out the field orientation, the known Hamiltonian parameters were used to fit the measured spectra. Because the zero-field hyperfine levels are doubly degenerate, in the presence of the external field, each zero-field line should split into four lines. However, in fact, as shown in Figure 4.9 (b), each zero-field line was split into eight lines by the applied field. This is because there are two magnetically inequivalent sites for each crystallographically equivalent Eu^{3+} site [22] (Section 2.3.2). Only transition frequencies of the 'site 1a' are investigated in this thesis. Once the field orientation was determined from the fitting, the sample rod was removed from the magnet, then the orientation between the sample and the wedge was adjusted by rotating the rotation plate. The spectrum was remeasured to work out the updated field orientation. This process was repeated until the fitting showed that the error in the alignment was less than 3°, an offset in the range of the Hamiltonian fitting error. The achieved field at this stage, from the fitting, was within 3° of the direction [-0.535, -0.634, 0.558] in the [D_1, D_2, C_2] coordinate frame.

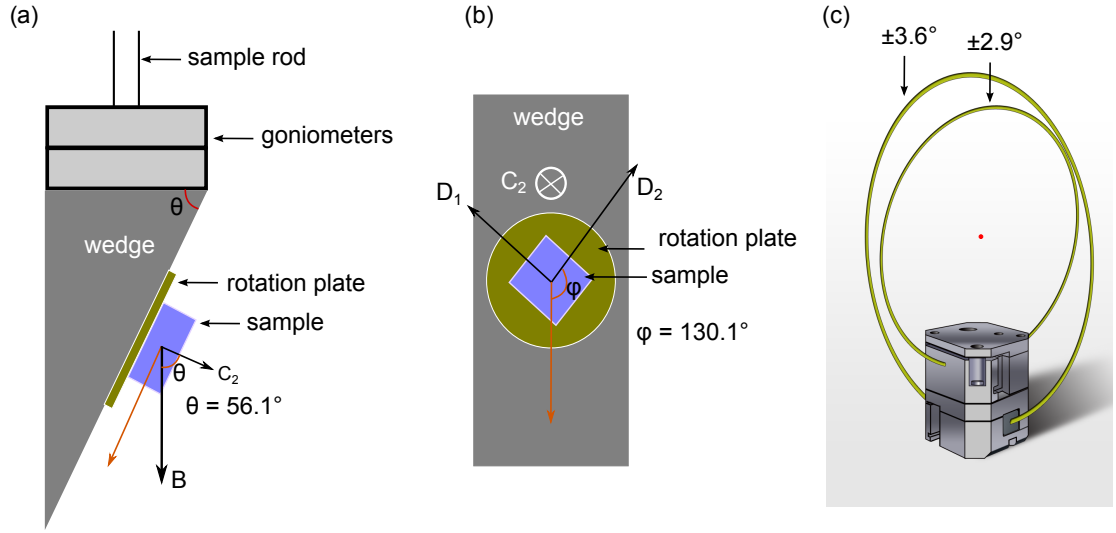

Figure 4.7: Illustration of the sample mount. (a), The sample mount consists of a wedge, a rotation plate and two electrically driven goniometers. The wedge, attached to the bottom goniometer, was designed to align the C_2 axis correctly. (b) The rotation plate was fitted to the wedge with three screws and the sample was glued on the rotation plate in roughly the right orientation in the (D_1, D_2) plane. The orientation of the sample relative to the field could be adjusted by rotating the plate on the wedge. (c), The two goniometers can tilt the sample a small amount along a pair of orthogonal directions by ±3.6° and ±2.9° respectively. The angles θ and ϕ are the theoretical calculated ZEFOZ field orientations relative to the coordinate frame (D_1, D_2, C_2), as demonstrated in Figure 4.2.

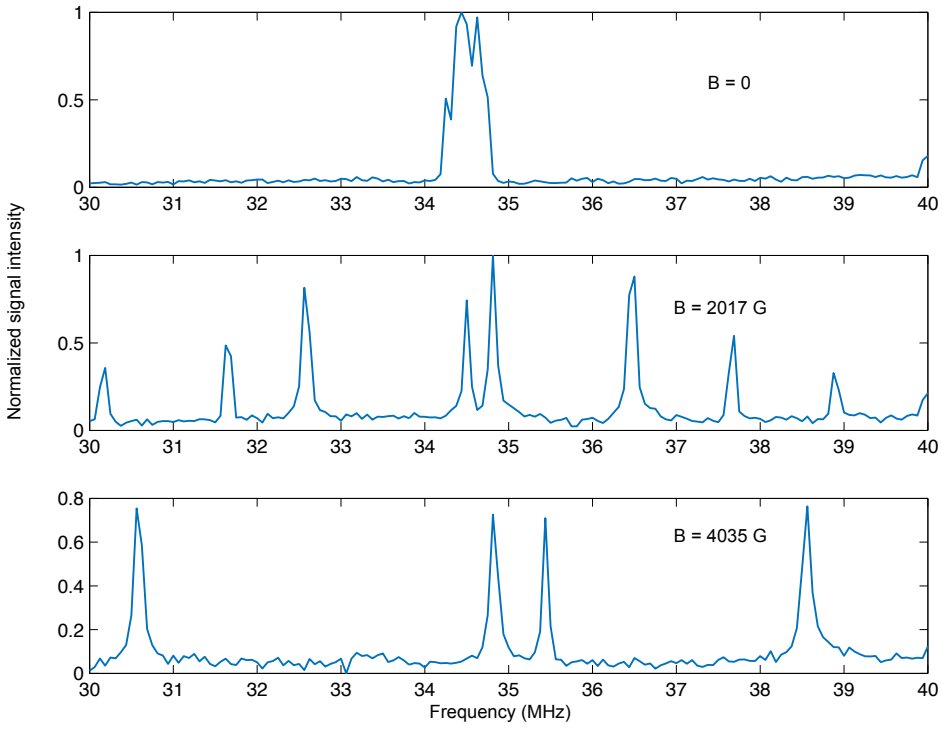

Figure 4.8: An example of the measured Raman-heterodyne spectrum of the $\pm 1/2 \rightarrow \pm 3/2$ transition (34.5 MHz at zero field) in the presence of an applied external magnetic field. Because of the magnet's residual field, the 34.5 MHz transition splits even in the case of '$B = 0$'.

4.3.4 Fine alignment of the field: phase sensitive detection

The final alignment of the sample with respect to the magnetic field was achieved by carrying out phase sensitive detection, which works by applying external magnetic perturbations and measuring the resulting phase shift on the echo signal. The external perturbations, of the order of 10 G, were produced by three sets of coils mounted along three orthogonal directions outside the cryostat.

With these coils, the phase sensitive detection allows a measurement of the field sensitivity of the investigated transition with high accuracy. The field sensitivity was measured by observing the phase shift of a two-pulse Hahn echo that occurred when the perturbation field was reversed after the rephasing π-pulse (see sequence RF_1 in Figure 4.3). This phase shift was observed by mixing the echo signal with two separate local oscillator channels separated in phase by 90° (see Figure 4.4). With the information obtained from the phase sensitive detection, the crystal was reorientated using the goniometers such that the field was better aligned with the critical point. Besides the field alignment, the field magnitude was also adjusted to achieve a smaller field sensitivity of the transition. As the Oxford superconducting magnet has a low field precision of 0.01 T, an external DC offset coil was mounted by winding the wire outside the cryostat. This offset coil is capable of providing a field along the z-axis up to 20 G, with a precision higher than 0.1 G, limited by the current supply.

The method of phase sensitive detection can be illustrated by using the Bloch sphere as shown in Figure 4.10. A driving RF $\pi/2$-pulse rotates the Bloch vector of the ensemble to the y axis (marked as M_0). After some time for precessing, a π-pulse inverts the y-

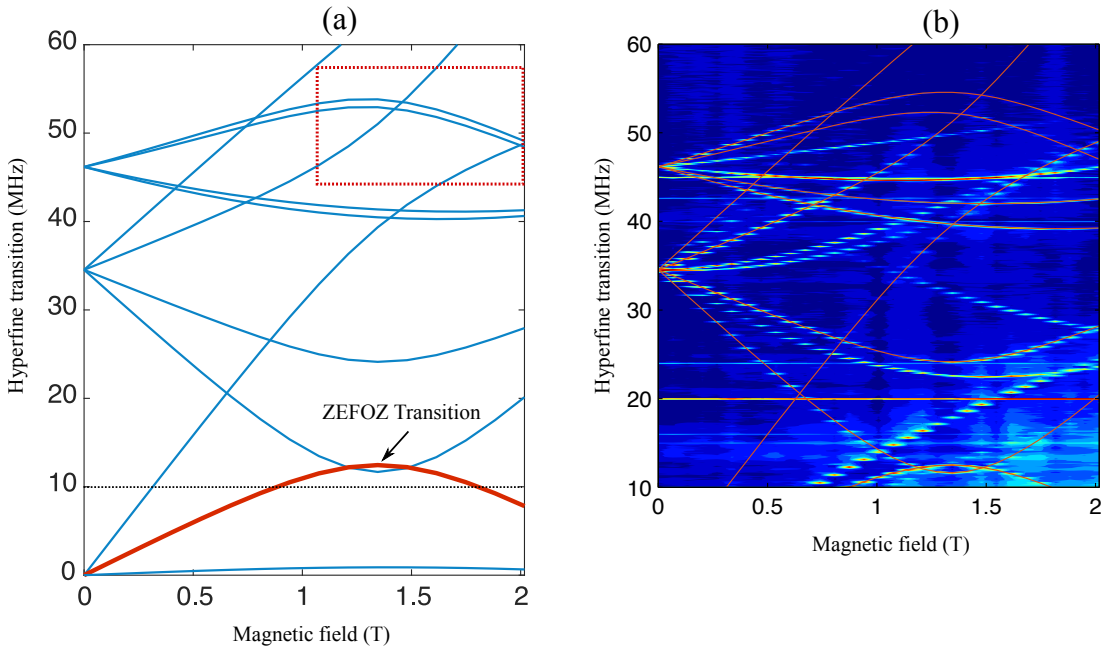

Figure 4.9: Zeeman splitting of the hyperfine ground state in the presence of an external field. The figure was plotted with the transition frequencies vs. the field magnitude. (a), The calculated transition lines as the magnetic field increased along the ideal ZEFOZ field orientation. (b), The measured hyperfine spectra as a function of the field. Each vertical slice is one spectrum with colour indicating the intensity of the Raman heterodyne signal. The fitting on the lines of magnetically 'site 1a', shown as solid red lines, demonstrates that the field orientation for this spectrum is about 4° off the optimal ZEFOZ field direction. This 4° misalignment results in a difference in the measured spectrum from a spectrum for the theoretically ideal ZEFOZ field as indicated in the dotted red rectangle.

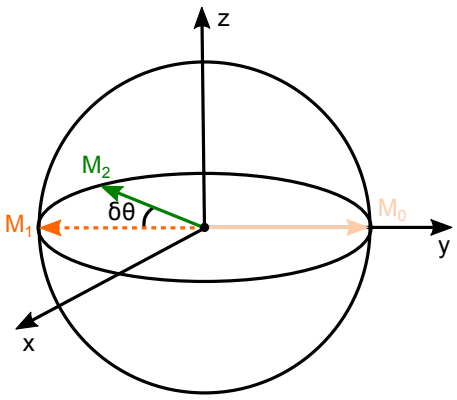

Figure 4.10: Illustration of phase sensitive detection using the Bloch sphere. 'M_0' is the ensemble Bloch vector of the transition after a $\pi/2$ pulse and 'M_1' is where the rephased Bloch vectors of the ensemble are supposed to focus some time after the π-pulse (echo). However, when the polarity of the DC perturbation field $\boldsymbol{\delta B}$ is reversed prior to the echo detection period (RF_1 in Figure 4.3), the resonant frequency of the transition would be shifted. This causes the rephased ensemble Bloch vector to shift by $\delta\theta$ and focus at M_2. With a fixed $\boldsymbol{\delta B}$, $\delta\theta$ is a measurement of the field sensitivity of the transition.

component of the vector and the polarization of the ensemble is supposed to refocus at the $-y$ axis (marked as M_1). With a sudden perturbation (applied by reversing the polarity of the perturbing magnetic field) prior to the echo detection period (RF_1 in Figure 4.3), the frequency of the transition is shifted by $\delta\omega$. This causes the ensemble Bloch vector to refocu at a different position (marked as M_2) with a phase shifted by $\delta\theta$ relative to M_1. The phase shift $\delta\theta$ is dependent on the frequency shift $\delta\omega$ and the total evolution time τ,

$$\delta\theta = \delta\omega\tau, \tag{4.1}$$

where the frequency shift $\delta\omega$ is given by the field sensitivity $\boldsymbol{S_1}$ and the strength of the applied field perturbation $\boldsymbol{\delta B}$ [1]:

$$\delta\omega = 2\pi(\boldsymbol{S_1} \cdot \boldsymbol{\delta B}).$$

From the above equations, with a fixed delay τ and $\boldsymbol{\delta B}$, the measured phase shift $\delta\theta$ is a measure of the field sensitivity $\boldsymbol{S_1}$.

By iteratively measuring the field sensitivity, adjusting the field magnitude and tilting the sample with the goniometers, the first-order Zeeman coefficient $|\boldsymbol{S_1}|$ was reduced to be below 1×10^{-3} MHz/T. This alignment was achieved at a field magnitude of 1.29 ± 0.01 T. As discussed before, this uncertainty of 0.01 T is determined by the precision of the main superconducting magnet while the field during the alignment can be changed with much higher precision given by offset DC coil. From the measured field sensitivity $|\boldsymbol{S_1}| = 1 \times 10^{-3}$ MHz/T, the field misalignment is less than 0.004° from the ideal critical point field orientation. This alignment is labelled as $\boldsymbol{B_{cp}}$, for which a decoherence rate of 2.9×10^{-2} s^{-1} is expected based on the measured $\boldsymbol{S_1}$ according to Equation 2.12.

During the field alignment, one issue with those external perturbation coils is that while the field produced by the two sets of the horizontal coils (orthogonal to the superconducting magnet) is the same as that was expected, the field produced by the vertical coils was along the opposite direction to that expected. This is because when the perturbation field was applied parallel with the superconducting magnet the magnet acts to maintain the flux through the coil. In this experiment, this results in a change in the total field in the opposite direction to the applied perturbation field. This also makes it hard to evaluate accurately the changed value of the magnetic field. Because the DC offset coil also provides a field parallel with the superconducting magnet, it has the same problem as the vertical perturbation coil.

4.4 Results

4.4.1 Two pulse spin echo decay

Once the field was well aligned to $\boldsymbol{B_{cp}}$, two pulse spin echoes were used to measure the coherence time. The measured decay of the two-pulse spin echoes as a function of the delay τ is shown in Figure 4.11. Three data sets are presented corresponding to the fields $|B_{cp}|$, $(|B_{cp}| + 0.005$ T) and $(|B_{cp}| + 0.05$ T). These show a dramatic decrease in the echo decay rate as the field alignment brings the transition closer to the critical point. The

[1] Only the first-order field sensitivity is considered here.

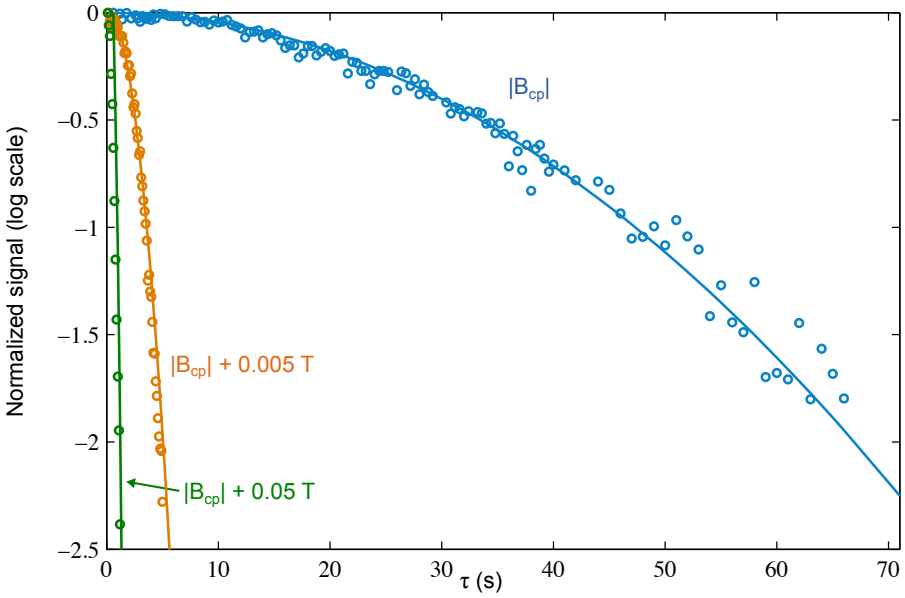

Figure 4.11: Two pulse spin echo decay with the echo amplitude E plotted against the total delay τ. Open circles show echo decays at magnetic fields $|B_{cp}|$ (blue), $(|B_{cp}| + 0.005)$ (orange) and $(|B_{cp}| + 0.05)$ T (green) as labelled. Each set is fitted using Equation 3.21 with phase memory times T_M equal to 47 s, 3.5 s and 0.8 s respectively.

echo decay curve at B_{cp} has a non-exponential form and cannot be properly described by a standard relaxation time T_2 because the decoherence rate changes with delay time τ. The decay is accurately described by Equation 3.21:

$$E(\tau) \propto \exp\left[-(\tau/T_M)^2\right], \tag{4.2}$$

which incorporates decoherence due to spectral diffusion (see Section 3.1.3). In this model, E is the echo amplitude as a function of τ. The phase memory time T_M is used to describe the coherence decay of the system. This was determined to be 47 s at B_{cp}.

For $\tau \ll T_M$ the decoherence rate, given by $2\tau/{T_M}^2$ (the gradient of the echo decay), is extremely slow. For example, at $\tau = 100$ ms, the fit to Equation 4.2 predicted the decoherence rate to be 9.1×10^{-5} s^{-1} , which is significantly slower than the rate of 4.4×10^{-3} s^{-1} for a perfect field alignment predicted by equation 2.12, and here the field was not perfectly aligned. This is attributed to the reduced local spin-reconfiguring rate due to the frozen core induced by the applied magnetic field (Section 2.5.3).

Compared to the ZEFOZ transition in Pr^{3+}:Y_2SiO_5 [21], the frozen core effect in Eu^{3+}:Y_2SiO_5 is much stronger. This is because the induced magnetic moment in that system was more than an order of magnitude smaller than that in the current experiment. For example, in Pr^{3+}:Y_2SiO_5, at the 0.1 T critical point studied in [21], the Pr^{3+} ions possessed a magnetic moment of 600 Hz/G. However, in Eu^{3+}:Y_2SiO_5, due to the induced component, the total magnetic moment of the Eu^{3+} ion at the investigated critical point (1.35 T) is 15.5 kHz/G as shown in Figure 2.12.

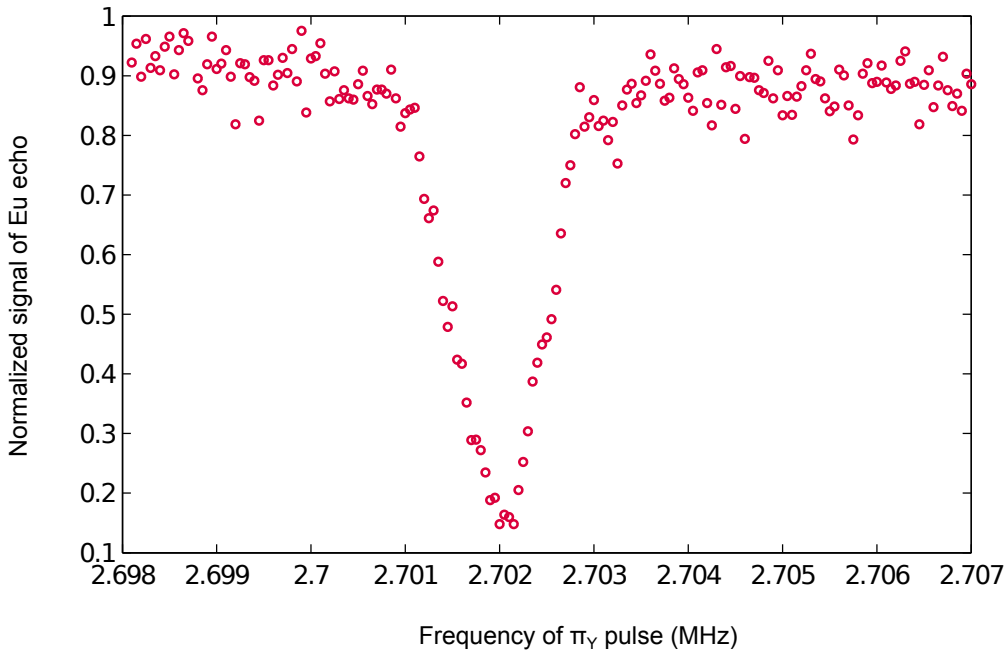

Figure 4.12: The Eu^{3+} two pulse spin echo amplitude plotted against the frequency of an applied π-pulse driving the Y^{3+} spin transition. This data set was measured at a magnetic field which was detuned by 10 G from $\boldsymbol{B_{cp}}$, so that the Eu^{3+} transition was more sensitive to the perturbation caused by the π_Y-pulse.

4.4.2 Investigation on the frozen core

The effect of the frozen-core Y spins was investigated by intentionally 'thawing' the core during the echo using pulse sequence RF_2 shown in Figure 4.3. A π-pulse resonant with the Y Zeeman splitting at 2.7 MHz (π_Y pulse) was applied just before the Eu π-pulse. The optimal frequency of the π_Y pulse was achieved through minimising the Eu echo size, at a fixed delay τ, by scanning the yttrium frequency (Figure 4.12). The π_Y pulse aims to invert the Y spins to maximize their contribution to the decoherence rate. The observed increase in decoherence rate is shown in Figure 4.13. If the inversion of the frozen-core was complete, the echo decay should have become exponential. The non-exponential decay for $\tau < 10$ s is attributed to the fact that the π_Y-pulse possessed an insufficient bandwidth (200 Hz) to achieve total inversion of the inhomogeneously broadened Y^{3+} spins and hence, could not maximally perturb the Eu^{3+} ions. Rather, the perturbing pulses were tuned to be resonant with the frozen core Y spins with the lowest flipping rate. For $\tau > 10$ s, the frozen core had completely thawed and the Hahn echo decay was exponential. The decoherence rate of the exponential decay is 5.3×10^{-2} s^{-1}, which is within a factor of two of the predicted decoherence rate (2.9×10^{-2} s^{-1}) from the directly measured transition sensitivity. This confirms that the decoherence at $B_{\boldsymbol{cp}}$ is still dominated by the interaction between the Eu^{3+} ions and the Y spin bath. Hence, Mims' model of Equation 4.2 allows T_M to be related to the flipping rate R of the local Y spins and $\Delta\omega_{1/2}$, the half width of the spectral broadening on the Eu hyperfine transition due to the distribution of the

static local field [85] (Section 3.1.3):

$$T_M = 1.41(R\Delta\omega_{1/2})^{-1/2} \tag{4.3}$$

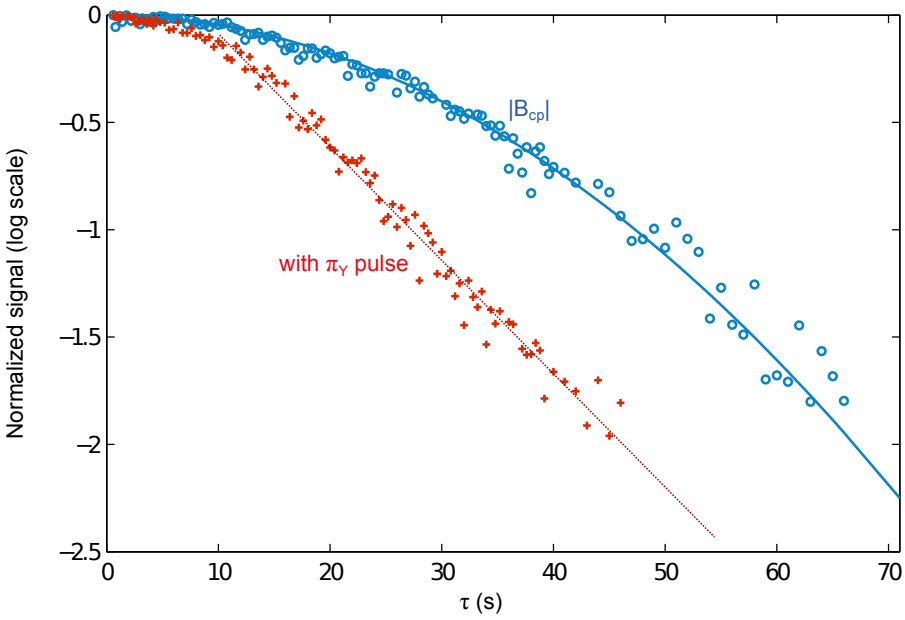

Figure 4.13: Comparison of the echo decays at $|B_{cp}|$ with and without a perturbing π_Y-pulse. Open circles show two pulse spin echo decay at magnetic fields $|B_{cp}|$ (blue). '+' symbols show the two-pulse spin echo decay with the perturbing π_Y-pulse (sequence RF_2 in Figure 4.3). At $\tau > 10$ s, the decoherence rate is 5.3×10^{-2} s^{-1} from an exponential fit to the 'π_Y' data set.

When the frozen core has been removed, the decoherence rate (5.3×10^{-2} s^{-1}) is a measure of the half width $\Delta\omega_{1/2}$ ($\Delta\omega_{1/2} = \pi\Delta f = 1/T_2$). Therefore, from Equation 4.3, the spin flip rate of the frozen core Y spins is $R = 1.7 \times 10^{-2}$ s^{-1}. This corresponds to a correlation time of 59 s for the transition frequency fluctuations, which is four orders of magnitude longer than the low field value of 3.5 ms measured by Arcangeli et al.[104].

4.4.3 Dynamic decoherence control (DDC) results

Owing to the very small amount of decoherence, the signal to noise ratio of the two-pulse spin echo measurements shown in Figure 4.11 was not sufficient to accurately measure the decoherence for $\tau \ll T_M$. Therefore, DDC pulse sequences, as introduced in Section 3.1.4, were used, which allow measurements of the decoherence rate at 100 ms$< \tau <$10,000 ms, as well as allowing extension of the slow decoherence rates at this short time zone to longer evolution times.

Ideally, application of a DDC sequence with a pulse interval τ_c would result in a hyperfine decoherence rate equal to the gradient of the two pulse spin echo curve at $\tau = \tau_c$, namely the tangent (Figure 4.14) [92]. According to the Equation 4.2, the expected coherence time T_2 from a DDC measurement, given by the tangent of the theoretical fitting

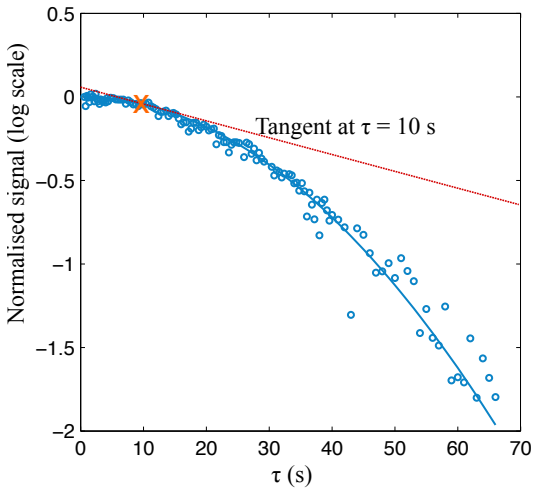

Figure 4.14: An illustration of the tangent of the two pulse spin echo decay at $\mathbf{B_{cp}}$.

for the two pulse spin echo decay curve is written:

$$T_2(\tau_c) = \frac{T_M^2}{2\tau_c}, \tag{4.4}$$

where the phase memory time T_M at $\mathbf{B_{cp}}$ was determined to be 47 s.

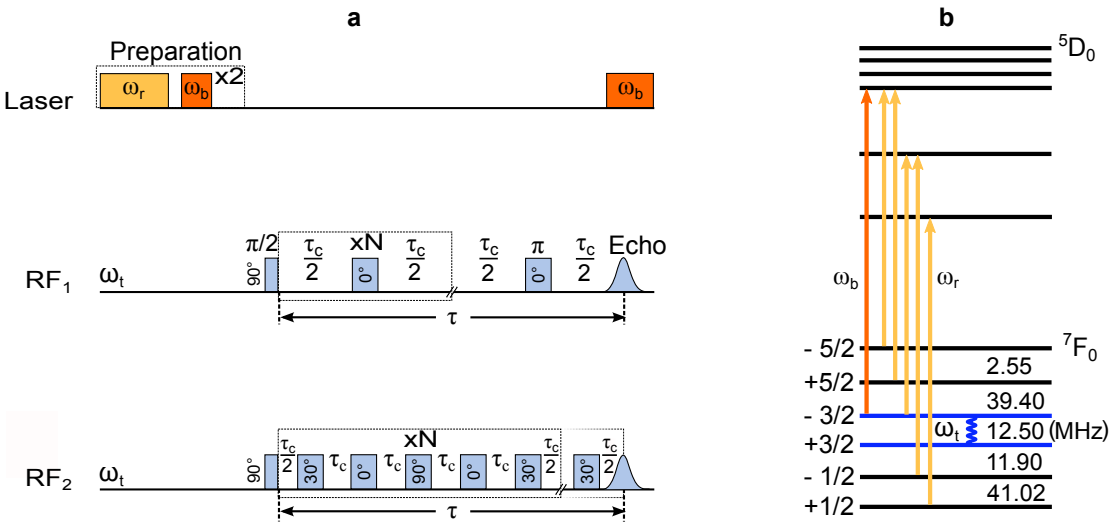

Figure 4.15: (a), DDC pulse sequence used in the experiment. RF_1 is the CPMG pulse sequence. RF_2 is the KDD_x pulse sequence. The laser pulses and the hyperfine transition frequencies in (b) are identical to what was used in the two pulse spin echo measurement as illustrated in Figure 4.3.

The first DDC pulse sequence used was a CPMG pulse sequence (RF_1 in Figure 4.15), which provides a simple way to test the DDC effectiveness. The main results of the CPMG measurement are shown in Figure 4.16. The echo decays exponentially against the total evolution time and the coherence time was prolonged as the time τ_c between the π-pulses was decreased. In Table 4.1, I list the coherence times measured with a CPMG pulse sequence and the estimated value from the gradient of the two-pulse spin echo curve. The

decoherence rates measured by the CPMG pulse sequence are in good agreement with the gradient of the Hahn echo decay curve with a discrepancy within 15% for $\tau_c < 1000$ ms. For DDC measurements, a realignment of the field was required after finishing collecting each data set. Hence, the slightly longer coherence time of the CPMG results than those from the Hahn echo decay curve for $\tau_c \geq 1000$ ms is probably due to better alignments.

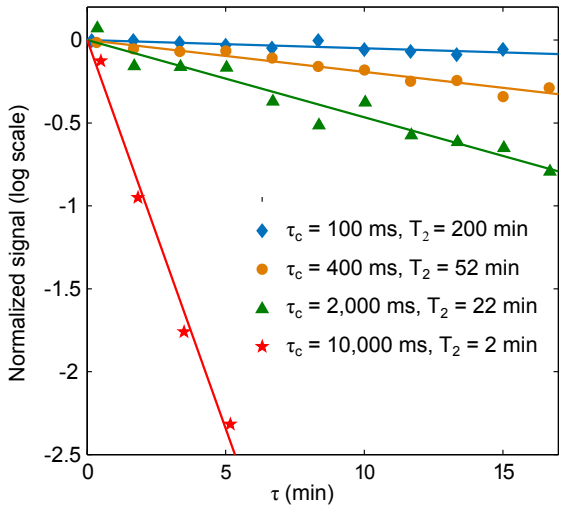

Figure 4.16: Measured coherence times at $\mathbf{B_{cp}}$ with a CPMG pulse sequence. Four data sets are displayed, with the echo amplitude E plotted against the total delay τ, corresponding to different pulse intervals τ_c.

Table 4.1: Expected coherence times calculated from the tangent of the two pulse spin echo decay compared to the experimental measurements with a CPMG sequence for different pulse rates.

τ_c (ms)	Expected value (min)	CPMG (min)
100	184.0	200.0 ± 50.0
200	92.0	80.4 ± 20.0
400	46.0	52.0 ± 5.0
1,000	18.4	32.3 ± 5
2,000	9.2	22.0 ± 2.0
10,000	1.8	12.1 ± 0.5

Although the CPMG sequence is commonly used to extend coherence, the method is only effective in preserving quantum states that possess a particular phase. Hence, it is not suitable for use in a practical quantum memory, which is required to store arbitrary quantum states. As an example, the coherence time of 200 min, achieved with CPMG decreased to less than 10 s when the phase of the initial $\pi/2$-pulse was rotated by 90°.

To test the suitability of the Eu^{3+}:Y_2SiO_5 system for arbitrary quantum state storage, a further experiment was performed using a DDC sequence known as KDD_x (RF_2 in Figure 4.15). The KDD_x sequence is effective in preserving arbitrary states and is robust against errors due to pulse area and off-resonant excitation [102].

The KDD_x results are shown in Figure 4.17. A coherence time of 370±60 min (6±1 hours) was observed for a decoupling period τ_c of 100 ms. This slightly longer coherence

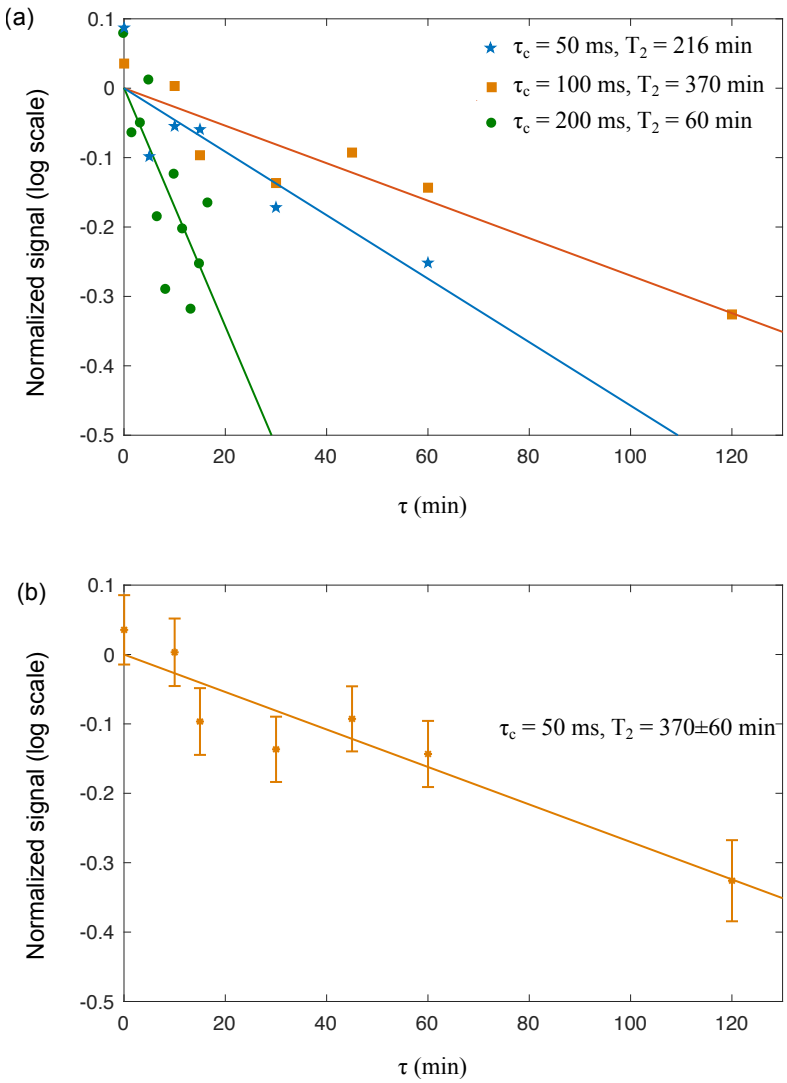

Figure 4.17: Measured coherence times with KDD_x pulse sequences. The figures present the echo amplitude plotted against the total delay. (a), Three data sets corresponding to DDC pulse intervals τ_c of 50 ms, 100 ms and 200 ms. (b), A repeat of the long coherence time data set with error bars for $\tau_c = 100$ ms. The error bars correspond to the shot-to-shot variations in the echo amplitude due to the preparation sequence that were observed at short delays. The uncertainty in the calculated T_2 is obtained from the uncertainty in the linear fit.

time compared to the result of the CPMG experiment is attributed to the day-to-day alignment variation of the magnetic field on the order of 0.001°.

When using DDC, decreasing τ_c should increase the coherence time until τ_c is shorter than the time scale of the dominant decoherence mechanism at which point no further improvement is seen. Such a trend was observed for both the CPMG and KDD_x sequences for 100 ms< τ <10000 ms. However, we observed a decrease in coherence time when τ_c was decreased from 100 ms to 50 ms when using the KDD_x sequence even though the bulk Y flipping rate is 3.5 ms. This is because the electrical mains supply has a frequency of 50 Hz and no particular effort was made to shield the crystal from AC magnetic fields. For τ_c = 100 ms, 50 Hz fluctuations are rephased because 100 ms is an integer multiple of the 20 ms period of the mains supply. In contrast, for τ_c = 50 ms, the transition is maximally sensitive to mains pick-up because 50 ms is a half-integer multiple of the supply period. In spite of this, even in the absence of magnetic shielding, the insensitivity of the transition to magnetic fluctuations still allowed a coherence time of 216 min to be achieved for τ_c = 50 ms.

4.5 Discussion

The application of the critical point field allowed a phase memory time of 47 s to be achieved on the $3/2 \leftrightarrow -3/2$ hyperfine transition of $^{151}Eu^{3+}$:Y_2SiO_5. This resulted from the combination of two effects. The first effect was the reduction of the transition's sensitivity to magnetic perturbations to the order of 1×10^{-3} MHz/T. The second effect was the reduction in the Y spin flipping rate by four orders of magnitude to R= 1.7×10^{-2} s^{-1} due to the formation of a frozen core. The consistency of the experimental results with Mims' model for decoherence in the presence of slow spectral diffusion is strong evidence that the Y spin bath fluctuations remain the dominant decoherence mechanism. Hence, a further decrease in the decoherence rate could be achieved by improving the decoupling of the Y-spin bath from the Eu ion.

Equation 2.12 predicts that the coherence time could be improved by an order of magnitude by improving the alignment of the applied field such that $|\boldsymbol{S_1}| = 0$. However, the current alignment is already close to the limit imposed by the ensemble inhomogeneity. Each ion possesses a slightly different critical point magnetic field so they cannot be aligned accurately simultaneously. This is mainly due to the strain broadening of the hyperfine transitions, which was measured to be 10 kHz at zero field. The crystal field broadens the transition via the quadrupole moment tensor $\boldsymbol{Q}$, which is comprised of two parameters E and D (Section 2.3). If we use a simple model where we consider the quadrupole inhomogeneity as the only source of the hyperfine inhomogeneous broadening and presume that there is no correlation between the two quadrupole splittings at zero field (34.5 MHz and 46.2 MHz), we can calculate the inhomogeneity at the critical point field. As shown in Figure 4.18(a), this can be done by sampling a frequency pair '(f_1,f_2)' from the frequency distributions of the two transitions decided by the linewidth Δf, then calculating the new quadrupole parameters E and D which would gives these frequencies. E and D can then be used to calculate the critical point of that ion. The distribution of the critical points in Figure 4.18(b) is a result after sampling through the transition broadening 10000 times. The measured 10 kHz linewidth for the hyperfine transitions results in a critical field inhomogeneity of 4 G. This means that, while we align one subgroup of the Eu^{3+} ions at their critical field, some subgroups would still be off their critical point by 4 G, corresponding to a decoherence rate of 0.25 s^{-1} or T_2 = 4 s according to equation 2.12

(The frozen core effect is not included in this model). Repeating the calculation by setting the linewidth Δf to be 5 kHz and 1 kHz leads to a reduced critical field broadening of 2 G and 0.5 G respectively. A field detuninig of 0.5 G from the critical point corresponds to 0.03 s^{-1}. That is to say, a decrease of the quadrupole inhomogeneity by an order of magnitude could leads to an increase of the coherence time by an order of magnitude.

The quadrupole broadening is due to the strain broadening within the crystal, which is not intrinsic to the site and can be reduced by improving the crystal growth process. A reduction in strain broadening by over an order of magnitude has been achieved in analogous materials [105] through reducing the dopant concentration and using isotopically pure materials. In Eu^{3+}:Y_2SiO_5, the strain broadening was also demonstrated to be dependent on the Eu^{3+} concentration where an increase in Eu^{3+} concentration from 0.02% to 7% produced an increase in the inhomogeneous linewidth from 0.5 GHz to 150 GHz(reference [17]). Repeated annealing of the crystal has demonstrated a reduction in optical linewidth from 2.4 GHz to 0.5 GHz for Eu^{3+}:Y_2SiO_5 (reference [106]). Though all these inhomogeneous linewidth observations were for optical transitions, we would expect a similar reduction in hyperfine linewidth at the critical point if the quadrupole inhomogeneity is the main source of broadening.

Refining the crystal growth technique is a long term procedure, but an immediately feasible strategy for tackling the inhomogeneous broadening is creating a narrow feature inside the hyperfine broadening through the spectral holeburning. Figure 4.19 presents a simple technique for creating a narrow feature such that the RF pulse sequence talks to a frequency-selected subgroup of Eu^{3+} ions.

A reduced linewidth of the transition would also improve the effectiveness of DDC. The coherence time of 6 hours was obtained with a reasonably low pulse rate. An increased pulse rate is expected to extend the coherence time. However, as stated before, a reduction of the coherence time was observed by increasing the decoupling rate from 10 Hz to 20 Hz ($\tau_c = 50$ ms) when using the KDD_x sequence. Though this is mainly due to the detected noise of 50 Hz from the electrical mains supply, pulse errors can also contribute to decreased coherence times with higher decoupling rates. A higher decoupling rate means a larger number of DDC pulses, thus the pulse errors become increasingly important.

The inhomogeneous linewidth of the transition is one of the sources of DDC pulse errors. The inhomogeneous linewidth causes different subgroups in the ensemble to respond differently to the DDC pulses and leads to errors in the rephasing process. Ideally, we want the DDC pulses to have the same action on every individual ion in the ensemble. This would require the bandwidth of the pulse to be much greater than the inhomogeneous linewidth of the ions. However, the bandwidth of the applied RF pulse is often limited by the feasible RF power. An alternative is to reduce the inhomogeneous linewith, either by refining the crystal growth process or by preparing a narrow feature of the transition by using spectral holeburning as discussed above.

The other source of DDC pulse errors is the inhomogeneity in the RF intensity across the sample arising from imperfect design and positioning of the RF coils. As shown in Figure 4.20, those ions in the centre of the coil ('M' ions) experience a stronger RF field while those at the sides ('N' ions) of the coil experience a weaker RF field. For a fixed pulse duration, the pulse area, which is the product of the Rabi frequency(proportional to the RF amplitude) with the pulse duration, will be different for atoms at 'M' ions and 'N' ions. Hence there will be errors in pulse area for some subgroups of the ensemble. Inhomogeneity in RF intensity can be reduced by either using thinner samples or designing a better RF coil.

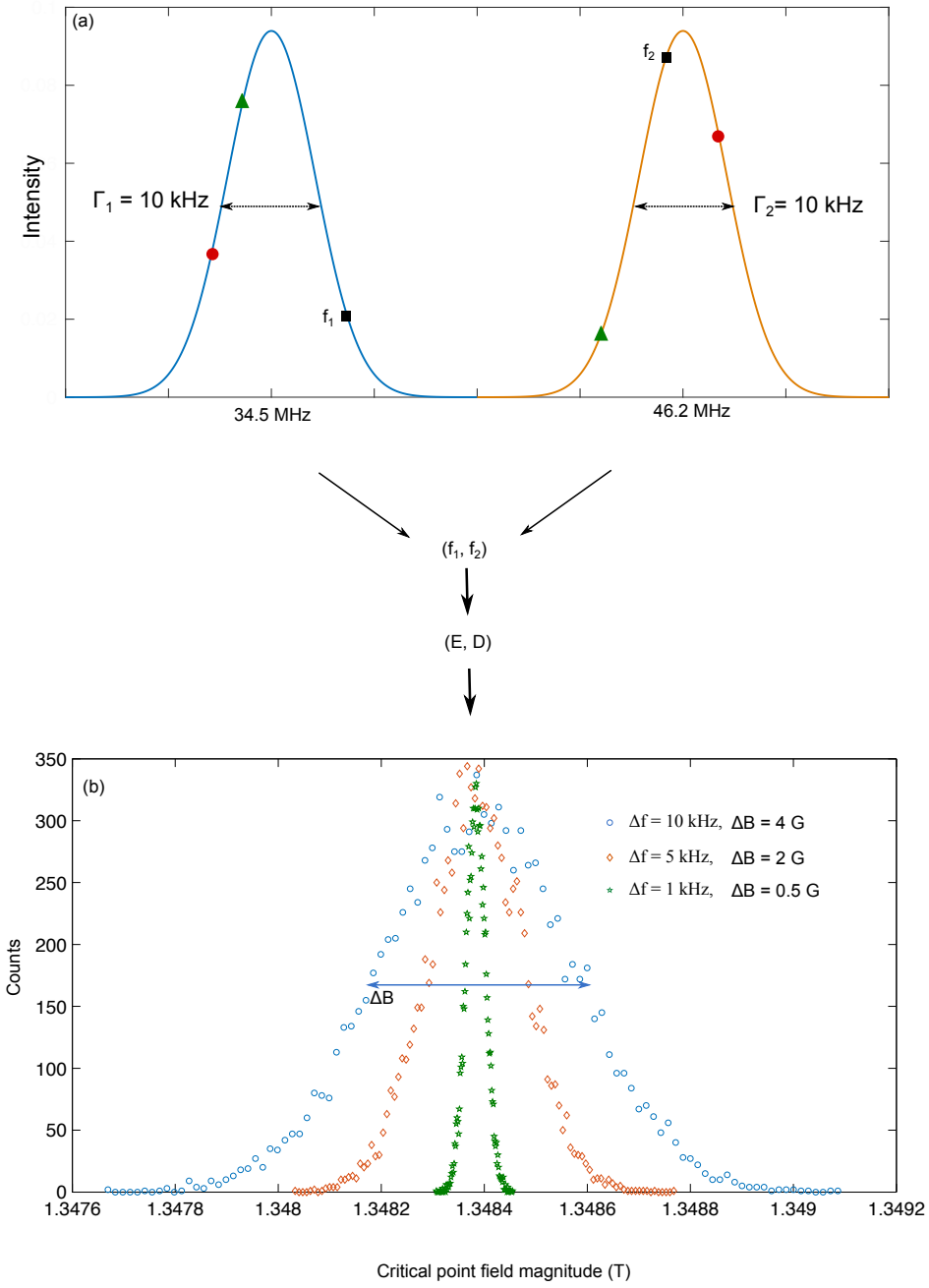

Figure 4.18: Illustration of the calculation of the inhomogeneity of the critical point field due to the quadrupole inhomogeneity. (a), Based on the hyperfine inhomeneous linewidth, Gaussian distributions corresponding to the broadening of the two zero-field transitions (34.5 MHz and 46.2 MHz) were formed. Pairs of frequency (f_1,f_2) were sampled randomly from the two distributions, with which the parameters E and D, which forms the quadrupole $\boldsymbol{Q}$ tensor, can be calculated. With the formed $\boldsymbol{Q}$ tensor and the other known Hamiltonian parameters, the critical point field investigated was calculated. (b), The inhomogeneity in the critical point magnitude calculated from randomly sampling the frequency through the two distributions for 10000 times. Three data sets are shown, corresponding to different linewidths of 10 kHz, 5 kHz and 1 kHz. This simulation is based on two assumptions. One is that the quadrupole inhomogeneity is the only source of the transition's inhomogeneous broadening. The other is that there are no correlations between the two zero-field transitions.

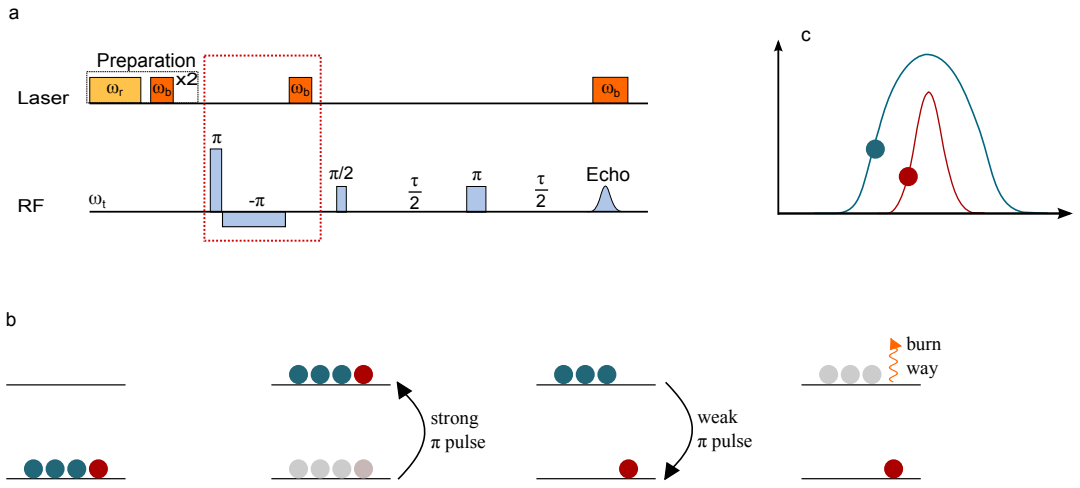

Figure 4.19: Achieving long coherence times by creating a a narrow feature in the hyperfine transition using spectral holeburning. (a), The pulse sequence used. A coherence measurement using the two pulse spin echo pulse sequence is performed after creating a narrow feature in the inhomogeneous line of the transition. The narrow feature is created using spectral holeburning by applying the pulses in the dotted red rectangle. (b), Illustration of the process of creating the narrow feature. Because of the optical preparation, all the ions are initialised in the ground state and are driven to the excited state by a strong and short RF π-pulse. A long and weak RF pulse is then applied, which drives only the ions with near zero detuning, represented with red circles, back to the ground state. Those off-resonant ions remaining in the excited state, represented with green circles, are burned away by an optical burning pulse at ω_b. This creates a narrow feature in the inhomogeneous line as shown in (c). In (c), the red line with red ions represents the narrow feature created and the blue lines with blue ions represents the inhomogeneous broadening.

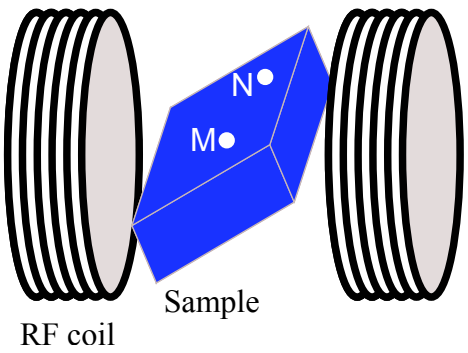

Figure 4.20: Illustration of RF inhomogeneity. Ions at M and N are on the path of the laser, which means they will contribute to the signal. If the coils are not perfectly implemented, there will be a difference in RF intensity between M and N.

Even without using any of the above approaches, the coherence time could be extended by moving to a critical point with a lower $|\boldsymbol{S_2}|$. There are many critical points that occur for ground state transitions in $^{151}Eu^{3+}$:Y_2SiO_5, and a number of these have slightly smaller values of $|\boldsymbol{S_2}|$ than the point studied in this thesis. In addition, the $|\boldsymbol{S_2}|$ values for critical points in $^{153}Eu^{3+}$:Y_2SiO_5, the other naturally occurring Eu isotope, are smaller still by approximately a factor of two. Furthermore, many of these critical points occur at magnetic field values up to five times larger than the field applied in this work. By increasing the magnetic field, the increased magnetic moment induced on the Eu^{3+} ion would extend the volume of the frozen core. The direct benefit would be a reduction of the Y spin flip rate R, which significantly reduces the rate at which DDC rephasing pulses would need to be applied. While the bulk Y spin flips remain the dominant decoherence mechanism, these refinements of the ZEFOZ technique would allow advances towards the lifetime limit of 23 days in this material [17].

4.6 Summary

In this chapter, the ZEFOZ method was used to extend the hyperfine coherence time in Eu^{3+}:Y_2SiO_5. The critical point investigated occurs at a field magnitude of 1.35 T and has a maximum curvature of $\boldsymbol{S_2} = 21.7$ MHz/T^2 from the theoretical calculation. For a perfect field alignment, the expected coherence time is 229 s, corresponding to a decoherence rate of 4.4×10^{-3} s^{-1}.

The major challenge of the ZEFOZ method is to align the magnetic field, especially when the field source, provided by a superconducting magnet, is along a fixed direction. Good alignment was achieved using applied field perturbation to performing the phase sensitive detection. The best field alignment achieved had a misalignment within 0.004° from the ideal critical point direction. The aligned critical point was found to occur at a field magnitude of 1.29 T.

Once the field was aligned, a two pulse spin echo pulse sequence was used to measure the hyperfine coherence time. The recorded echo decay had a non exponential shape which could be perfectly fitted by the spectral diffusion model of Equation 3.21. From the fitting, the phase memory time T_M was determined to be 47 s.

Because of the non-exponential shape, at short delays, the echo decay rate is much slower than the rate given by T_M. For example, at a delay of 100 ms, the fit predicts a decoherence rate of 9.1×10^{-5} s^{-1}, which is two orders of magnitude slower than the predicted rate for a perfect field alignment presented above. This is due to the frozen core induced on the Eu^{3+} by the applied strong magnetic field, which largely suppressed the spin flipping of the Y^{3+} ions in the host.

The frozen core effect was investigated using a π_Y pulse to intentionally flip the Y^{3+} and thaw the core. An increased echo decay rate of 5.3×10^{-2} s^{-1} was observed when the frozen core was removed. This measurement allowed the frozen core Y^{3+} spin lifetime to be estimated to be 59 s. This number is four orders magnitude longer than that of the bulk Y^{3+} ions.

The slow decoherence rates of the two pulse spin echoes at short delays were measured and extended to longer delays by using DDC pulse sequences. With a pulse interval of 100 ms, the KDD$_x$ pulse sequence resulted in a coherence time of 370±60 min, which is the longest coherence time observed in a solid state system.

The achieved 6 hour coherence time is the combined result of ZEFOZ, frozen core and DDC. However, the achieved phase memory time of 47 s is much shorter than the predicted

coherence time of 229 s for a ideal ZEFOZ transition. This is believed to be because the field was not perfectly aligned due to the limitation imposed by the inhomogeneity of the critical field values in the ensemble. Such an inhomogeneity issue could be improved by using samples with narrower inhomogeneous broadening, creating narrow features by spectral holeburning and designing a better RF coil. Even without using any of these approaches, the coherence time could be extended by moving to a critical point with a lower $\boldsymbol{S_2}$ and higher field magnitude.

The non-exponential spin echo decay shape and the investigation on the frozen core shows that the hyperfine coherence time in Eu^{3+}:Y_2SiO_5 is still limited by the spin-reconfiguration of the Y^{3+} ions in the host. Hence, in the next chapter, the study focuses on the dynamics of these spins.

Chapter 5

Dynamics of the frozen-core Y^{3+} spins in Eu^{3+}:Y_2SiO_5

The study in the previous chapter showed that spin flips of the frozen-core Y^{3+} nuclei in the host is the dominant decoherence mechanism for ZEFOZ hyperfine transitions in Eu^{3+}:Y_2SiO_5. The goal of this chapter is to study the dynamics of these frozen-core Y^{3+} spins, with the aim of achieving longer coherence times through better control of the spins.

The Y^{3+} dynamics are studied in this chapter by perturbing the frozen-core Y^{3+} spins and measuring the effect on the Eu^{3+} ion. The main difference with the method used in Section 4.4.2 is that here the Y^{3+} ions are excited with narrowband pulses so that individual Y^{3+} sites in the frozen core can be addressed. The pulse sequence used to achieve this is shown in Figure 5.1.

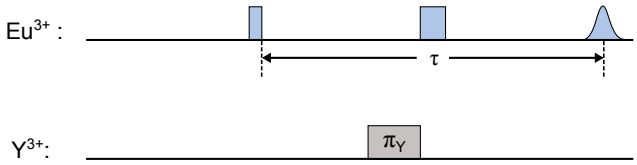

Figure 5.1: The RF pulse sequence used in this chapter. All the optical preparation and readout processes are identical to those discussed in the previous chapter and are not shown here. During the two pulse spin echo of Eu^{3+}, a π_Y pulse was applied prior to the Eu^{3+} π pulse and the effect on the echo amplitude was observed. The π_Y pulse is resonant with the spin transition of one frozen-core Y^{3+} ion.

In this chapter, I first present an introduction to the theory of the interactions between the Eu^{3+} and Y^{3+} ions. This is followed by a measurement of the resonant frequencies of the frozen-core Y^{3+} spins. Then a measurement of the Rabi frequencies of the Y^{3+} ions is presented, which is followed by a presentation of a coherence time measurement on one particular individual frozen-core Y^{3+}. Finally, I also present a measurement of the frequency shift of the Eu^{3+} hyperfine transition when the Y^{3+} spin is flipped.

5.1 Introduction: interactions between the Eu^{3+} and Y^{3+} ions

The study presented in this chapter aims to resolve the dynamics of individual frozen-core Y^{3+} ions. It includes measurements of the resonant frequencies of the Y^{3+} spins and the

frequency shift of the Eu^{3+} hyperfine transition when a Y^{3+} spin is flipped. The results of both measurements are dependent on the magnetic dipole-dipole interactions between the Eu^{3+} and Y^{3+} ions. Hence, before presenting the measurements, in this section, a theory on how these interactions relate to each measurement is introduced.

In this theory, the magnetic dipole-dipole interactions between the Eu^{3+} and the Y^{3+} ions are treated as a perturbation on the reduced spin Hamiltonian of the Eu^{3+} (Equation 2.3), with which the magnetic dipole moment of the Eu^{3+} ion can be calculated. Then the magnetic dipole-dipole interaction can be calculated with this magnetic dipole moment.

5.1.1 The spin frequencies of the frozen-core Y^{3+} ions

The resonant frequency of the i-th frozen-core Y^{3+} spin is given by:

$$\nu_Y = \gamma|\boldsymbol{B} + \boldsymbol{dB_i}|, \tag{5.1}$$

where $\gamma = 2.09 \times 10^6$ Hz/T is the gyromagnetic moment of Y^{3+} ions, $\boldsymbol{B}$ is the applied magnetic field and $\boldsymbol{dB_i}$ is the field due to the Eu^{3+} ion. The value of $\boldsymbol{B}$ is defined

$$\boldsymbol{dB_i} = \frac{\mu_0}{4\pi}\left(\frac{3(\boldsymbol{m_{Eu}}\cdot\boldsymbol{r}_i)\boldsymbol{r}_i}{|\boldsymbol{r}_i|^5} - \frac{\boldsymbol{m_{Eu}}}{|\boldsymbol{r}_i|^3}\right), \tag{5.2}$$

where $\mu_0 = 4\pi \times 10^{-7}$ T·m/A is the vacuum permeability, $\boldsymbol{r_i}$ is the displacement of the i-th Y^{3+} ion relative to the Eu^{3+} ion and $\boldsymbol{m_{Eu}}$ is the magnetic moment of the Eu^{3+} spin.

The Eu^{3+} magnetic moment $\boldsymbol{m_{Eu}}$ has two different contributions in the presence of an external magnetic field, which are the induced moment and the nuclear magnetic moment. As detailed in Section 2.5.3, the induced moment is linearly dependent on the field magnitude. All measurements presented in this chapter are near the critical field $\mathbf{B_{cp}}$, which is of the order of 1 T, where the induced moment is much larger than the nuclear magnetic moment and thus the latter can be ignored. To summarise, the value $\boldsymbol{dB_i}$ is determined by the induced moment of the Eu^{3+}, which is linearly dependent on the applied magnetic field.

For different Y^{3+} ions, the relative positions with respect to the Eu^{3+} are different, namely the $\boldsymbol{r_i}$ value in Equation 5.2 is different, thus they have different $\boldsymbol{dB_i}$. Hence, the resonant spin frequencies of the frozen-core Y^{3+} ions are detuned from each other. The detuning frequency of an frozen-core Y^{3+} from the bulk can be calculated:

$$d\nu_Y = \gamma(|\boldsymbol{B} + \boldsymbol{dB_i}| - |\boldsymbol{B}|). \tag{5.3}$$

The calculated values of $d\nu_Y$ at a given field for some of the nearest frozen-core Y^{3+} ions are listed in Table 5.1 and the measurement of the spin transition frequencies for these Y^{3+} ions is presented in Section 5.2.

5.1.2 The frequency shift of the Eu^{3+} hyperfine transition when flipping an Y^{3+} spin

While the resonant frequency of the frozen-core Y^{3+} ions is dominated by the induced moment of the Eu^{3+} ion, the frequency shift of the Eu^{3+} hyperfine transition resulting from flipping an Y^{3+} spin is related to the nuclear magnetic moment. The spin flip of the i-th frozen-core Y^{3+} ion produces a magnetic field perturbation $\boldsymbol{\delta B_i}$ at the Eu^{3+} site,

resulting in a frequency shift of Eu^{3+} hyperfine transition given by:

$$\delta f = \boldsymbol{S} \cdot \boldsymbol{\delta B_i}, \tag{5.4}$$

where $\boldsymbol{S}$ is the field sensitivity of the transition [1]. As discussed in Section 2.5.4, $\boldsymbol{S} = \boldsymbol{\Delta m}$, where $\boldsymbol{\Delta m}$ is the difference in the Eu^{3+} magnetic moment between the hyperfine ground and excited states. The induced moment is independent of the hyperfine state, thus $\boldsymbol{\Delta m}$ is given by the difference in the nuclear magnetic moment of the two hyperfine states. At a critical point, as shown in Figure 2.12, $\boldsymbol{\Delta m} = 0$, and so flipping a Y^{3+} spin does not produce any frequency shift in the Eu^{3+} hyperfine transition. When the field is detuned from the critical point, there is a non-zero value of $\boldsymbol{\Delta m}$. The magnitude of $\boldsymbol{\Delta m}$ is dependent on the amount of field detuning from the critical point.

A measurement of this frequency shift is presented in Section 5.5. This measurement was performed by applying a resonant π_Y pulse to drive the spin flip of one individual Y^{3+} ion, as shown in Figure 5.1, and recording the two pulse spin echo amplitude of the Eu^{3+} ion.

In a two pulse spin echo measurement of the Eu^{3+} ion, a frequency shift δf during the echo sequence results in a phase shift of the echo signal:

$$\begin{aligned} \delta\alpha(\tau) &= 2\pi\,\delta f\,\tau \\ &= 2\pi(\boldsymbol{S} \cdot \boldsymbol{\delta B_i})\tau, \end{aligned} \tag{5.5}$$

where τ is the total delay. Thus, when a π_Y pulse is applied resonant with one of the frozen core Y^{3+} spin frequency, a well defined phase shift of the Eu^{3+} echo signal might be expected. In fact, applying a π_Y pulse leads to a modulation of the echo amplitude, and no phase shift. As explained below, this is a consequence of the random distribution of the initial Y^{3+} state on the Bloch sphere.

To understand the modulation, it is first necessary to determine the phase shift of an individual Eu^{3+} ion when the frozen core Y^{3+} ion nearby, which is in an arbitrary state, is flipped. In particular, we are interested in the phase shift on the Eu^{3+} ion at the time of the echo. The dipolar interaction between Eu^{3+} and Y^{3+} ions means they constitute a coupled system and their states are entangled. A complete treatment of this problem involves solving the full coupled Hamiltonian. However, since the interaction is purely diagonal (it only leads to shifts in energy levels), it is possible to understand the appearance of amplitude modulation by just considering the action of the Y^{3+} on the Eu^{3+} state.

In the absence of the π_Y pulse, assume that at the time of the echo the Eu^{3+} ion is along the $-x$ axis of the Bloch sphere,

$$\boldsymbol{M_0} = \begin{bmatrix} u_0 \\ v_0 \end{bmatrix} = \begin{bmatrix} -1 \\ 0 \end{bmatrix}; \tag{5.6}$$

When the π_Y pulse is applied, this leads to a phase shift on this Bloch vector that accumulates over the evolution time τ. At the time of the echo, the phase shift can be described by a rotation of the vector about the z axis:

$$\boldsymbol{M_{flip}} = \boldsymbol{R}(\tau)\boldsymbol{M_0} \tag{5.7}$$

[1] Only the first order field sensitivity is considered.

To work out the phase shift for an arbitrary state, we first consider the phase shift when the Y^{3+} is in one of its stationary states $|g\rangle$ and $|e\rangle$. If the Y^{3+} is in $|g\rangle$, then the π_Y pulse flips it to $|e\rangle$. Assume that this leads to a positive frequency shift on the Eu^{3+} ion and hence a positive phase shift:

$$R^{+}(\tau) = \begin{bmatrix} \cos(\delta\alpha(\tau)) & \sin(\delta\alpha(\tau)) \\ -\sin(\delta\alpha(\tau)) & \cos(\delta\alpha(\tau)) \end{bmatrix}; \tag{5.8}$$

If the Y^{3+} starts in the excited state, flipping it will lead to an opposite frequency shift and hence a negative phase shift:

$$R^{-}(\tau) = \begin{bmatrix} \cos(-\delta\alpha(\tau)) & \sin(-\delta\alpha(\tau)) \\ -\sin(-\delta\alpha(\tau)) & \cos(-\delta\alpha(\tau)) \end{bmatrix}. \tag{5.9}$$

If the Y^{3+} starts in an arbitrary state, the phase shift will be between these two extremes. An arbitrary Y^{3+} state can be written in terms of the two stationary states as (See Section 3.1.1):

$$|Y_B\rangle = \sin\frac{\theta}{2}|g\rangle + e^{i\phi}\cos\frac{\theta}{2}|e\rangle. \tag{5.10}$$

By considering the full coupled system, it can be shown that the phase shift of the Eu^{3+} Bloch vector for an arbitrary Y^{3+} state is

$$R(\tau,\theta) = \sin^2\frac{\theta}{2}R^{+}(\tau) + \cos^2\frac{\theta}{2}R^{-}(\tau). \tag{5.11}$$

This equation shows that the phase shift of an individual Eu^{3+} Bloch vector as a function of the Y^{3+} state. To work out the echo amplitude, it is necessary to consider the entire Eu^{3+} ensemble. Since the Y^{3+} ions can be assumed to be completely randomly distributed, the total echo amplitude can be obtained by integrating over all possible Y^{3+} states:

$$\begin{aligned} \boldsymbol{M}(\tau) &= \int_0^{2\pi}\int_0^{\pi} R(\tau,\theta)\boldsymbol{M_0}\sin(\theta)d\theta d\phi \qquad (5.12)\\ &= \int_0^{2\pi}\int_0^{\pi} (\sin^2\frac{\theta}{2}R^{+}(\tau) + \cos^2\frac{\theta}{2}R^{-}(\tau))\begin{bmatrix}-1\\0\end{bmatrix}\sin(\theta)d\theta d\phi \\ &= 4\pi\cos(\alpha(\tau))\begin{bmatrix}-1\\0\end{bmatrix} \\ &= 4\pi\cos(\alpha(\tau))\boldsymbol{M_0} \\ &= 4\pi\cos(2\pi\delta f\tau)\boldsymbol{M_0} \qquad (5.13) \end{aligned}$$

This gives an echo signal dependent on the evolution time τ as:

$$E(\tau) \propto \cos(2\pi\delta f\tau). \tag{5.14}$$

Thus, the echo amplitude has a modulation over the evolution time τ. A measurement of such an echo modulation is presented in Section 5.5.

According to Equation 5.5, the frequency shift δf is dependent on $\boldsymbol{S}$ and $\boldsymbol{\delta B_i}$. The field sensitivity $\boldsymbol{S}$ is determined by the amount of field detuning from the critical point,

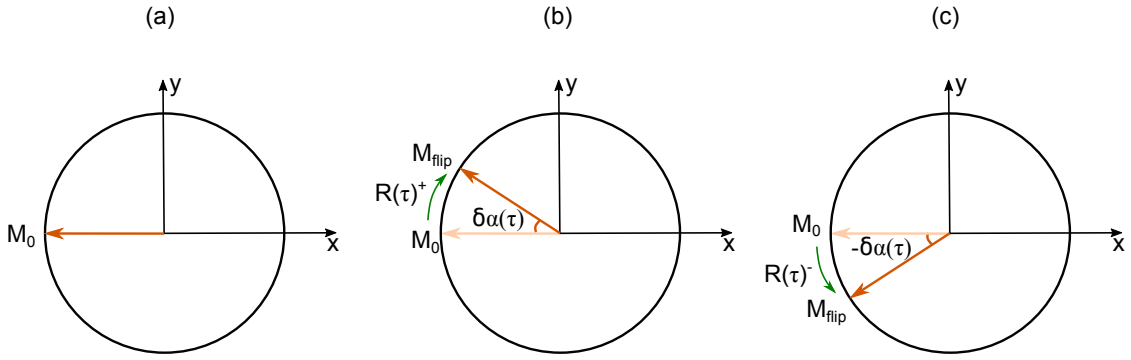

Figure 5.2: Bloch sphere illustration of the A spin coherence emission. (a), If A is not coupled to B, the Bloch vector of A spin can be represented using $\boldsymbol{M_0}$ as marked. (b), If A is coupled to the B spin system, which is prepared purely in the $|g\rangle$ state, a positive phase shift is produced, the Bloch vector of the A spin is rotated from $\boldsymbol{M_0}$ to $\boldsymbol{M(\tau)}$. (c), If A is coupled to the B spin system, which is prepared purely in the $|e\rangle$ state, a negative phase shift is produced instead.

or the field alignment. The field perturbation $\boldsymbol{\delta B_i}$ for an individual Y^{3+} ion is determined by its position with respect to the Eu^{3+} ion. Flipping each frozen-core Y^{3+} spin results in a different value of $\boldsymbol{\delta B_i}$ on the Eu^{3+} ion. This means that each individual frozen-core Y^{3+} site has its unique echo modulation frequency, which is a measure of the interaction strength δf (Equation 5.4) between this Y^{3+} ion and the Eu^{3+} ion. In other words, for a fixed field alignment and fixed delay τ, resonantly driving the spin flip of different Y^{3+} ions using the narrowband π_Y pulse should result in different echo amplitudes, as demonstrated in the measurement presented in Section 5.2.

This modulation effect is only observable in a particular magnetic field regime: close to, but not exactly on, a critical point. In the above discussion, the focus was on one individual frozen-core Y^{3+} ion while the echo decay due to the reconfiguration of other Y^{3+} ions was ignored. This is only true when the measurement is performed near a critical point where the effect of the bulk Y^{3+} spin flips is negligible due to the small field sensitivity. Otherwise, if the field is completely away from a critical point, the echo signal decays quickly to zero due to the fast spin flips of the bulk Y^{3+} ions before a slow modulation caused by a frozen-core Y^{3+} ion can be observed. Equally, however, if there is a spontaneous spin flipping of the frozen-core Y^{3+} spin during the modulation period $1/(\delta f)$, an echo modulation for an individual Y^{3+} ion produced by the π_Y pulse will not be observable, thus, the echo modulation period must be made sufficiently short. In order to shorten the modulation period $1/(\delta f)$ such that it is shorter than the lifetime of the frozen-core Y^{3+} spins, the field sensitivity needs to be increased by detuning the field from the critical point. Hence, the field alignment should be made such that:

$$\frac{1}{R_b} \ll \frac{1}{\delta f} \ll \frac{1}{R_f}, \tag{5.15}$$

where $1/R_b = 3.5\ ms$ is the correlation time of the bulk Y^{3+} ions [104] and $1/R_f$ is the correlation time of the frozen-core Y^{3+} spins. In the previous section, at the investigated critical point $\mathbf{B_{cp}}$, $1/R_f$ was measured to be 59 s. To satisfy Equation 5.15, all the measurements to be discussed in this chapter were performed at a field detuned by (16±10) G from the critical point $\mathbf{B_{cp}}$. The reason for this large field uncertainty is explained in Sec-

tion 4.3.4. The interaction strength δf at this field value can be calculated according to Equation 5.4. The calculation of the field sensitivity $\boldsymbol{S} = \boldsymbol{\Delta m}$ at a given field is detailed in Section 2.5.4. The field perturbation $\boldsymbol{\delta B_i}$ acting on the Eu^{3+} produced by flipping a Y^{3+} spin can be calculated using

$$\boldsymbol{\delta B_i} = \frac{\mu_0}{4\pi}\left(\frac{3(\boldsymbol{m_Y}\cdot\boldsymbol{r}_i)\boldsymbol{r}_i}{|\boldsymbol{r}_i|^5} - \frac{\boldsymbol{m_Y}}{|\boldsymbol{r}_i|^3}\right), \tag{5.16}$$

where $\boldsymbol{m_Y}$ is the magnetic moment of the Y^{3+} spin.

The calculated δf, at the experimental magnetic field, corresponding to different Y^{3+} sites is listed in Table 5.1. These values all satisfy Equation 5.15. In addition, the frequency detunings of the spin transition for these frozen-core Y^{3+} ions at this field, calculated using the method detailed in Section 5.1.1, are also listed in the Table 5.1.

Label of Y site	Y position $\lvert\mathbf{r}\rvert$ (Å)	δf (Hz)	$d\nu_Y$ (Hz)
Y_1	3.403	0.2±0.3	-461±1
Y_2	3.525	0.5±0.3	1458±1
Y_3	3.651	0.4±0.3	-373±1
Y_4	3.735	0.4±0.3	324±1
Y_5	3.775	0.4±0.3	1070±1
Y_6	4.022	0.18±0.05	70±1
Y_7	4.162	0.11±0.05	-225±1
Y_8	4.689	0.14±0.05	-329±1
Y_9	4.937	0.13±0.05	-207±1
Y_{18}	6.248	0.04±0.03	-139.4±0.1
Y_{30}	7.295	0.05±0.03	18.94±0.1

Table 5.1: The calculated coupling strength δf between the Eu^{3+} and different frozen-core Y^{3+} ions, as well as the frequency detuning $d\nu_Y$ of the spin transition for these Y^{3+} ions. The 'Y position' is the distance between the Eu^{3+} ion and the Y^{3+} ion. The calculation was performed at a field along $\mathbf{B_{cp}}$, with a magnitude detuned from $|\mathbf{B_{cp}}|$ by (16 ± 10) Hz.

5.2 Spectrum measurement of the frozen-core Y^{3+} sites

In order to investigate the dynamics of an individual Y^{3+} site, it is necessary to work out its spin transition frequency. As discussed in the previous section, the resonant spin frequencies of the different Y^{3+} sites are detuned from the bulk and each other. This section describes the measurement of the spectrum for these resonant spin frequencies.

The measurement was performed using the RF pulse sequence in Figure 5.1. The required frequency of the π_Y pulse was estimated based on the field applied (1.29 T) and the gyromagnetic ratio of the Y^{3+} ion (2.09 MHz.T^{-1}). This frequency is the value for the bulk Y^{3+} ions and in order to find the frequency for a frozen-core Y^{3+}, the Eu^{3+} echo was observed by adjusting the frequency of the π_Y pulse for a fixed delay until a minimum value of the echo amplitude was achieved, indicating a large perturbation to the

Eu^{3+} ion. Then the frequency of the π_Y pulse was fixed and the total delay of the Eu^{3+} pulses was adjust until the echo amplitude was further minimized. This minimization process was performed because the echo signal is dependent on both the frequency of the π_Y pulse and the total delay τ. This process identified the spin transition frequency and the modulation period of one of the Y^{3+} sites. After that, with the delay fixed, the frequency of the π_Y pulse was scanned over 9 kHz and the Eu^{3+} echo amplitude was record to identify other Y^{3+} frequencies. Because each Y^{3+} ion corresponds to a different echo modulation frequency, at this fixed delay, they would not all experience a maximal echo modulation. However, because the minimisation process was performed on an Y^{3+} ion that has a median modulation frequency, for most other frozen-core Y^{3+} ions, some amount of decrease in the echo amplitude was expected when the π_Y frequency becomes resonant with their spin transitions.

The measured Y^{3+} spectrum is shown in Figure 5.3(a), with the Eu^{3+} echo amplitude plotted vs. the frequency of the π_Y pulse. Each of the five peaks (p_1 to p_5) shown in the spectrum represents a frozen-core Y^{3+} site. Although the frequencies for these peaks are determined by the frozen-core effect, the amplitude of each peak is not directly related to the frequency detuning caused by the frozen core, The amplitude of each is determined by the coupling strength $\boldsymbol{\delta B_i}$ and the echo delay τ. Hence, the peaks with the largest modulation depth (p_1 and p_5) may not necessarily have the strongest coupling strength. In this initial measurement of the frequency shifts, the delay was chosen to give a clear spectrum, and in doing so a value was picked which maximised the signal from p_1 and p_5. At this delay, driving p_1 and p_5 Y^{3+} sites produced a phase shift of the echo signal close to π.

The experimental peaks ($p_1 - p_5$) were assigned to the frozen-core Y^{3+} sites by comparing the experimental results with the calculated frequency detuning. The calculation was discussed in the previous section and the spectrum of the calculated frequency detuning of the 20 nearest frozen-core Y^{3+} ions is presented in Figure 5.3(b). The difference in the frequency detuning between the two Y^{3+} sites with maximum plus detuning (Y_1) and minus detuning (Y_2) is ~1.9 kHz, in good agreement with the separation between the peak p_1 and p_5 of the measured spectrum. Hence, the peaks p_1 and p_5 were assigned to these two Y^{3+} sites respectively. Then peaks p_2 was assigned to Y_{18} and p_3 to Y_4. However, in the calculated spectrum, there is no frequency that matches the peak p_4. This is probably because peak p_4 is a mixture of signals from multiple Y^{3+} sites. The different Y^{3+} sites in the crystal corresponding to the experimental peaks are shown in Figure 5.3(c).

The theoretical simulation shows that there are more than five frozen-core Y^{3+} sites, which means that Figure 5.3 is not a complete mapping of all frozen-core Y^{3+} sites. This is due to the poor resolution of the measured spectrum. One possibility limiting the spectral resolution was thought to be the Rabi frequency of the applied π_Y pulse, 111 Hz, was not narrow enough to resolve all the Y^{3+} sites in the frozen core. Based on this hypothesis the measurement was repeated by using narrower π_Y pulses, but the resolution of the spectrum was not significantly improved. Hence, it is likely that the spectral resolution is limited by the inhomogeneity in the applied magnetic field, which is on the order of 1 G. This 1 G field inhomogneity results in a 100 Hz inhomogenous broadening of the spin transition of the Y^{3+} spin bath. Once the inhomogeneity in the field is improved, using a π_Y pulse with a narrower bandwidth should lead to better spectral resolution.

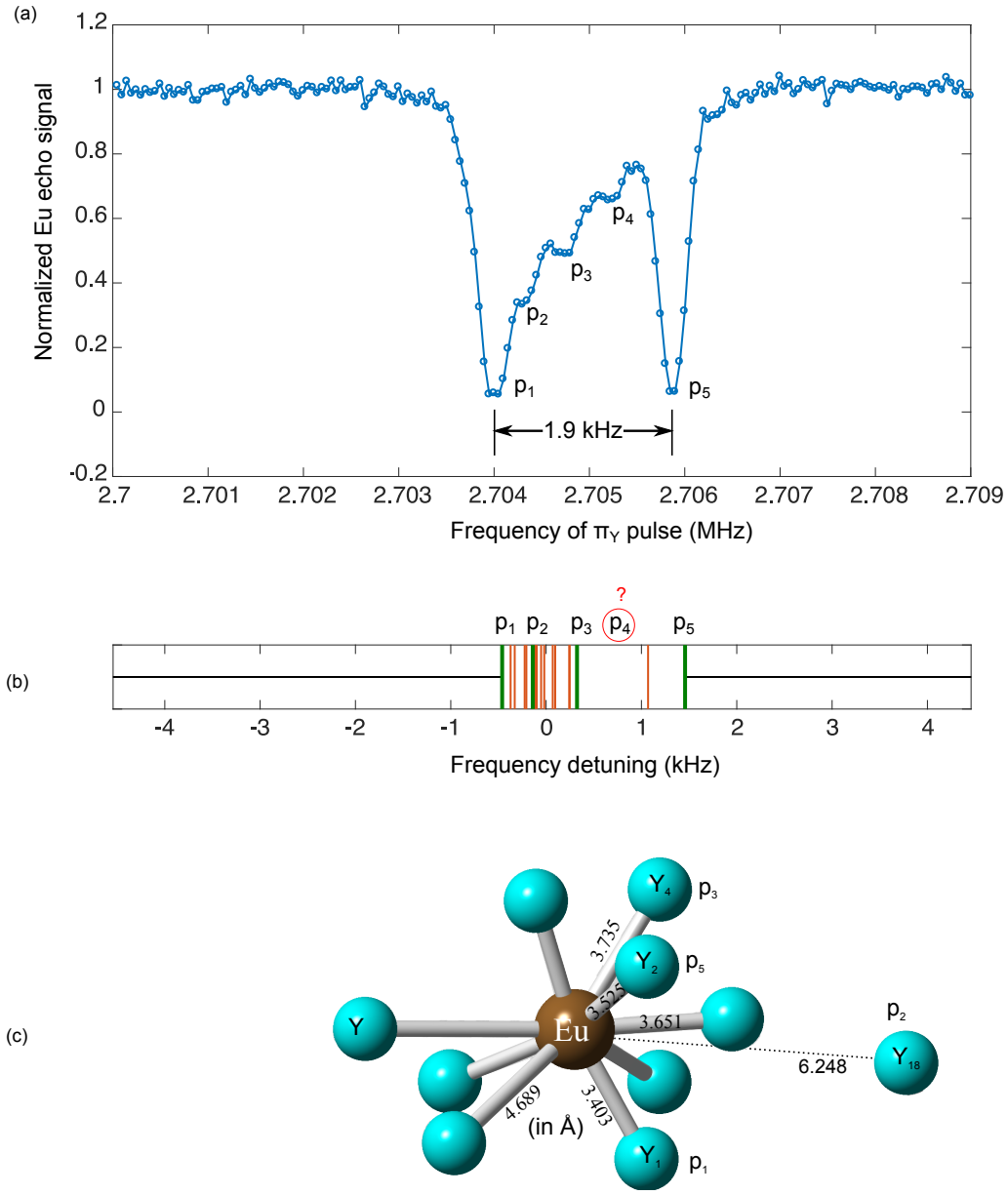

Figure 5.3: (a), The measured spectrum of the frozen-core Y^{3+} spin transitions near the critical point $\mathbf{B_{cp}}$, with the Eu^{3+} echo amplitude plotted against the frequency of the π_Y-pulse. (b), The calculated detuning of the spin transition for the nearest 20 frozen core-Y^{3+} ions. Each vertical line represents the frequency detuning for a Y^{3+} site. The lines in green represent those Y^{3+} sites which are assigned with the experimental peaks as marked. (c), The crystal information for the resolved Y^{3+} sites. The Y^{3+} sites 'Y_1', 'Y_2' and so on are named based on the distances between the Eu^{3+} and the Y^{3+} ions. For example, the 'Y_1' is the closest Y^{3+} site.

5.3 Nutation measurements for the frozen-core Y^{3+} spins

In the previous section, the spin transition frequency for different Y^{3+} ions was resolved. With this information, the dynamics of one individual Y^{3+} ion can be studied by setting the frequency of the π_Y pulse resonant with that site. This section presents measurements of nutation for two of the frozen-core Y^{3+} spins. A nutation measurement can provide a simple illustration of the effect of a π_Y pulse on the Eu^{3+} ion and it also gives the Rabi frequency of the π_Y pulse, which is required in the coherence time and echo modulation measurements in the next two sections.

The nutation measurement was performed by setting the frequency of the π_Y pulse to be resonant with one of the Y^{3+} sites and observing the Eu^{3+} echo amplitude when scanning the length of the π_Y pulse. Again, the RF pulse sequence used is shown in Figure 5.1, and the total Eu^{3+} delay was set to maximise the echo modulation. The echo amplitude was then recorded as the length of the π_Y pulse was varied from 0.25 ms to 55 ms. Nutation measurements were performed at two frequencies, at peaks p_1 and p_5.

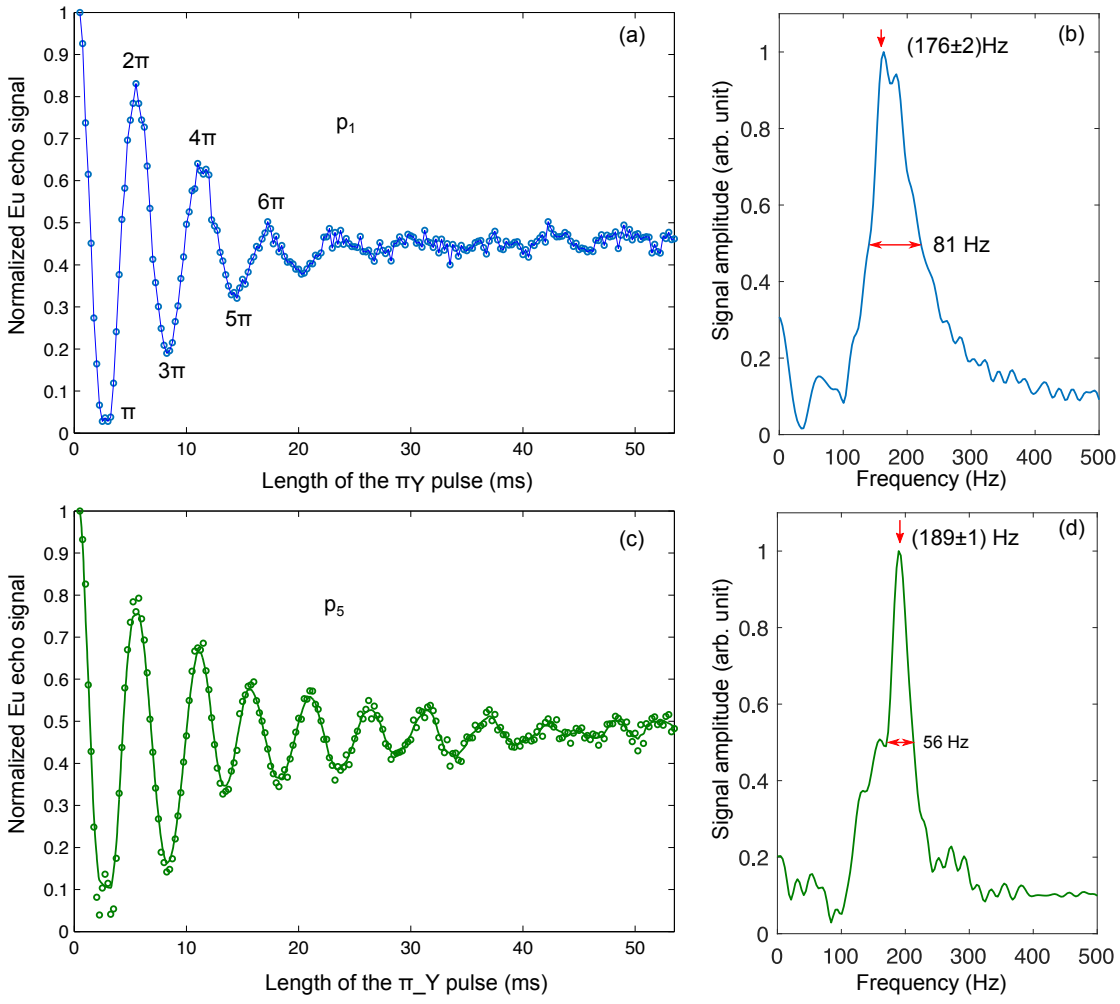

Figure 5.4: (a) and (c), The nutation measurements at p_1 and p_5 respectively, with the Eu^{3+} echo amplitude plotted against the length of the π_Y-pulse. (b) and (d), Fourier transforms of the nutation signals. The frequencies of the Fourier transform plots are the Rabi frequencies for each site. The broadening of each Fourier transform plot represent the decay of the nutation.

The measured nutations are shown in Figure 5.4, with the Eu^{3+} echo amplitude plotted against the length of the π_Y pulse. For both p_1 and p_5 Y^{3+} sites, clear nutations were produced as expected. The Rabi frequencies measured from the nutation are (176 ± 1) Hz and (189 ± 2) Hz respectively for for sites p_1 and p_5 respectively. The uncertainty is from the the difficulty in determing the centre frequencies. The Rabi frequencies for the two Y^{3+} sites agree. This is expected because the same RF intensity of the π_Y pulse was used for the two sites and they have almost the same spin transition frequency [2].

The nutation decay is due to the inhomogeneous broadening of the Y^{3+} spin transition, which, as discussed earlier, is mainly caused by the inhomogeneity of the applied magnetic field. In this case, as different Y^{3+} spins experience the same inhomogeneous broadening, the same decay rate for p_1 and p_5 might be expected. However, as demonstrated in Figure 5.4, the nutation of p_5 decays much slower than p_1. The faster nutation decay of p_1 is likely due to the off-resonant excitation of other sites, which could be the nearby p_2 site or other unresolved sites. As shown in the measured spectrum (Figure 5.3), p_5 is relatively isolated compared to the other peaks.

5.4 Coherence time measurement for the frozen-core Y^{3+} spins

The homogeneous linewidth of the frozen-core Y^{3+} spins is an important parameter in calculating the cross relaxation rate of the frozen-core spins [107]. In order to determine this homogeneous linewidth, in this section, a measurement of the coherence time for a frozen-core Y^{3+} spin is presented.

The applied pulse sequence is shown in Figure 5.5(a). Rather than a single π_Y-pulse, two different three-pulse sequences were applied prior to the Eu^{3+} π pulse. One of the Y^{3+} pulse sequences was $\pi/2$, π and $\pi/2$ (RF_{Ya}) while the other was $\pi/2$, π and $-\pi/2$ (RF_{Yb}). The frequency of these pulses was set to be the resonant frequency of the p_5 site.

In Figure 5.5(b), the effect of these two Y^{3+} pulse sequences is illustrated using the Bloch sphere by assuming that the Y^{3+} ions are initialised in the ground state. For both Y^{3+} sequences, the first $\pi/2$-pulse rotates the Y^{3+} spins to the 50-50 superposition state, then the Bloch vectors of the individual frequency subgroups start to precess around the Bloch sphere with a rate corresponding to their detunings. A π-pulse is then applied and the Bloch vectors of the frozen-core Y^{3+} ensemble gradually refocus. For the RF_{Ya} sequence, a third $\pi/2$-pulse drives the refocused Bloch vector to the initial ground state while for RF_{Yb} squence, the third $-\pi/2$-pulse drives the refocused Bloch vector to the excited state. This means that the RF_{Ya} sequence would recover the spin state while the RF_{Yb} sequence would flip the spins. However, this is only true when the total evolution time of the Y^{3+} pulse sequences is much shorter than the coherence time of the frozen core Y^{3+} ions, namely $\tau_Y \ll T_{2Y}$. As shown in Figure 5.5(c), when $\tau_Y \gg T_{2Y}$, the frozen-core Y^{3+} ensemble Bloch vectors would have already lost coherence completely before the second π-pulse was applied and would not be refocused. After either the RF_{Ya} or RF_{Yb} sequence, there would be half of the spins in the upper hemisphere and half in the lower hemisphere of the Bloch sphere.

The previous section has discussed that flipping a Y^{3+} spin will cause an attenuation of the echo amplitude if the Eu^{3+} delay was set at the minimum value of the echo modulation.

[2] As the spin transition frequency for Y^{3+} ions at the applied strong field is a few MHz, when considering the Rabi frequency, the kHz scale frequency detuning due to the frozen-core is negligible.

From the above discussion, by applying pulse sequences RF_{Ya} and RF_{Yb} and observing the Eu^{3+} echo amplitude, the coherence time of the resonant frozen-cor Y^{3+} spin can be measured. To work out this coherence time, the Eu^{3+} echo amplitudes was recorded sequentially for both sequences for each Y^{3+} delay τ_Y, from 10 ms to 800 ms.

The result is shown in Figure 5.6 with the Eu^{3+} echo amplitude plotted against τ_Y. Two data sets were recorded, corresponding to pulse sequence RF_{Ya} and RF_{Yb} as marked. At short τ_Y, for the data set RF_{Ya}, the Eu^{3+} echo amplitude was not attenuated because the pulse sequence recovers the spin state. As τ_Y increases, the frozen-core Y^{3+} spins gradually lose coherence, and sequence RF_{Ya} is less effective at recovering the spins, resulting in decreasing Eu^{3+} echo amplitude. The echo amplitude kept decreasing until τ_Y reached the value at which the frozen-core Y^{3+} spins completely lose coherence. After that, the Eu^{3+} echo amplitude stayed constant as τ_Y was lengthened. This is because, when the coherence disappeared, half of the spins are in the upper hemisphere and half in the lower hemisphere of the Bloch sphere as stated above. The measured data set for RF_{Ya}, then, is in complete agreement with the theory.

The pulse sequence RF_{Yb} reverses the Y^{3+} spin state completely at $\tau_Y \ll T_{2Y}$, hence, a minimum Eu^{3+} echo amplitude is expected initially, and then the echo amplitude is expected to increase until the frozen-core Y^{3+} spins lose coherence completely. However, for the data set marked RF_{Yb}, an initial decrease of the Eu^{3+} echo amplitude was observed. After this initial drop, the echo amplitude increased in the way expected until it reached the same constant value as the data set RF_{Ya}. The cause of the initial drop of the echo amplitude is not completely understood, although it seems to be due to the fact that the Eu^{3+} delay was not set correctly to maximize the echo modulation (see Section 5.5).

From the above discussion, an exponential fit to the echo decay for sequence RF_{Ya} is a measure of the frozen core Y^{3+} coherence time. The fit resulted in a coherence time $T_{2Y} = 1.6$ s.

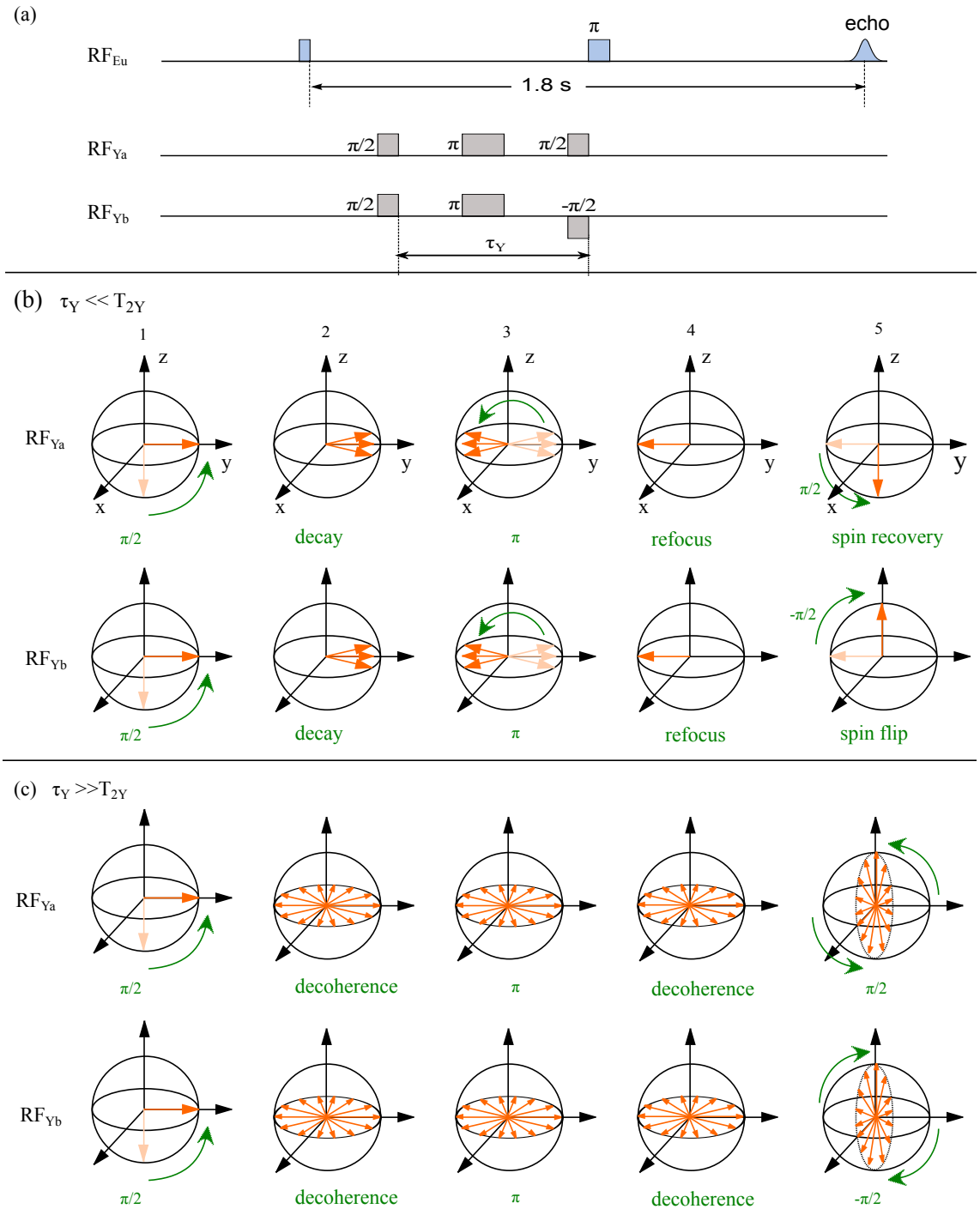

Figure 5.5: (a), The pulse sequence used to measure the coherence time of frozen-core Y^{3+} spins. Two different Y^{3+} pulse sequences, RF_{Ya} and RF_{Yb}, were applied prior to the Eu^{3+} π pulse. The Eu^{3+} delay was kept constant and the Eu^{3+} echoes were recorded at different Y^{3+} delays τ_Y. (b), The Bloch sphere representation of the Y^{3+} spins driven by RF_{Ya} and RF_{Yb} for $\tau \ll T_{2Y}$. The RF_{Ya} sequence recovers the spin state while RF_{Yb} sequence flips the spins. (c), The Bloch sphere representation of the Y^{3+} spins driven by the RF_{Ya} and RF_{Yb} sequences for $\tau \gg T_{2Y}$. The frozen-core Y^{3+} ensemble Bloch vectors lose coherence completely before the second π-pulse is applied and are not refocused. After either a RF_{Ya} or RF_{Yb} sequence, half of the spins are in the upper hemisphere and half in the lower hemisphere.

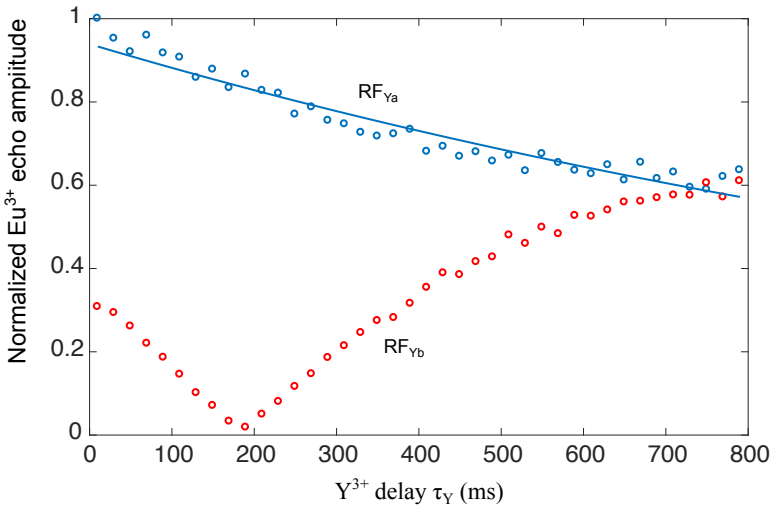

Figure 5.6: The result for frozen-core Y^{3+} coherence time measurement with the Eu^{3+} echo amplitude plotted as a function of the Y^{3+} delay. Open circles show echo decay with the applied RF_{Ya} and RF_{Yb} sequences respectively as marked. The solid line is an exponential fit for the RF_{Ya} data set, which resulted in a coherence time of 1.6 s.

5.5 Measurement of the Eu^{3+}-Y^{3+} ion-ion interactions and Y^{3+} spin lifetime

Although I explained theoretically in Section 5.1.2 that an Eu^{3+} echo amplitude modulation against the total delay τ is expected when flipping an Y^{3+} spin, all measurements demonstrated in the previous sections were performed with a fixed Eu^{3+} delay. In this section, by varying the Eu^{3+} delay, an echo modulation was experimentally demonstrated.

The measurement was performed using the pulse sequence shown in Figure 5.1, with the frequency resonant with the peak p_5 Y^{3+} site. Based on the nutation measurement, the length of the π_Y-pulse was set to be 2.75 ms. With this fixed π_Y pulse, the Eu^{3+} echo amplitude was recorded by varying the total delay of the Eu^{3+} pulse sequence. To observe the effect of the π_Y pulse on the Eu^{3+} echo decay, for each delay, the Eu^{3+} echo amplitude with and without a π_Y-pulse were recorded sequentially.

The measured Eu^{3+} two pulse spin echo amplitude as a function of the total delay is shown in Figure 5.7(a). The data set in orange is a two pulse spin echo decay without a π_Y-pulse while the one in blue is a two pulse spin echo decay perturbed by the π_Y-pulse. The echo decay without a π_Y pulse has a contribution from the spontaneous spin flips of all the Y^{3+} ions. For the echo decay with a π_Y pulse, this contribution remains, and there is an additional contribution from the spin flips of the p_5 Y^{3+} ion. In order to get rid of the effect of the spontaneous spin flips of the other Y^{3+} ions, the data set with the π_Y pulse was normalised using the data set without a π_Y pulse, which results in the normalised data set as shown in Figure 5.7(b). The normalised data shows a clear modulation of the echo amplitude. This modulation is the result of the Eu^{3+} ion coupling to the p_5 frozen-core Y^{3+} ions. The beat frequency of the modulation, $\delta f = 0.25$ Hz, is a measure of the interaction strength, namely the frequency shift of the Eu^{3+} hyperfine transition when the p_5 Y^{3+} spin is flipped. The p_5 peak was assigned to the Y_2 Y^{3+} site according to the spectrum measurement presented in Section 5.2. The theoretically calculated interaction

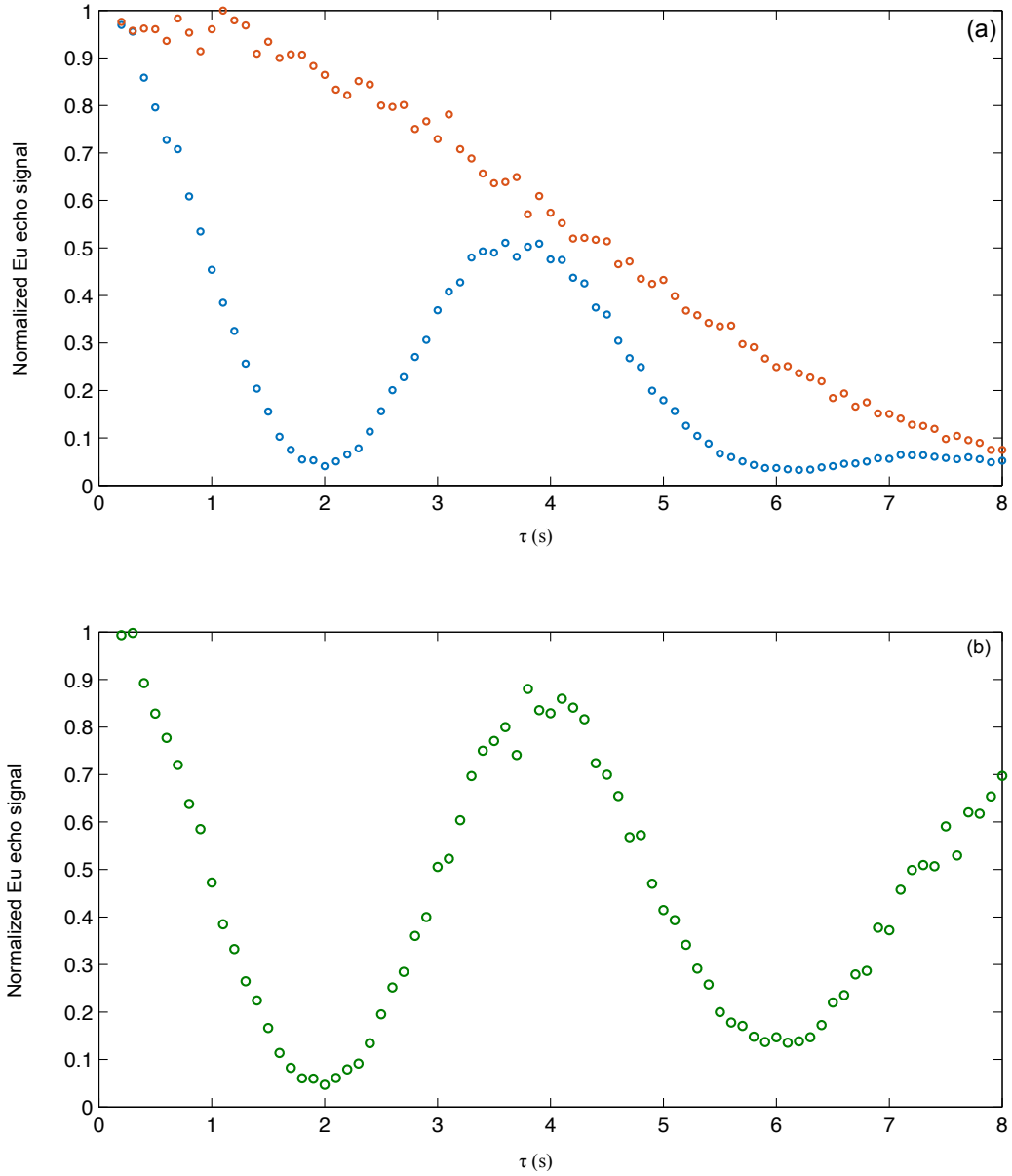

Figure 5.7: (a), Open circles in orange shows the Eu^{3+} echo decay without a π_Y-pulse. The data in blue circles shows the Eu^{3+} echo decay in the presence of perturbing π_Y-pulse. (b), The normalised Eu^{3+} echo decay of the orange data set using the blue data set.

strength for this Y_2 is $\delta f = 0.5 \pm 0.3$ Hz, as listed in Table 5.1. Hence, the measured $\delta f = 0.25$ Hz is in reasonable agreement with the theoretical value.

The envelope decay of the normalised data set in Figure 5.7(b) is a measure of the lifetime of the p_5 Y^{3+} spin, which is 27±10 s. There is no inconsistent between this number and the measured correlation time of the Y^{3+} spins in the frozen core, 59 s, from the two pulse spin echo decay at $\mathbf{B_{cp}}$ (Section 4.4). For distinction, the former (27 s) is the lifetime of one particular individual Y^{3+} spin while the latter, the correlation time of 59 s, is an averaged lifetime over all the frozen-core Y^{3+} spins.

5.6 Discussion

This chapter studied dynamics of the frozen-core Y^{3+} spins in Eu^{3+}:Y_2SiO_5. A better understanding of these dynamics allows the possibility to extend the hyperfine coherence time of the Eu^{3+} ions by decoupling the Y^{3+} ions from Eu^{3+} using more sophisticated pulse sequences. In addition, this study showed that it is possible to re-orient the polarisation of the Y^{3+} spins in a particular well-defined crystalline site. This implies the potential of spin cooling the frozen-core and using it as a resources to perform quantum computing.

The frozen core effect results in detuned spin transition frequencies of the Y^{3+} ions in the core. A spectrum of these frequencies was measured and the frequencies were preliminarily assigned to Y^{3+} sites in the crystal. However, fewer frozen-core Y^{3+} sites were experimentally observed than predicted. This was due to the poor resolution of the experimental spectrum which was caused by the inhomogeneity in the applied magnetic field. Hence, a complete mapping of all the frozen-core Y^{3+} sites might be achieved by improving the field inhomogeneity.

The above method of mapping the frozen-core Y^{3+} sites is based on the fact that the frozen-core Y^{3+} have spin transition frequencies detuned from each other. We can also assign the frozen-core Y^{3+} sites by measuring their different interaction strength δf with the Eu^{3+} ion. In this chapter, the interaction strength of one of the Y^{3+} site was successfully measured. By repeating this measurement on other sites it will be possible to measure the interaction strength of all the Y^{3+} sites, and by comparing the experimental results and the theoretical results, a complete assignment of all the frozen-core Y^{3+} sites is possible.

The lifetime of the Y^{3+} spin in one of the frozen-core sites was measured, and was in reasonable agreement with the measured correlation time of the frozen-core Y^{3+} ions demonstrated in the previous chapter. One of the major spin relaxation mechanism is cross relaxation. The cross relaxation rate $1/T_{CR}$ of two nuclear spins can be calculated using a model developed by Bloembergen et al. in 1958 [107]:

$$\omega_{ij} = \frac{2\pi}{T_{CR}} = \frac{|\langle\varphi_i|H_{int}|\varphi_j\rangle|^2}{\sqrt{2\pi}h^2}\left[\frac{\exp\left\{\frac{-(\nu_1-\nu_2)^2}{(\Delta\nu_1)^2+(\Delta\nu_2)^2}\right\}}{\sqrt{(\Delta\nu_1)^2+(\Delta\nu_2)^2}}\right] \tag{5.17}$$

where H_{int} is the dipolar interaction Hamiltonian, ν_1 and ν_2 are the transition frequencies and $\Delta\nu_1$ and $\Delta\nu_2$ are the FWHM homogeneous linewidths of the spin transitions for the ions investigated. The value of the cross relaxation rate can be estimated from the measurements in this chapter. As shown in Figure 5.3, the measured detune $|\nu_1 - \nu_2|$ for two frozen-core spins is of the order of 100 Hz. The homogeneous linewidth $\Delta\nu_1 = \Delta\nu_2 = 1/(\pi T_{2Y}) = 0.2$ Hz, where $T_{2Y} = 1.6$ s is the measured coherence time demonstrated in Section 5.4. The detuning is three orders magnitude larger than the linewidth, resulting

in very small exponential part in Equation 5.17. From this calculation, a much longer frozen-core spin lifetime (T_{CR}) than the experimentally measured 27 s was expected. One explanation for this is that the frozen-core Y^{3+} ions might experience a cross-relaxation process more complicated than a direct mutual interaction between two spins: it might involved multiple ions at the same time. Then, Equation 5.17, a model describing the cross relaxation that involves only two spins, is no longer appropriate. Another explanation for the failure of the above model is that there might be other unknown sources limiting the lifetime of the frozen-core Y^{3+} spins, which are independent of the frequency detunings

In order to better understand the frozen-core Y^{3+} bath, and in particular, to understand the mechanisms that limit the lifetimes of these frozen-core Y^{3+} spins, it would be useful to measure the lifetimes of the spins at each site. With such a measurement, the dependency of the lifetime on the interaction strength (δf) could be studied. Further, as mentioned in the Section 4.5, there are critical points in Eu^{3+}:Y_2SiO_5 that occur at higher fields. Since the frequency detuning of the Y^{3+} sites increases at higher field, a significant change in the cross-relaxation process is expected. Hence, the dependency of the Y^{3+} lifetime on the cross-relaxation process might be understood by repeating the lifetime measurement of the frozen-core Y^{3+} spins, as well as other measurements presented in this chapter, at one of these higher field critical points.

Chapter 6

Conclusion and future work

Quantum memories with long storage times are essential for communication of quantum information over long distances. To achieve this, the quantum transitions of the memory material system need to have long coherence times and be optically accessible. This thesis has investigated the potential of developing such memories using the rare earth ions in solids, which are promising candidates due to the good coherence properties of their optically addressable quantum transitions. The research in this theses was performed on the hyperfine transitions of a Eu^{3+}:Y_2SiO_5 crystal because these transitions have extremely long life times (23 days). A coherence time of 6 hours on one of these transitions was reported.

Employing the ZEFOZ technique was crucial in achieving this long coherence time. The ZEFOZ technique works by applying a static magnetic field such that the Zeeman shift of the Eu^{3+} hyperfine transition of interest experiences a critical point. At the critical point, the transition has no first order component, which nulls the decoherence caused by the magnetic interactions with the host to first order. In addition, as the magnetic field of the chosen critical point was of the order of 1 T, a further extension of the coherence time occurs as this field induces a frozen core on the Eu^{3+} ions. The frozen core suppressed the spin flipping of nearby host Y^{3+} ions. As the field sensitivity of the transition is extremely low at the ZEFOZ point, the transition is only affected by large perturbations caused by the slow spin flips of these nearby Y^{3+} ions, and not the small, fast perturbation caused by the spin flips of more distant bulk Y^{3+} ions. Thus, the slow spin flips of the frozen-core Y^{3+} ions are the dominant decoherence mechanism of the Eu^{3+} hyperfine transition. A decreased spin flipping rate of these nearby host ions resulted in a decoherence rate of 8×10^{-5} s^{-1} over 100 milliseconds.

The above decoherence rate was measured using the two pulse spin echo technique. At longer evolution times of the two pulse spin echoes, the decoherence rate increases because the frozen-core Y^{3+} spins gradually flip. In order to extend the slow decoherence rate to longer evolution times, DDC pulse sequences were used. The application of the KDD_x sequence resulted in a coherence time of 6 hours.

While the achieved 6 hour coherence time dwarfs the previously achieved 10 ms in this material, there is great promise to increase this further. An analysis of the measured two pulse spin echo decay confirmed that the decoherence at the aligned critical point is still dominated by the magnetic dipole dipole interactions between the Eu^{3+} ions and Y^{3+} spin bath. Hence, a further increase in the coherence time can be achieved by further decreasing the field sensitivity of the transition and better control of the Y^{3+} spin bath. The field sensitivity of the transition can be decreased through a better alignment of the magnetic field using the strategies discussed in Section 4.5. Because the frozen-core Y^{3+} ions dominate the Eu^{3+} decoherence of a ZEFOZ transition, better control of the Y^{3+}

bath means a better control of the frozen-core Y^{3+} ions. In Chapter 5, techniques were developed to investigate the dynamics of the frozen core. A detailed investigaion of these dynamics would allow the possibility to extend the hyperfine coherence time of the Eu^{3+} ions by decoupling the Y^{3+} ions from Eu^{3+} using more sophisticated pulse sequences.

The 6 hour coherence time achieved via the KDD_x sequence demonstrated that the $^{151}Eu^{3+}$:Y_2SiO_5 system is suitable for a long-term quantum memory to store arbitrary quantum states. Similar storage times have been observed for the nuclear spin transition of ionized ^{31}P dopants in isotopically pure ^{28}Si (reference [108]). However, there are important distinctions between the $^{31}P^{+}$:^{28}Si system and the rare-earth-ion doped crystal investigated in this thesis. The first distinction is the method used to decouple the storage transition from external perturbations. The long coherence times achieved by Saeedi et al. were possible because the dominant source of magnetic perturbations, the ^{29}Si spins, was removed [108]. Contrastingly, in the current work the transition of interest was made insensitive to magnetic fluctuations. Thus, long coherence times were achieved in a crystal stoichiometric in perturbing spins. The second aspect that distinguishes the two materials is the ability to optically access the storage transition. The mapping of light onto the hyperfine transitions of $^{151}Eu^{3+}$:Y_2SiO_5 has been previously demonstrated [15], whereas a suitable optical transition to access the transition of interest in $^{31}P^{+}$:^{28}Si has not been identified. In addition, the extreme insensitivity of the europium ions to their environment allows relatively high ion densities to be achieved, which enables high optical depths for efficient absorption. It is precisely the suitability of $^{151}Eu^{3+}$:Y_2SiO_5 for an optical quantum memory that separates the observed hours-long storage from other demonstrations of long coherence times in systems such as $^{31}P^{+}$:^{28}Si [108] and cooled, nuclear-spin polarised gaseous systems [109].

Although nuclear spins in Eu^{3+}:Y_2SiO_5 stand out among the candidate systems that are suitable for quantum memories due to the observed long coherence time, more work is needed in the future before practical quantum memories for applications such as quantum repeaters can be made with this system. This is because there are other requirements for quantum memories such as large efficiency, high fidelity, multimode storage. High fidelity multimode storage in this system has been demonstrated by Laplane et al. [19]. Further, in Pr^{3+}:Y_2SiO_5, high efficiency quantum memory has been demonstrated [11]. It is slightly more difficult to achieve high efficiencies in Eu^{3+}:Y_2SiO_5 than Pr^{3+}:Y_2SiO_5 because of its lower optical depth[67]. However, the optical depth can be improved by using impedance-matched cavities [110] or longer crystals. With impedance-matched cavities, comparable efficiencies have been achieved in Eu^{3+}:Y_2SiO_5 [111] and Pr^{3+}:Y_2SiO_5 [20]. In addition, Eu^{3+}:Y_2SiO_5 possess advantages over Pr^{3+}:Y_2SiO_5 including narrower homogeneous linewidth for optical transitions, larger hyperfine splittings and longer hyperfine lifetimes. It is, therefore, reasonable to expect an efficiency in Eu^{3+}:Y_2SiO_5 similar to, or exceeding, that in Pr^{3+}:Y_2SiO_5. Incorporating large efficiency, high fidelity, and multimode storage with the long coherence time achieved in this thesis would allow the building of quantum memories that are useful in real-world quantum communication.

In practical quantum communication with the quantum repeater protocol, a common challenge is to interface a quantum memory with an entangled photon source. For rare earth-based quantum memories, an elegant solution to this challenge, based on rephased amplified spontaneous emission (RASE), has been successfully demonstrated in Pr^{3+}:Y_2SiO_5 [18, 112]. As discussed above, compared to Pr^{3+}:Y_2SiO_5, Eu^{3+}:Y_2SiO_5 has narrower homogeneous linewidth for optical transitions and larger hyperfine splitting. These properties would lead to larger temporal multiplexing capacity of this system and

hence a better performance for RASE is expected. In future work, this will be experimentally demonstrated.

It has been almost universally assumed that light is the best long-distance carrier for quantum information. However, the coherence time observed here is long enough that nuclear spins travelling at 9 kilometres per hour in a crystal would have a lower decoherence with distance than light in an optical fibre. This opens up the possibility of an intriguing alternative to entanglement distribution: the physical transport of memory crystals, in which case the crystals can be considered as persistent quantum memories. For example, a carrier of such a memory can be a satellite, then it is theoretically possible to set up entanglement between any two spots on the globe. One way to achieve this is the following: Alice, at one point on the earth, sends an optical photon through the atmosphere to the memory on the satellite, where it is held as the satellite moves until it can be sent on to the receiver Bob. In this case, the quantum information encoded in the optical signal is transferred from Alice to Bob. To develop such a memory that can work efficiently in real wold quantum communication, however, it needs to have a high data storage capacity, which will be the main challenge in this field in future work.

In summary, an experimental investigation of the development of quantum memories using rare earths in solids was presented in this thesis. I have demonstrated coherence time of rare earths in solids that are long enough to set up a global quantum network using quantum repeater protocol. Moreover, I also demonstrated the suitability of the rare earths in solids for developing persistent quantum memories, which can enable a new way for entanglement distribution: entanglement is transported by physically transporting the memory crystal rather than the light. This approach presents a new regime for both quantum communication and fundamental tests of quantum mechanics.

Appendices

Appendix A

Measurements of the quadratic Zeeman tensor in Eu^{3+}:Y_2SiO_5

A.1 Theory

This appendix presents the measurements on the quadratic Zeeman parameters of the hyperfine ground state in Eu^{3+}:Y_2SiO_5. To understand this measurement, I begin with the spin Hamiltonian, which had been discussed in detail in Section 2.3. The spin Hamiltonian is

$$H = (\boldsymbol{B}\cdot\boldsymbol{Z}\cdot\boldsymbol{B})\hat{\boldsymbol{E}} + \boldsymbol{B}\cdot\boldsymbol{M}\cdot\hat{\boldsymbol{I}} + \hat{\boldsymbol{I}}\cdot\boldsymbol{Q}\cdot\hat{\boldsymbol{I}}. \tag{A.1}$$

The first term is the quadratic Zeeman term with $\boldsymbol{Z}$ the quadratic Zeeman tensor. The quadratic Zeeman term does not affect the hyperfine transition frequencies, but it affects the electronic energy levels, which results in frequency shifts of the optical transitions in the presence of a magnetic field. The quadratic Zeeman tensor that determines the second-order field sensitivity of the frequency of the optical transition ($^7F_0 \rightarrow {}^5D_0$) is given by:

$$\boldsymbol{Z_o} = \boldsymbol{Z_e} - \boldsymbol{Z_g}, \tag{A.2}$$

where $\boldsymbol{Z_g}$ and $\boldsymbol{Z_e}$ are the quadratic Zeeman tensor for the ground state $^7F_0$ and the excited state $^5D_0$ respectively. These quadratic Zeeman tensors describe the effect on the spin Hamiltonian due to admixture of the other J states with the $J = 0$ state. Because the $^5D_0 \rightarrow {}^5D_1$ separation ($\approx$ 50 THz) is much larger than the $^7F_0 \rightarrow {}^7F_1$ separation ($\approx$ 10 THz) [67], the contribution of $\boldsymbol{Z_e}$ to $\boldsymbol{Z_o}$ can be ignored. This leads to $\boldsymbol{Z_g} = -\boldsymbol{Z_o}$ and thus $\boldsymbol{Z_g}$ can be measured by observing the second-order field senstivity of the optical transitions.

A.2 Experiment

The measurement of the parameter $\boldsymbol{Z_o}$ along a fixed direction is shown in Figure A.1. With the crystal aligned along a fixed field direction (with an uncertainty of 10°), the optical absorption spectrum was recorded at different field magnitudes from 0 T to 3.9 T. Then a quadratic fitting of the transition frequency at the maximum value of the spectrum as a function of the field magnitude gave the quadratic Zeeman parameter along that direction. As shown in Figure A.2, the parameters of $\boldsymbol{Z_o}$ along D_1, D_2 and C_2 axes of the crystal were measure to be 0.56 Hz/G^2, 0.52 Hz/G^2 and 1.58 Hz/G^2 respectively. From the above discussion, the quadratic parameters of $\boldsymbol{Z_g}$ along D_1, D_2 and C_2 axes are -0.56 Hz/G^2, -0.52 Hz/G^2 and -1.58 Hz/G^2 respectively. With these parameters, the quadratic Zeeman

tensor $\boldsymbol{Z_g}$ can be calculated as illustrated in Section 2.5.3.

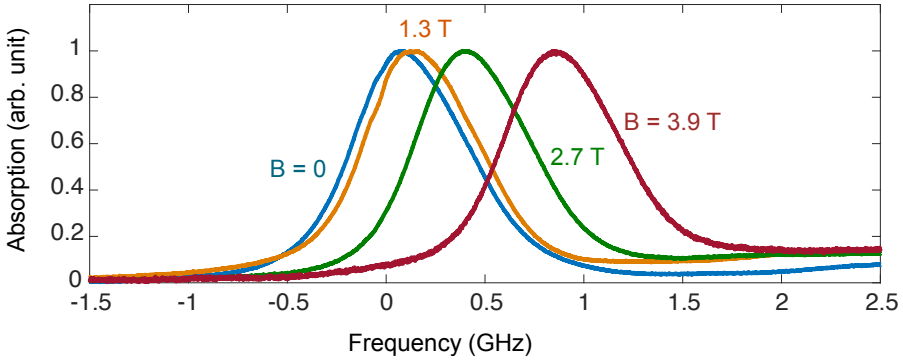

Figure A.1: The measured optical absorption spectrum for $^7F_0 \rightarrow {}^5D_0$ transition corresponding to different field magnitude as marked while the field was applied along the D_1 axis of the crystal. The label of the x-axis is the optical frequency offset from the centre frequency of the zero field spectrum.

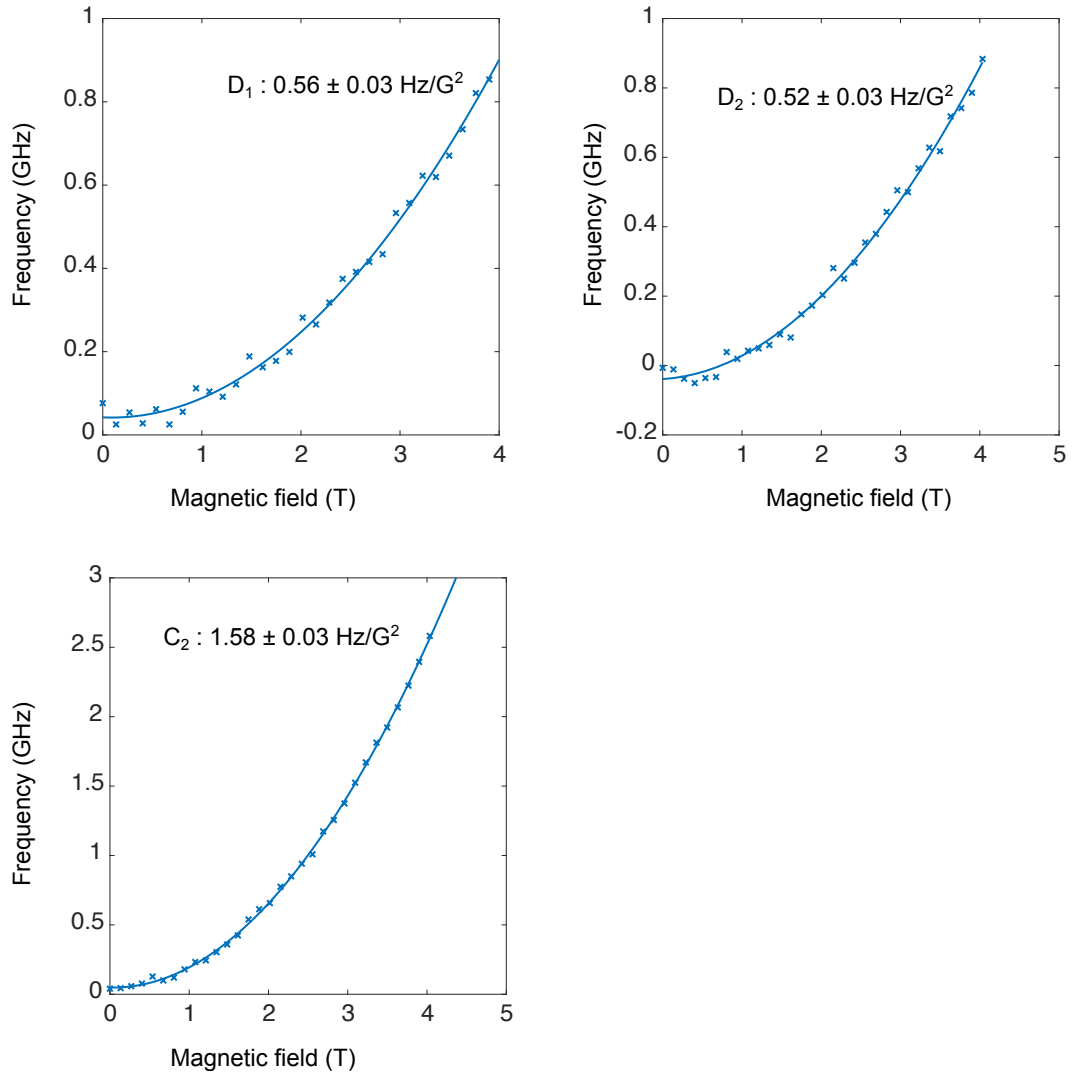

Figure A.2: The measured frequency of $^7F_0 \rightarrow {}^5D_0$ transitions plotted as a function of the field magnitude. The cross symbols are data from measurements while the solid lines are the quadratic fits. The three data sets corresponds to the field direction as marked and the quadratic Zeeman parameters from the fitting are marked in the figure as well. The uncertainties were obtained from the fitting.

Bibliography

[1] Albert Einstein, Boris Podolsky, and Nathan Rosen. Can quantum-mechanical description of physical reality be considered complete? *Physical review*, 47(10):777, 1935.
(Cited on pages 1 and 2.)

[2] David Bohm. A suggested interpretation of the quantum theory in terms o "hidden" variables. *Physical Review*, 85(2):166, 1952.
(Cited on page 2.)

[3] David Bohm and Yakir Aharonov. Discussion of experimental proof for the paradox of einstein, rosen, and podolsky. *Physical Review*, 108(4):1070, 1957.
(Cited on page 2.)

[4] J. S. Bell. On the Einstein Podolsky Rosen paradox. *Physics*, pages 195–200, 1964.
(Cited on pages 1, 2, 4, and 6.)

[5] JF Dynes, H Takesue, ZL Yuan, AW Sharpe, K Harada, T Honjo, H Kamada, O Tadanaga, Y Nishida, M Asobe, et al. Efficient entanglement distribution over 200 kilometers. *Optics express*, 17(14):11440–11449, 2009.
(Cited on page 1.)

[6] Juan Yin, Ji-Gang Ren, He Lu, Yuan Cao, Hai-Lin Yong, Yu-Ping Wu, Chang Liu, Sheng-Kai Liao, Fei Zhou, Yan Jiang, et al. Quantum teleportation and entanglement distribution over 100-kilometre free-space channels. *Nature*, 488(7410):185–188, 2012.
(Cited on page 1.)

[7] H-J Briegel, Wolfgang Dür, Juan I Cirac, and Peter Zoller. Quantum repeaters: the role of imperfect local operations in quantum communication. *Physical Review Letters*, 81(26):5932, 1998.
(Cited on pages 1 and 7.)

[8] L-M Duan, MD Lukin, J Ignacio Cirac, and Peter Zoller. Long-distance quantum communication with atomic ensembles and linear optics. *Nature*, 414(6862):413–418, 2001.
(Cited on pages 1, 7, and 10.)

[9] JJ Longdell, Elliott Fraval, MJ Sellars, and NB Manson. Stopped light with storage times greater than one second using electromagnetically induced transparency in a solid. *Physical review letters*, 95(6):063601, 2005.
(Cited on page 1.)

[10] Elliott Fraval, MJ Sellars, and JJ Longdell. Dynamic decoherence control of a solid-state nuclear-quadrupole qubit. *Physical review letters*, 95(3):030506, 2005.
(Cited on pages 2, 13, 31, and 38.)

[11] Morgan P Hedges, Jevon J Longdell, Yongmin Li, and Matthew J Sellars. Efficient quantum memory for light. *Nature*, 465(7301):1052–1056, 2010.
(Cited on pages 1, 11, and 96.)

[12] Georg Heinze, Christian Hubrich, and Thomas Halfmann. Stopped light and image storage by electromagnetically induced transparency up to the regime of one minute. *Physical review letters*, 111(3):033601, 2013.
(Cited on pages 1, 2, 11, 13, 31, and 38.)

[13] Christoph Clausen, Imam Usmani, Félix Bussieres, Nicolas Sangouard, Mikael Afzelius, Hugues de Riedmatten, and Nicolas Gisin. Quantum storage of photonic entanglement in a crystal. *Nature*, 469(7331):508–511, 2011.
(Cited on page 1.)

[14] Erhan Saglamyurek, Neil Sinclair, Jeongwan Jin, Joshua A Slater, Daniel Oblak, Félix Bussieres, Mathew George, Raimund Ricken, Wolfgang Sohler, and Wolfgang Tittel. Broadband waveguide quantum memory for entangled photons. *Nature*, 469(7331):512–515, 2011.
(Cited on page 1.)

[15] Nuala Timoney, Bjorn Lauritzen, Imam Usmani, Mikael Afzelius, and Nicolas Gisin. Atomic frequency comb memory with spin-wave storage in 153eu3+: Y2sio5. *Journal of Physics B: Atomic, Molecular and Optical Physics*, 45(12):124001, 2012.
(Cited on pages 1 and 96.)

[16] CW Thiel, Thomas Böttger, and RL Cone. Rare-earth-doped materials for applications in quantum information storage and signal processing. *Journal of luminescence*, 131(3):353–361, 2011.
(Cited on page 1.)

[17] Flurin Könz, Y Sun, CW Thiel, RL Cone, RW Equall, RL Hutcheson, and RM Macfarlane. Temperature and concentration dependence of optical dephasing, spectral-hole lifetime, and anisotropic absorption in Eu^{3+}:Y_2SiO_5. *Physical Review B*, 68(8):085109, 2003.
(Cited on pages 1, 11, 13, 19, 22, 25, 26, 38, 46, 53, 74, and 77.)

[18] Kate R Ferguson, Sarah E Beavan, Jevon J Longdell, and Matthew J Sellars. Generation of light with multimode time-delayed entanglement using storage in a solid-state spin-wave quantum memory. *Physical Review Letters*, 117(2):020501, 2016.
(Cited on pages 1 and 96.)

[19] Cyril Laplane, Pierre Jobez, Jean Etesse, Nuala Timoney, Nicolas Gisin, and Mikael Afzelius. Multiplexed on-demand storage of polarization qubits in a crystal. *New Journal of Physics*, 18(1):013006, 2015.
(Cited on pages 1 and 96.)

[20] Mahmood Sabooni, Qian Li, Stefan Kröll, and Lars Rippe. Efficient quantum memory using a weakly absorbing sample. *Physical review letters*, 110(13):133604, 2013.
(Cited on pages 1 and 96.)

[21] Elliott Fraval, MJ Sellars, and JJ Longdell. Method of extending hyperfine coherence times in Pr^{3+}:Y_2SiO_5. *Physical review letters*, 92(7):077601, 2004.
(Cited on pages 2, 28, 30, 31, 32, 61, and 67.)

[22] JJ Longdell, AL Alexander, and MJ Sellars. Characterization of the hyperfine interaction in europium-doped yttrium orthosilicate and europium chloride hexahydrate. *Physical Review B*, 74(19):195101, 2006.
(Cited on pages 2, 23, 31, 32, 55, 56, and 62.)

[23] Charles H. Bennett, Gilles Brassard, Seth Breidbard, and Stephen Wiesner. Advances in Cryptology: Proceedings of CRYPTO '82. *Plenum*, 108:267–275, 1982.
(Cited on page 2.)

[24] Erwin Schrödinger. Discussion of probability relations between separated systems. In *Mathematical Proceedings of the Cambridge Philosophical Society*, volume 31, pages 555–563. Cambridge Univ Press, 1935.
(Cited on pages 2 and 4.)

[25] Stuart J Freedman and John F Clauser. Experimental test of local hidden-variable theories. *Physical Review Letters*, 28(14):938, 1972.
(Cited on page 4.)

[26] Paul G Kwiat, Klaus Mattle, Harald Weinfurter, Anton Zeilinger, Alexander V Sergienko, and Yanhua Shih. New high-intensity source of polarization-entangled photon pairs. *Physical Review Letters*, 75(24):4337, 1995.
(Cited on page 4.)

[27] Alain Aspect, Philippe Grangier, and Gérard Roger. Experimental tests of realistic local theories via bell's theorem. *Physical Review Letters*, 47(7):460, 1981.
(Cited on page 4.)

[28] Alain Aspect, Jean Dalibard, and Gérard Roger. Experimental test of bell's inequalities using time-varying analyzers. *Physical review letters*, 49(25):1804, 1982.
(Cited on page 4.)

[29] John Stewart Bell. *Speakable and unspeakable in quantum mechanics: Collected papers on quantum philosophy*. Cambridge university press, 2004.
(Cited on page 4.)

[30] Emilio Santos. Critical analysis of the empirical tests of local hidden-variable theories. *Physical review A*, 46(7):3646, 1992.
(Cited on page 4.)

[31] Bas Hensen, H Bernien, AE Dréau, A Reiserer, N Kalb, MS Blok, J Ruitenberg, RFL Vermeulen, RN Schouten, C Abellán, et al. Loophole-free bell inequality violation using electron spins separated by 1.3 kilometres. *Nature*, 526(7575):682–686, 2015.
(Cited on page 4.)

[32] Daniel R Simon. On the power of quantum computation. *SIAM journal on computing*, 26(5):1474–1483, 1997.
(Cited on page 5.)

[33] Thomas Monz, Philipp Schindler, Julio T Barreiro, Michael Chwalla, Daniel Nigg, William A Coish, Maximilian Harlander, Wolfgang Hänsel, Markus Hennrich, and Rainer Blatt. 14-qubit entanglement: Creation and coherence. *Physical Review Letters*, 106(13):130506, 2011.
(Cited on page 5.)

[34] Peter W Shor. Polynomial-time algorithms for prime factorization and discrete logarithms on a quantum computer. *SIAM review*, 41(2):303–332, 1999.
(Cited on page 5.)

[35] Daniel J Bernstein. Introduction to post-quantum cryptography. In *Post-quantum cryptography*, pages 1–14. Springer, 2009.
(Cited on page 5.)

[36] C.H. Bennett and G. Brassard. Quantum cryptography: public key distribution and coin tossing. *IEEE International Conference on Computers Systems and Signal Processing, Bangalore India*, 1984.
(Cited on page 6.)

[37] Charles H Bennett, François Bessette, Gilles Brassard, Louis Salvail, and John Smolin. Experimental quantum cryptography. *Journal of cryptology*, 5(1):3–28, 1992.
(Cited on page 6.)

[38] Brahim Lounis and Michel Orrit. Single-photon sources. *Reports on Progress in Physics*, 68(5):1129, 2005.
(Cited on page 6.)

[39] Hugues De Riedmatten, Julien Laurat, Chin-Wen Chou, EW Schomburg, Daniel Felinto, and H Jeff Kimble. Direct measurement of decoherence for entanglement between a photon and stored atomic excitation. *Physical review letters*, 97(11):113603, 2006.
(Cited on page 6.)

[40] DN Matsukevich, T Chaneliere, SD Jenkins, S-Y Lan, TAB Kennedy, and A Kuzmich. Deterministic single photons via conditional quantum evolution. *Physical review letters*, 97(1):013601, 2006.
(Cited on page 6.)

[41] Shuai Chen, Yu-Ao Chen, Thorsten Strassel, Zhen-Sheng Yuan, Bo Zhao, Jörg Schmiedmayer, and Jian-Wei Pan. Deterministic and storable single-photon source based on a quantum memory. *Physical review letters*, 97(17):173004, 2006.
(Cited on page 6.)

[42] Artur K Ekert. Quantum cryptography based on bell?s theorem. *Physical review letters*, 67(6):661, 1991.
(Cited on page 6.)

[43] M. Fox. Quantum Optics. *Oxford University Press*, pages 296–297, 2006.
(Cited on page 6.)

[44] Marek Zukowski, Anton Zeilinger, Michael A Horne, and Aarthur K Ekert. Event-ready-detectors bell experiment via entanglement swapping. *Physical Review Letters*, 71(26):4287–4290, 1993.
(Cited on pages 6 and 7.)

[45] Mikael Afzelius, Thierry Chaneliere, Rufus L Cone, Stefan Kröll, Sergey A Moiseev, Matthew Sellars, et al. Photon-echo quantum memory in solid state systems. *Laser*

& Photonics Reviews, 4(2):244–267, 2010.
(Cited on pages 7 and 11.)

[46] Zhi Zhao, Tao Yang, Yu-Ao Chen, An-Ning Zhang, and Jian-Wei Pan. Experimental realization of entanglement concentration and a quantum repeater. *Physical review letters*, 90(20):207901, 2003.
(Cited on page 7.)

[47] Félix Bussières, Nicolas Sangouard, Mikael Afzelius, Hugues de Riedmatten, Christoph Simon, and Wolfgang Tittel. Prospective applications of optical quantum memories. *Journal of Modern Optics*, 60(18):1519–1537, 2013.
(Cited on pages 8, 10, and 11.)

[48] Markus Aspelmeyer, Thomas Jennewein, Martin Pfennigbauer, Walter R Leeb, and Anton Zeilinger. Long-distance quantum communication with entangled photons using satellites. *IEEE Journal of Selected Topics in Quantum Electronics*, 9(6):1541–1551, 2003.
(Cited on page 9.)

[49] Zhen-Sheng Yuan, Xiao-Hui Bao, Chao-Yang Lu, Jun Zhang, Cheng-Zhi Peng, and Jian-Wei Pan. Entangled photons and quantum communication. *Physics Reports*, 497(1):1–40, 2010.
(Cited on page 9.)

[50] Cristian Bonato, Markus Aspelmeyer, Thomas Jennewein, Claudio Pernechele, Paolo Villoresi, and Anton Zeilinger. Influence of satellite motion on polarization qubits in a space-earth quantum communication link. *Optics express*, 14(21):10050–10059, 2006.
(Cited on page 9.)

[51] Cheng-Zhi Peng, Tao Yang, Xiao-Hui Bao, Jun Zhang, Xian-Min Jin, Fa-Yong Feng, Bin Yang, Jian Yang, Juan Yin, Qiang Zhang, et al. Experimental free-space distribution of entangled photon pairs over 13 km: towards satellite-based global quantum communication. *Physical review letters*, 94(15):150501, 2005.
(Cited on page 9.)

[52] Xiao-Song Ma, Thomas Herbst, Thomas Scheidl, Daqing Wang, Sebastian Kropatschek, William Naylor, Bernhard Wittmann, Alexandra Mech, Johannes Kofler, Elena Anisimova, et al. Quantum teleportation over 143 kilometres using active feed-forward. *Nature*, 489(7415):269–273, 2012.
(Cited on page 9.)

[53] E. Bibeny. One giant step for quantum internet. *Nature*, 535:478, 2016.
(Cited on page 9.)

[54] Marlan O Scully and M Suhail Zubairy. Quantum optics, 1999.
(Cited on page 10.)

[55] Pierre Meystre and Murray Sargent. *Elements of quantum optics*. Springer Science & Business Media, 2013.
(Cited on page 10.)

[56] David J Wineland, M Barrett, J Britton, J Chiaverini, B DeMarco, WM Itano, B Jelenković, C Langer, D Leibfried, V Meyer, et al. Quantum information processing with trapped ions. *Philosophical Transactions of the Royal Society of London A: Mathematical, Physical and Engineering Sciences*, 361(1808):1349–1361, 2003.
(Cited on page 10.)

[57] YO Dudin, L Li, and A Kuzmich. Light storage on the time scale of a minute. *Physical Review A*, 87(3):031801, 2013.
(Cited on page 10.)

[58] Charles Santori, David Fattal, Jelena Vučković, Glenn S Solomon, and Yoshihisa Yamamoto. Indistinguishable photons from a single-photon device. *nature*, 419(6907):594–597, 2002.
(Cited on page 11.)

[59] Andreas Wallraff, David I Schuster, Alexandre Blais, L Frunzio, R-S Huang, J Majer, S Kumar, Steven M Girvin, and Robert J Schoelkopf. Strong coupling of a single photon to a superconducting qubit using circuit quantum electrodynamics. *Nature*, 431(7005):162–167, 2004.
(Cited on page 11.)

[60] Patrick M Ledingham, William R Naylor, and Jevon J Longdell. Experimental realization of light with time-separated correlations by rephasing amplified spontaneous emission. *Physical review letters*, 109(9):093602, 2012.
(Cited on page 11.)

[61] Sarah E Beavan, Morgan P Hedges, and Matthew J Sellars. Demonstration of photon-echo rephasing of spontaneous emission. *Physical review letters*, 109(9):093603, 2012.
(Cited on page 11.)

[62] J Becquerel and H Kamerlingh Onnes. The absorption spectra of the compounds of the rare earths at the temperatures obtainable with liquid hydrogen, and their change by the magnetic field. *Koninklijke Nederlandse Akademie van Wetenschappen Proceedings Series B Physical Sciences*, 10:592–603, 1908.
(Cited on page 13.)

[63] V. M. Agranovich and A. A. Maradudin. Spectroscopy of solids containing rare earth ions, 1 ed. *Noth-Holland Physics Publishing, Amsterdam*, 1987.
(Cited on page 13.)

[64] Thomas Böttger, CW Thiel, RL Cone, and Y Sun. Effects of magnetic field orientation on optical decoherence in Er^{3+}:Y_2SiO_5. *Physical Review B*, 79(11):115104, 2009.
(Cited on page 13.)

[65] RD t Shannon and C Tfc Prewitt. Effective ionic radii in oxides and fluorides. *Acta Crystallographica Section B: Structural Crystallography and Crystal Chemistry*, 25(5):925–946, 1969.
(Cited on page 14.)

[66] Arthur J Freeman and RE Watson. Theoretical investigation of some magnetic and spectroscopic properties of rare-earth ions. *Physical Review*, 127(6):2058, 1962.
(Cited on page 15.)

[67] Guokui Liu and Bernard Jacquier. *Spectroscopic properties of rare earths in optical materials*, volume 83. Springer Science & Business Media, 2006.
(Cited on pages 16, 18, 20, 21, 22, 25, 27, 34, 96, and 101.)

[68] Go Ho Dieke and HM Crosswhite. The spectra of the doubly and triply ionized rare earths. *Applied optics*, 2(7):675–686, 1963.
(Cited on page 16.)

[69] W. T. Carnall and H. M. Crosswhite . Technical Report No. 60439 (unpublished). *Argonne National Lab*, page 681, 1989.
(Cited on page 16.)

[70] GF Imbusch and R Kopelman. Optical spectroscopy of electronic centers in solids. In *Laser spectroscopy of solids*, pages 1–37. Springer, 1981.
(Cited on page 17.)

[71] Y. Sun, T. Böttger, C. W. Thiel, and R. L. Cone. X-ray Structure Determination of $Tm : Y_2SiO_5$. *Physical Review B*, 77:085124, 2008.
(Cited on page 18.)

[72] BR Judd. Optical absorption intensities of rare-earth ions. *Physical Review*, 127(3):750, 1962.
(Cited on page 19.)

[73] GS Ofelt. Intensities of crystal spectra of rare-earth ions. *The Journal of Chemical Physics*, 37(3):511–520, 1962.
(Cited on page 19.)

[74] Lidia Smentek and B ANDES HESS. Theoretical description of 0 0 and 0 1 transitions in the eu3+ ion in hosts with c2v symmetry. *Molecular Physics*, 92(5):835–846, 1997.
(Cited on page 19.)

[75] RM Macfarlane and RM Shelby. Coherent transient and holeburning spectroscopy of rare earth ions in solids. *Spectroscopy of solids containing rare earth ions*, 21, 1987.
(Cited on page 19.)

[76] MA Teplov. Magnetic resonance on Pr^{141} nuclei in a $Pr_2(SO_4)_3 \cdot 8H_2O$ single crystal. *Soviet Journal of Experimental and Theoretical Physics*, 26:872, 1968.
(Cited on page 19.)

[77] Ryuzi Yano, Masaharu Mitsunaga, and Naoshi Uesugi. Ultralong optical dephasing time in $Eu^{3+}:Y_2SiO_5$. *Optics letters*, 16(23):1884–1886, 1991.
(Cited on pages 22, 30, 32, and 56.)

[78] Ryuzi Yano, Masaharu Mitsunaga, and Naoshi Uesugi. Nonlinear laser spectroscopy of $Eu^{3+}:Y_2SiO_5$ and its application to time-domain optical memory. *JOSA B*, 9(6):992–997, 1992.
(Cited on page 22.)

[79] R. Ahlefeldt. Evaluation of a stoichiometric rare earth crystal for quantum computing, Page 25, PhD thesis of the Australian Nationall University. 2013.
(Cited on page 25.)

[80] R Orbach. Spin-lattice relaxation in rare-earth salts. In *Proceedings of the Royal Society of London A: Mathematical, Physical and Engineering Sciences*, volume 264, pages 458–484. The Royal Society, 1961.
(Cited on page 25.)

[81] DE McCumber and MD Sturge. Linewidth and temperature shift of the r lines in ruby. *Journal of Applied Physics*, 34(6):1682–1684, 1963.
(Cited on page 25.)

[82] Toru Miyakawa and DL Dexter. Phonon sidebands, multiphonon relaxation of excited states, and phonon-assisted energy transfer between ions in solids. *Physical Review B*, 1(7):2961, 1970.
(Cited on page 25.)

[83] AK Rebane, CW Thiel, RK Mohan, and RL Cone. Slow decoherence and the radiative decay limit in rare-earth-doped crystals for coherent optical storage. *Bulletin of the Russian Academy of Sciences: Physics*, 74(7):891–900, 2010.
(Cited on page 25.)

[84] R Wo Equall, Yongchen Sun, RL Cone, and RM Macfarlane. Ultraslow optical dephasing in Eu^{3+}:Y_2SiO_5. *Physical review letters*, 72(14):2179, 1994.
(Cited on page 26.)

[85] WB Mims. Phase memory in electron spin echoes, lattice relaxation effects in $cawo_4$: Er, ce, mn. *Physical Review*, 168(2):370, 1968.
(Cited on pages 28, 43, 45, 46, 47, 48, and 69.)

[86] LL Wald, Erwin L Hahn, and Matjaz Lukac. Variation of the Pr^{3+} nuclear quadrupole resonance spectrum across the inhomogeneous optical line in Pr^{3+} : LaF_3. *JOSA B*, 9(5):784–788, 1992.
(Cited on page 28.)

[87] Joseph Ganem, YP Wang, RS Meltzer, and WM Yen. Magnetic-field dependence of photon-echo decays in ruby. *Physical Review B*, 43(10):8599, 1991.
(Cited on page 28.)

[88] Joseph Ganem, YP Wang, D Boye, RS Meltzer, WM Yen, and RM Macfarlane. Nonexponential photon-echo decays of paramagnetic ions in the superhyperfine limit. *Physical review letters*, 66(6):695, 1991.
(Cited on page 28.)

[89] RM Macfarlane, R Wannemacher, D Boye, YP Wang, and RS Meltzer. Nonexponential photon echo decay of Er^{3+} in fluorides. *Journal of luminescence*, 48:313–317, 1991.
(Cited on page 28.)

[90] RM Macfarlane. Photon-echo measurements on the trivalent thulium ion. *Optics letters*, 18(22):1958–1960, 1993.
(Cited on page 28.)

[91] C Langer, R Ozeri, John D Jost, J Chiaverini, B DeMarco, A Ben-Kish, RB Blakestad, J Britton, DB Hume, WM Itano, et al. Long-lived qubit memory using atomic ions. *Physical review letters*, 95(6):060502, 2005.
(Cited on page 31.)

[92] E. Fraval. Minimising the Decoherence of Rare Earth Ion Solid State Spin Qubits, Page 64, PhD thesis of The Australian National University. 2005.
(Cited on pages 32, 34, and 69.)

[93] R. Ahlefeldt. Personal communication. 2013.
(Cited on page 33.)

[94] G. J. Pryde. Ultra-High Resolution Spectroscopic Studies of Oprical Dephasing in Solids, Ph.D. thesis, RSPhySSE, ANU. 1999.
(Cited on page 35.)

[95] Erwin L Hahn. Spin echoes. *Physical review*, 80(4):580, 1950.
(Cited on page 44.)

[96] NA Kurnit, ID Abella, and SR Hartmann. Observation of a photon echo. *Physical Review Letters*, 13(19):567, 1964.
(Cited on page 44.)

[97] B Herzog and EL Hahn. Transient nuclear induction and double nuclear resonance in solids. *Physical Review*, 103(1):148, 1956.
(Cited on pages 46 and 47.)

[98] Juan I Cirac and Peter Zoller. Quantum computations with cold trapped ions. *Physical review letters*, 74(20):4091, 1995.
(Cited on page 48.)

[99] JR Klauder and PW Anderson. Spectral diffusion decay in spin resonance experiments. *Physical Review*, 125(3):912, 1962.
(Cited on page 48.)

[100] Isaac L Chuang, Lieven MK Vandersypen, Xinlan Zhou, Debbie W Leung, and Seth Lloyd. Experimental realization of a quantum algorithm. *Nature*, 393(6681):143–146, 1998.
(Cited on page 48.)

[101] Saul Meiboom and David Gill. Modified spin-echo method for measuring nuclear relaxation times. *Review of scientific instruments*, 29(8):688–691, 1958.
(Cited on page 50.)

[102] Alexandre M Souza, Gonzalo A Álvarez, and Dieter Suter. Robust dynamical decoupling for quantum computing and quantum memory. *Physical review letters*, 106(24):240501, 2011.
(Cited on pages 50 and 71.)

[103] J Mlynek, NC Wong, RG DeVoe, ES Kintzer, and RG Brewer. Raman heterodyne detection of nuclear magnetic resonance. *Physical Review Letters*, 50(13):993, 1983.
(Cited on page 53.)

[104] Andrea Arcangeli, Marko Lovrić, Biagio Tumino, Alban Ferrier, and Philippe Goldner. Spectroscopy and coherence lifetime extension of hyperfine transitions in $^{151}Eu^{3+}$:Y_2SiO_5. *Physical Review B*, 89(18):184305, 2014.
(Cited on pages 69 and 83.)

[105] Roger M Macfarlane. High-resolution laser spectroscopy of rare-earth doped insulators: a personal perspective. *Journal of luminescence*, 100(1):1–20, 2002.
(Cited on page 74.)

[106] RM Macfarlane, RS Meltzer, and BZ Malkin. Optical measurement of the isotope shifts and hyperfine and superhyperfine interactions of nd in the solid state. *Physical Review B*, 58(9):5692, 1998.
(Cited on page 74.)

[107] N Bloembergen, S Shapiro, PS Pershan, and JO Artman. Cross-relaxation in spin systems. *Physical Review*, 114(2):445, 1959.
(Cited on pages 88 and 93.)

[108] Kamyar Saeedi, Stephanie Simmons, Jeff Z Salvail, Phillip Dluhy, Helge Riemann, Nikolai V Abrosimov, Peter Becker, Hans-Joachim Pohl, John JL Morton, and Mike LW Thewalt. Room-temperature quantum bit storage exceeding 39 minutes using ionized donors in silicon-28. *Science*, 342(6160):830–833, 2013.
(Cited on page 96.)

[109] Werner Heil, Claudia Gemmel, Sergei Karpuk, Yuri Sobolev, Kathlynne Tullney, Fabian Allmendinger, Ulrich Schmidt, Martin Burghoff, Wolfgang Kilian, Silvia Knappe-Grüneberg, et al. Spin clocks: Probing fundamental symmetries in nature. *Annalen der Physik*, 525(8-9):539–549, 2013.
(Cited on page 96.)

[110] Mikael Afzelius and Christoph Simon. Impedance-matched cavity quantum memory. *Physical Review A*, 82(2):022310, 2010.
(Cited on page 96.)

[111] Pierre Jobez, Imam Usmani, Nuala Timoney, Cyril Laplane, Nicolas Gisin, and Mikael Afzelius. Cavity-enhanced storage in an optical spin-wave memory. *New Journal of Physics*, 16(8):083005, 2014.
(Cited on page 96.)

[112] Patrick M Ledingham, William R Naylor, Jevon J Longdell, Sarah E Beavan, and Matthew J Sellars. Nonclassical photon streams using rephased amplified spontaneous emission. *Physical Review A*, 81(1):012301, 2010.
(Cited on page 96.)